



## Diplomarbeit

# Effect of heat treatments on the microstructure of deformed Ti-6Al-4V

ausgeführt zum Zwecke der Erlangung des akademischen Grades eines  
Diplomingenieurs der technischen Wissenschaften unter der Leitung von

Dipl. Ing. Dr. techn. Fernando Warchomicka

und

o. Univ. Prof. Dipl. Ing. Dr. techn. H. P. Degischer

E308

Institut für Werkstoffwissenschaft und Werkstofftechnologie

eingereicht an der Technischen Universität Wien

**Fakultät für Maschinenwesen und Betriebswissenschaften**

von

Pere Barriobero Vila

Matr. Nr: 0929167

Hernalser Hauptstraße 110/22

A-1170 – Wien

Wien, am 24. September 2010

Pere Barriobero Vila



# Acknowledgments

---

This work was carried out under the project N° 815855, MITI64, sponsored by the Austrian Research Promotion Agency (programme “TAKE OFF”) in cooperation with Böhler Schmiedetechnik GmbH & Co KG. I would like to thank to Prof. Hirt (RWTH Aachen University) for the provision of the Servotest machine and to USTEM (Vienna University of Technology) for the EBSD facilities.

First and foremost I would like to express my sincerely grateful to my advisor Dipl. Ing. Dr. techn. Fernando Warchomicka for his unwavering close support towards my work and my stay in Vienna. His passion and experience in materials science as well as the friendly experiences that we have shared made this work possible.

Next I also would like to thank my co-advisor Dipl. Ing. Dr. techn. Cecilia Poletti for her valuable guidance, discussions and support through this work and at personal level for her talks about everything.

I am also indebted with Prof. Dipl. Ing. Dr. techn H. P. Degischer for giving me the opportunity to be in Vienna and accept me to accomplish this work in the institute. I want also to express my gratitude to him for accepting to read this work and for the interesting suggestions about it.

I also would like to extend my sincere gratitude to Dr. M. Stockinger for his vital suggestions and generous foresight about research during the project meetings.

A heartfelt affection to my colleagues of the institute and people that I have known there for the kind, amuse and easygoing attitude during work time.

My live in Vienna would not have been enjoyable without the friends that I have here. Live in a foreign place gave me the opportunity to know them and learn of their energy in every single experience that we share in every trip, concert, club, parade, marathon, museum, flat or Gürtel excursion.

Last but not least, I would like to express my love to my family and especially my parents back in Catalunya for their mental support and encouragement to put me up through the years. Definitely they made the biggest sacrifice.

# Abstract

---

Titanium alloys are widely used in aerospace applications due to their unique combination of low density and high strength. The Ti6Al4V alloy, which has the highest percentage of all applications, belongs to the group of  $\alpha+\beta$  alloys. For  $\alpha+\beta$  alloys as well as for  $\beta$  alloys, the mechanical properties which are relevant for particular applications are optimized for microstructural control. A prerequisite for property optimization is a profound knowledge of the microstructure-property relationships on one hand, and of the microstructure's evolution as a result of processing on the other hand.

Annealing heat treatments below  $\beta$  transus temperature followed by different cooling rates are carried to hot deformed samples in  $\alpha+\beta$  field. The experimental results show the influence of deformation temperature in the final microstructure after the annealing. A posterior effect of an ageing treatment is also studied after annealing presenting a strong interdependence of the resulting cooling rate on the final microstructure. In addition, a combination of isothermal heat treatments below  $\beta$  transus followed by controlled cooling rates were carried out to samples deformed in the  $\alpha+\beta$  field with the intention to obtain recrystallized structures.

The microstructure is analyzed at different zones of the sample by quantitative analysis after annealing showing a lean influence of deformation parameters. Differential scanning calorimetry analysis with dilatometry and hardness tests are also used to investigate the correlation of the microstructure after the heat treatments with the deformation parameters.

# Content

---

1.....	Introduction.....	1
2.....	State of Art.....	3
2.1.	Titanium Alloys.....	3
2.2.	Methodology.....	19
3.....	Experimental.....	32
3.1.	Material.....	32
3.2.	Heat treatments.....	33
3.3.	Metallography.....	35
3.4.	Differential scanning calorimetry.....	37
3.5.	Hardness.....	39
4.....	Results.....	41
4.1.	Metallography.....	41
4.2.	Quantification.....	52
4.3.	DSC.....	57
4.4.	Dilatometry.....	59
4.5.	Hardness.....	60
5.....	Interpretation and discussion.....	62
6.....	Conclusions.....	67
7.....	References.....	68

# 1. Introduction

---

High strength, low density, and excellent corrosion resistance are the main properties that make titanium attractive for variety of applications including aircraft parts, biomedical devices or components in chemical processes. Although Ti has a low strength-price ratio it is used in certain necessary applications. Basically, the price is the consequence of the reactivity of Ti with oxygen during the production process, where vacuum or inert atmosphere is required. The cost of this material has hindered a wider use for example in automotive applications, where aluminium is used instead of Ti. Aluminium is the main competitor in light weight structural applications presenting a higher specific stiffness in bending, but the higher melting temperature of Ti gives an advantage for service at high temperatures. The maximum service temperature for Ti alloys is about 600°C due to the fast growing of oxide layers and subsequent embrittlement of the surface [1].

Within the family of titanium alloys, the  $\alpha+\beta$  alloys are the most widely used because of the great variety of microstructures and mechanical properties that can be obtained by varying their composition and thermomechanical treatments [1]. One of these  $\alpha+\beta$  alloys has the greatest commercial importance namely Ti6Al4V, making up more than half of the sales of titanium alloys [2].

In order to control the microstructure of titanium alloys, most of the studies in  $\alpha+\beta$  field are focused in the evolution of the primary  $\alpha$  phase. In addition, is important to understand the effect of processing parameters on the precipitation mechanism of secondary  $\alpha$  phase so as to control the microstructure by processing parameters in the high temperature deformation of titanium alloys [3].

In this work Ti6Al4V alloy is examined to determine the effect of annealing and ageing on the microstructure after hot deformation in  $\alpha+\beta$  field. Thus, the effect of deformation parameters on the precipitation mechanism of the secondary  $\alpha$  phase is studied. Section 2 describes the state of art of titanium alloys focusing in phase transformations, features and thermoprocessing of  $\alpha$ ,  $\alpha+\beta$  and  $\beta$  alloys, mechanical properties and main applications. In this section also general information about the used analysing techniques is correlated with literature of studies carried out on Ti6Al4V. Section 3 corresponds to the experimental part where all the information about the equipments, experiments and procedures is reported.

Section 4 shows all the results about metallography, quantitative analysis, DSC measurements, dilatometry and hardness. Afterwards, in section 5 all the results are used to interpret the phase transformations by relating and comparing them with the literature.

## 2. State of Art

---

### 2.1. Titanium Alloys

#### 2.1.1. Pure titanium

An allotropic phase transformation is shown in pure Ti at 882°C heating the material from  $\alpha$  phase (hexagonal close-packed crystal structure, hcp) at low temperatures, to  $\beta$  phase (body-centred cubic crystal structure, bcc) at higher temperatures. Depending on what kind of interstitial and substitutional elements are alloyed with Ti, the transformation temperature can increase or decrease. For this hcp structure the most densely packed planes are the basal plane (0002), the three prismatic planes  $\{10\bar{1}0\}$  and the six pyramidal planes  $\{10\bar{1}\bar{1}\}$ . The three basal axis  $a_1$ ,  $a_2$ ,  $a_3$  are in the closed-packed directions with the indices  $\langle 11\bar{2}0 \rangle$ . The six most densely packed lattice planes in the bcc structure are  $\{110\}$  with four  $\langle 111 \rangle$  closed-packed directions (Fig.2.1) [1].

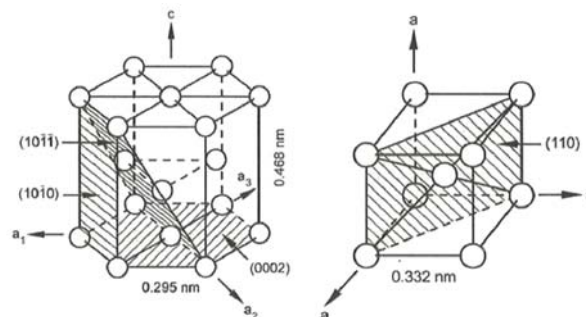


Fig.2.1. Unit cell of  $\alpha$  phase (hcp) and unit cell of  $\beta$  phase (bcc) [1].

The anisotropic character of the hcp structure has important consequences for the elastic properties of Ti and its alloys. The modulus of elasticity  $E$  for single crystals in pure  $\alpha$  Ti varies between 145 GPa (stress parallel to the  $c$  axis) and 100 GPa (stress perpendicular to the  $c$  axis) because of this anisotropy of the hcp cell. Less pronounced variations in elastic properties are observed in polycrystalline  $\alpha$  Ti with crystallographic texture. For pure Ti, the modulus of elasticity of the  $\beta$  phase cannot be measured at room temperature because this phase is not stable. In multicomponent alloys containing enough  $\beta$  stabilizing elements (for example about 20% Vanadium for Ti-V alloys), the metastable  $\beta$  phase can be retained to room temperature by fast cooling. The value of  $E$  for  $\beta$  phase depends on the stabilizer element but in general has lower modulus of elasticity than the  $\alpha$  phase [1].

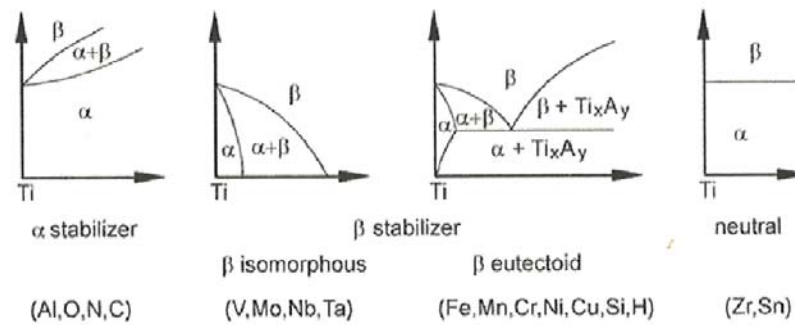


Fig. 2.2. Effect of alloying elements on phase diagrams of titanium alloys [1].

Alloying elements in Ti are classified into  $\alpha$  or  $\beta$  stabilizers (Fig.2.2) where the first ones increase the  $\alpha$  / $\beta$  transition temperature ( $\beta$  transus) of pure Ti (882°C) and the second ones decrease it. The  $\alpha$  stabilizers increase the solute content and they are divided in substitutional or interstitial elements. Al is the most common substitutional element and O, N and C are the most common interstitial elements. Other  $\alpha$  stabilizers are B, Ga, Ge and some rare earth elements but none of them are used commonly because of the lower solubility compared to Al or O. On the other side, the  $\beta$  stabilizers are divided into isomorphous elements and eutectoid elements, depending on the effect that they produce in the phase diagram. The mostly used  $\beta$  isomorphous elements in Ti alloys are V, Mo and Nb. The  $\beta$  eutectoid forming elements Cr, Fe and Si are used in many Ti alloys and others are just used for special purposes. Hydrogen as a  $\beta$  eutectoid forming element led a special process of microstructure refinement called hydrogenation/dehydrogenation (HDH) process but is limited to about 125-150 ppm because of the embrittlement. In addition, some elements (Zr, Hf and Sn) with almost neutral behaviour exist because they lower slightly the  $\beta$  transus but at higher concentrations they increase it.

Commercial Ti alloys are classified basically into three different categories according to their position in the pseudo-binary section through the  $\beta$  isomorphous phase diagram (Fig.2.3):  $\alpha$ ,  $\alpha+\beta$ , and  $\beta$  alloys.

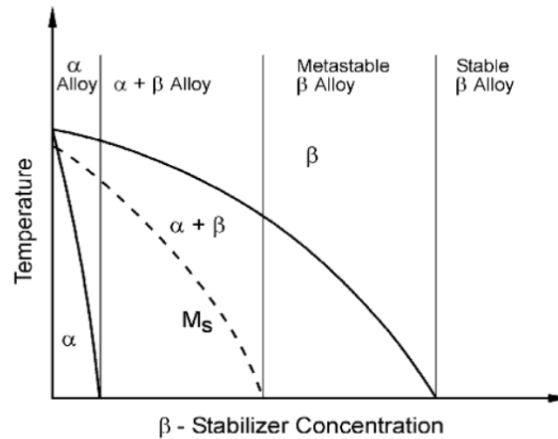


Fig. 2.3. Pseudo-binary section through the  $\beta$  isomorphous phase diagram [1].

### 2.1.2. Phase transformations

In titanium alloys, the transformation from bcc  $\beta$  phase to the hcp  $\alpha$  phase can occur martensitically or by diffusion controlling the nucleation and grain growth process depending on the cooling rate and the alloy composition. The crystallographic orientation between  $\alpha$  and  $\beta$  was studied for Zirconium by Burgers (Burgers relationship), and then was confirmed also for titanium [4]:

$$\begin{aligned} (110)_{\beta} \parallel (0002)_{\alpha} \\ [\bar{1}\bar{1}1]_{\beta} \parallel [11\bar{2}0]_{\alpha} \end{aligned}$$

According to this relationship, a bcc crystal can transform into 12 hcp variants with different orientations with regard to the parent  $\beta$  crystal. The relationship can be used either for the martensite transformation or for the nucleation and growth process.

The martensite transformation involves the movement of atoms by a shear type process, resulting in a homogeneous transformation of the bcc phase into hcp crystal lattice lamellar packages over the given volume. This hcp martensite is designated as  $\alpha'$  and can be observed in two different morphologies: “massive martensite” (lath or packet martensite) and “acicular martensite”.

Massive martensite occurs only in pure Ti, dilute alloys and alloys with high martensitic transformation temperature. The morphology consists in large irregular regions without any clear internal features visible by light microscopy. These regions contain packets of small, almost parallel  $\alpha$  plates or laths belonging to the same Burgers relationship.

Acicular martensite occurs in alloys with higher solute content (lower martensite transformation temperature), and consists of a mixture of individual  $\alpha$  plates with a different Burgers relationship between them. Martensitic plates contain a high dislocation density and sometimes

twins. The hcp  $\alpha'$  martensite is supersaturated in  $\beta$  stabilizers and during the annealing in  $\alpha+\beta$  field decomposes into  $\alpha+\beta$  by precipitating incoherent  $\beta$  particles at dislocations or  $\beta$  layers at plate boundaries.

Increasing the solute content the hcp structure of the martensite becomes distorted and the structure loses its hexagonal symmetry and must be described as orthorhombic ( $\alpha''$ ).

The martensitic start temperature ( $M_s$ ) of pure Ti is about 850°C but depends on the impurity level ( $O_2$ , Fe). Thus increases with increasing the content of  $\alpha$  stabilizers and decreases with increasing amount of  $\beta$  stabilizers. In the alloys where the martensitic reaction is suppressed, the  $\beta$  phase decomposes upon quenching to the so-called athermal  $\omega$  phase.

When titanium alloys are cooled at sufficiently low rates from the  $\beta$  phase field into the  $\alpha+\beta$  phase field the nucleation and growth process take place. Firstly, the  $\alpha$  phase (incoherent with respect to  $\beta$  phase), nucleates preferentially at  $\beta$  grain boundaries leading a continuous  $\alpha$  layer along  $\beta$  grain boundaries. During continued cooling  $\alpha$  plates nucleate either at the interface of the continuous  $\alpha$  layer or at the  $\beta$  grain boundary and grow into the  $\beta$  grain as parallel plates belonging to the same variant of Burgers relationship ( $\alpha$  colony). The  $\alpha$  plates continue to grow until they meet other  $\alpha$  colonies nucleated at other grain boundary areas that belong to different variants of Burgers relationship. The individual  $\alpha$  plates are separated within the  $\alpha$  colonies by the retained  $\beta$  matrix ( $\beta$  plates). The  $\alpha$  and  $\beta$  plates are also called  $\alpha$  and  $\beta$  lamellae and the resulting microstructure is designated lamellar as well according to the 2D metallographic observation (Fig.2.4). It can be seen in Fig.2.4 that the Burgers relationship is obeyed and the flat surface of the  $\alpha$  plates is parallel to the  $(\bar{1}100)$  plane of  $\alpha$  phase and parallel to the  $(\bar{1}12)$  plane of the  $\beta$  phase [1].

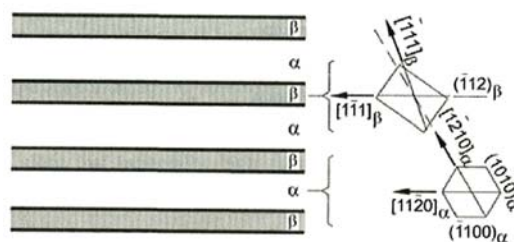


Fig.2.4. Representation of the crystallographic relationship between  $\alpha$  and  $\beta$  plates in  $\alpha$  colonies [1].

Increasing the cooling rate, the size of the  $\alpha$  colonies as well as the thickness of the  $\alpha$  lamellae become smaller. Then, colonies nucleated at  $\beta$  grain boundaries cannot fill the whole  $\beta$  grain and colonies start to nucleate also on boundaries of other colonies by “point contact” on the board face. To minimize the overall elastic strains, the new  $\alpha$  plates tend to grow nearly perpendicular to their originating plate. The nucleation and growth mechanism in combination

with the smaller number of  $\alpha$  plates within the colonies leads to so-called Widmanstätten structure known from the transformation pattern from austenite into ferrite in steel.

### 2.1.3. Commercially pure titanium and $\alpha$ alloys

The group of  $\alpha$  alloys is composed of alloys of various grades of commercially pure (CP) Ti and  $\alpha$  alloys annealed below the  $\beta$  transus that contain small amounts of  $\beta$  phase (2-5 vol%) stabilized by iron. In these alloys, the  $\beta$  phase helps to control the recrystallized  $\alpha$  grains and improves the hydrogen tolerance of these alloys. All  $\alpha$  Ti alloys are based on the low temperature, hexagonal allotropic form of Ti. These alloys can contain substitutional elements (Al or Sn) or interstitial alloying elements (O, C or N) that are soluble in the hcp phase. The  $\alpha$  alloys can also contain small amounts of elements with limited solubility as Fe, V and Mo. Specific alloys have been formulated to improve the environmental resistance of CP Ti and  $\alpha$  Ti alloys to provide comparable performance to alloys where expensive addition as Pd are involved. Consequently, there has been an evolution of these alloys and there are at least 16 different alloys called grades.

The excellent corrosion resistance of CP Ti, compared for example to stainless steel, has made it an attractive material for chemical and petrochemical processing equipment. CP Ti also shows a very good weldability and good general workability, especially for tubing and subsequent shaping. Although CP Ti is more expensive at the outset than stainless steel the pieces made of Ti last longer in service than those of steel [1].

There are four different grades of CP Ti (Table 2.1) and the difference between them is the oxygen content, which goes from 0.18% in grade 1 to 0.40% in grade 4 in order to increase the yield stress level. Fig.2.5 shows the equiaxed microstructure of CP Ti alloys. The  $\alpha$  alloys Ti-0.2Pd (grade 7) and Ti-0.3Mo-0.8Ni (grade 12) offer better corrosion resistance than CP Ti with the iron and oxygen content according to grade 2. The disadvantage of  $\alpha$  alloys is the absence of heat treatment response, but the Ti-3Al-2.5V (half Ti-6Al-4V) is the best  $\alpha$  alloy classified in this aspect and has excellent cold conformability to be used in aerospace applications [5].

CP Ti is always selected for its corrosion resistance and workability. The other  $\alpha$  alloys are used when CP Ti has not enough strength for the intended application.

Alloys which contain a small volume of  $\beta$  phase in equilibrium (less than 10vol%) are called “near  $\alpha$ ” alloys and their usage is at high service temperatures. Near  $\alpha$  alloys are obtained in the range from  $\alpha/\alpha+\beta$  phase boundary up to the intersection of the  $M_s$  line with ambient temperature transforming into martensite by fast cooling from  $\beta$  phase (Fig.2.3). Per definition these alloys belong to  $\alpha+\beta$  alloys but their special features to work at high temperatures permit to treat them like an own group [1].

Name	Alloy composition	T <sub>β</sub> (°C)
Grade 1	CP-Ti (0,2Fe, 0,18O)	890
Grade 2	CP-Ti (0,3Fe, 0,25O)	915
Grade 3	CP-Ti (0,3Fe, 0,35O)	920
Grade 4	CP-Ti (0,5Fe, 0,40O)	950
Grade 7	Ti-0,2Pd	915
Grade 12	Ti-0,3Mo-0,8Ni	880
Ti-5-2,5	Ti-5Al-2,5Sn	1040
Ti-3-2,5	Ti-3Al-2,5V	935
Ti-811	Ti-8Al-1Mo-1V	1040
Ti-6242	Ti-6Al-2Sn-4Zr-2Mo-0,1Si	995

Table 2.1. CP titanium, and most used  $\alpha$  and near  $\alpha$  alloys with chemical composition and  $\beta$  transus temperature [1],[5].

A thermomechanical processing of  $\alpha$  alloys is done to control the crystallographic texture and grain size, but is not used to manipulate the microstructure in a similar manner as is done in  $\alpha+\beta$  alloys and  $\beta$  alloys. The processing of CP Ti starts with either a round ingot or a rectangular cross section slab cast from a cold hearth furnace. This ingot is rolled or forged to create a large slab with a small and uniform grain size. The slab is hot rolled to an intermediate product called hot band. Then the hot band is coiled and depending on the intended finish product gage is either pickled and annealed or just annealed in preparation to the final rolling of the product [1].

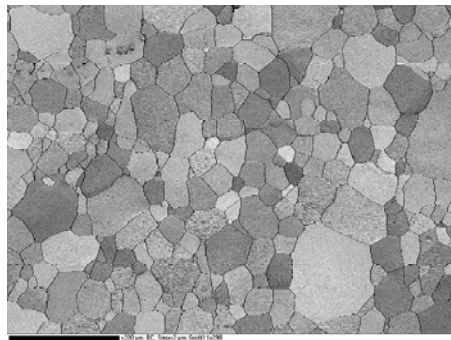
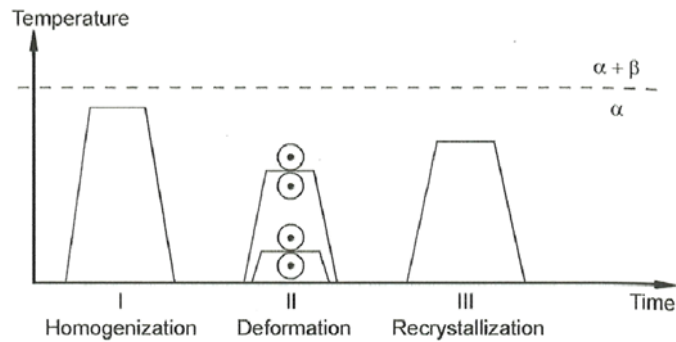


Fig.2.5. EBSD map of the equiaxed microstructure of annealed CP Ti grade 2 [6].

The flexibility and easiness of the processing depends on the CP Ti grade. Fig.2.6 shows the typical processing route for  $\alpha$  alloys consisting of three operations. The  $\alpha$  alloys require less homogenization time because the low solute concentration minimizes any concerns about freezing segregation. Rolling of CP Ti slabs can be done with minimal conditioning because of the good ductility and notch sensitivity. Many of  $\alpha$  alloys can be cold rolled but they are used by seldom in  $\alpha$  non recrystallized condition, because of reduced ductility which constrains subsequent manufacturing options. The microstructure of  $\alpha$  alloys after processing consists of recrystallized  $\alpha$  grains with dispersed  $\beta$  phase [1].

Fig.2.6. Processing route for  $\alpha$  alloys [1].

### 2.1.4. $\alpha+\beta$ alloys

The  $\alpha+\beta$  alloys support a mixture of  $\alpha$  and  $\beta$  phases thus they contain  $\alpha$  and  $\beta$  stabilizers. The Ti6Al4V alloy is the most used and studied  $\alpha+\beta$  alloy and the one investigated in this thesis (Fig.2.7). Although this particular alloy is difficult to form,  $\alpha+\beta$  alloys generally exhibit good manufacturing as well as high room-temperature strength and moderate elevated-temperature strength. The properties of these alloys can be controlled by heat treatment which adjusts the microstructure and precipitation states of the  $\beta$  component [1]. Table 2.2 presents some of the most used  $\alpha+\beta$  alloys.

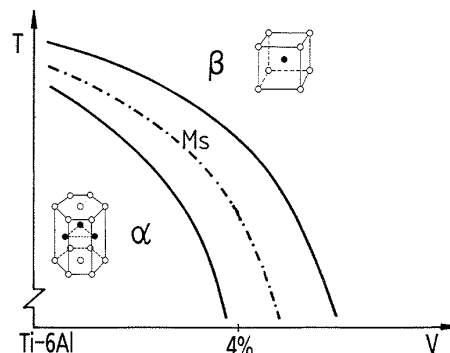


Fig.2.7. Pseudo-binary diagram for Ti-6Al vs V content [5].

Name	Alloy composition	$T_{\beta}$ (°C)
<b>Ti6Al4V</b>	<b>Ti-6Al-4V (0,200)</b>	<b>995</b>
Ti-6-4 ELI	Ti-6Al-4V (0,130)	975
Ti-662	Ti-6Al-6V-2Sn	945
Ti-7-4	Ti-7Al-4Mo	1005

Table 2.2. Most used  $\alpha+\beta$  alloys with chemical composition and  $\beta$  transus temperature [1].

In  $\alpha+\beta$  alloys there are three distinctly different types of microstructures by changing the thermo-mechanical process: fully lamellar structures, fully equiaxed structures, and bi-modal (or duplex) structures containing equiaxed primary  $\alpha$  in a lamellar  $\alpha+\beta$  matrix [1].

### 2.1.4.1. Fully lamellar structures

This microstructure can be obtained in the final steps of the processing route by an annealing treatment after a recrystallization treatment from  $\beta$  phase field as is shown in Fig.2.8. The deformation process (step II) can be done by forging or rolling, either in  $\beta$  phase field or in the  $\alpha+\beta$  phase field. Usually the material is deformed in the  $\beta$  field first taking the advantage of the lower flow stress and then deformed in the  $\alpha+\beta$  phase to avoid large  $\beta$  grain sizes [1].

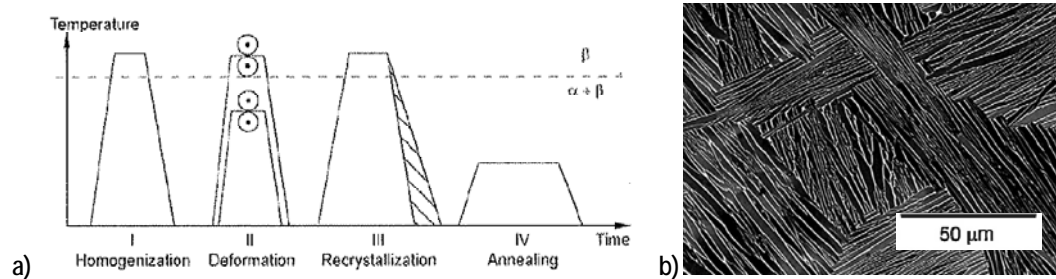


Fig.2.8. a) Processing route [1] and b) lamellar microstructure of  $\alpha+\beta$  alloys [7].

The recrystallization temperature in step III is set 30-50°C above the  $\beta$  transus to maintain control of the  $\beta$  grain size. The most important parameter in the processing route is the cooling rate from  $\beta$  field in step III to determine the characteristic features of the lamellar structure: size of  $\alpha$  lamellae ( $\alpha$  plates or laths), colony size and thickness of  $\alpha$  lamellae at  $\beta$  grain boundaries. All of these values decrease by increasing the cooling rate.

In step IV (final annealing heat treatment) the temperature is more important than the time because the temperature determines whether age-hardening of the  $\alpha$  phase by  $\text{Ti}_3\text{Al}$  particles occurs or not. In the Ti6Al4V the  $\text{Ti}_3\text{Al}$  solvus temperature is about 550°C. In addition, depending on the cooling rate in step III, fine  $\alpha$  platelets can precipitate in the  $\beta$  phase during the heat treatment in step IV.

There is another type of fully lamellar structures namely  $\beta$  processed condition, but this condition is not used in commercial application (Fig.2.9). In case of  $\beta$  processing, there is no step III and the material remains in a non recrystallized condition. The resulting shape of the grains depends on the deformation mode (rolling, forging, pressing, etc.) and on the deformation degree, but the latter determines also the width of deformed  $\beta$  grains. The advantage of this process is that the  $\alpha$  colony size is limited at least in one direction by the  $\beta$  grain width and the continuous  $\alpha$  layers are broken up. The cooling rate after the deformation process is also important to determine the  $\alpha$  lamellae width and the  $\alpha$  colony size [1].

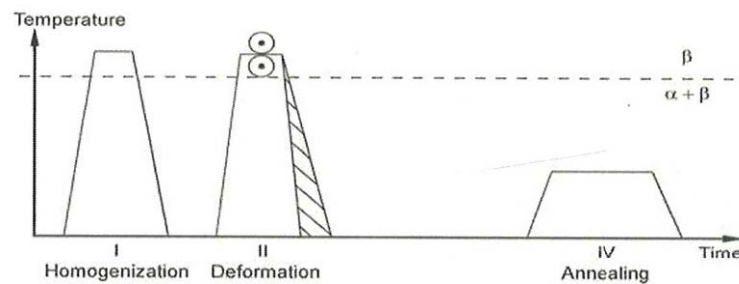


Fig.2.9. Processing route for  $\beta$  processed microstructures of  $\alpha+\beta$  alloys [1].

#### 2.1.4.2. Bi-modal structures

The process to obtain bi-modal (duplex) structures is divided into four different steps (Fig.2.10): homogenization in  $\beta$  phase field (step I), deformation in  $\alpha+\beta$  phase field (step II), recrystallization in the  $\alpha+\beta$  phase field (step III) and final ageing or stress relieving treatment (step IV). The main parameter of the processing route is the cooling rate from step I, because it determines the width of  $\alpha$  lamellae that will be afterwards deformed and recrystallized. In the step II the lamellar structure is deformed plastically (not broken up) with enough stored energy (dislocations) to obtain complete recrystallization of the  $\alpha$  and  $\beta$  phases during step III. In addition, in step II crystallographic textures in the hcp  $\alpha$  phase and in the bcc  $\beta$  phase can develop to influence the mechanical properties [1].

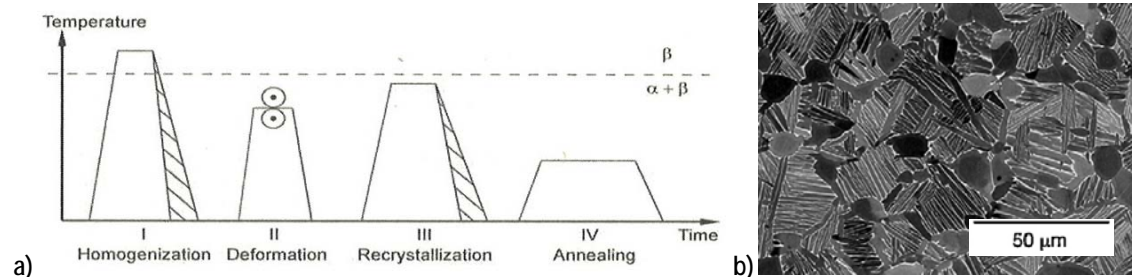


Fig.2.10. a) Processing route [1] and b) bi-modal microstructure of  $\alpha+\beta$  alloys [7].

At low deformation temperatures (higher volume of  $\alpha$  present during deformation), an  $\alpha$ -deformation texture develops. On the other hand at high deformation temperatures in the  $\alpha+\beta$  field (a high volume of  $\beta$  phase is present during deformation), a  $\beta$ -deformation texture develops. The resulting textures of the hcp phase will not change significantly during the subsequent recrystallization step. The most important parameter in step III is the temperature, which determines the volume fraction of recrystallized equiaxed  $\alpha$  primary placed in the corners (triple-points) of the recrystallized  $\beta$  grains. The content and size of  $\alpha$  is defined by the  $\beta$  grain size, which is about the distance between  $\alpha$  primary grains. The annealing time in step III is not very critical if it is enough to generate isolated equiaxed primary  $\alpha$  grains. Grain growth is very slow in the mixture between primary  $\alpha$  and  $\beta$  grains. During separation into primary  $\alpha$

and  $\beta$ , a redistribution of alloying elements takes place, where strong  $\alpha$  (Al, O) and  $\beta$  stabilizers (V, Mo) will diffuse into the two phases, respectively. This effect has the consequence that  $\alpha$  lamellae formed in the  $\beta$  grains during cooling in step III have a lower concentration of those elements (Al, O). That promotes age-hardening by the formation of  $Ti_3Al$  particles in step IV, as compared to  $\alpha$  primary or fully lamellar structures. Substantial volume fractions of these coherent particles can be precipitated in the  $\alpha$  phase in Ti-6Al-4V (IMI550) at 500°C, in Ti-6Al-4V (IMI685) at 550°C, in Ti-6242 at 590°C or even in IMI 834 at 700°C. In bi-modal structures the cooling rate in step III mainly influences the width of the individual  $\alpha$  lamellae whereas the  $\alpha$  colony size and the length of continuous  $\alpha$  layers at  $\beta$  grain boundaries are determined by the  $\beta$  grain size [1].

### 2.1.4.3. Fully equiaxed structures

There are two different processing routes to obtain fully equiaxed microstructures. The first one is identical to the processing route to obtain a bi-modal microstructure but with a lower cooling rate in step III (Fig 2.11). If the cooling rate in step III is sufficiently low, only the  $\alpha$  grains will grow and no  $\alpha$  lamellae are formed within the  $\beta$  grains, resulting a fully equiaxed structure with the equilibrium volume of  $\beta$  phase located at the “triple-points” of the  $\alpha$  grains [1].

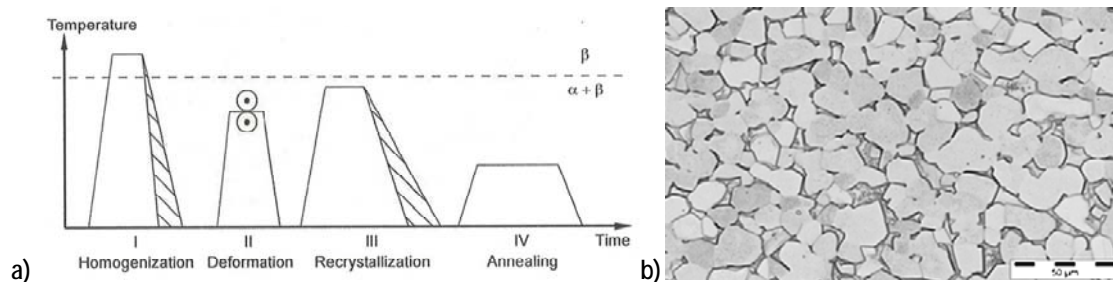


Fig.2.11. a) Processing route [1] and b) fully equiaxed microstructure of  $\alpha+\beta$  alloys slowly cooled in step III [7].

The second possibility (Fig.2.12) to obtain a fully equiaxed microstructure, is to recrystallize in step III at low temperature, when the equilibrium volume fraction of  $\alpha$  phase at that temperature is high enough to form the fully equiaxed microstructure directly from the deformed lamellar structure during step II. The mechanism, that changes the deformed lamellar microstructure is the same as in the bi-modal microstructure but in the opposite direction:  $\alpha$  phase penetrates along the  $\beta/\beta$  grain boundaries into the recrystallized  $\beta$  lamellae causing the separation of  $\beta$  grains in the final microstructure. Using this second processing route, smaller  $\alpha$  grains can be achieved as compared to the first method [1].

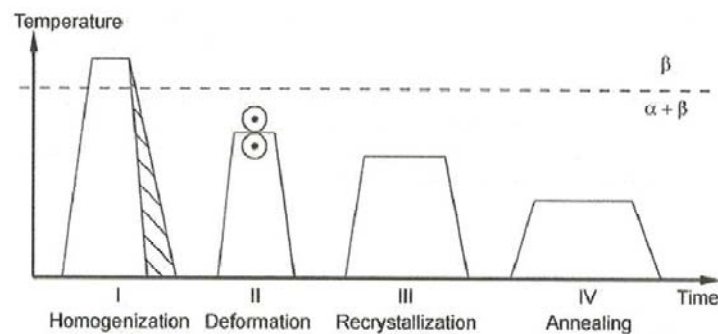


Fig.2.12. Processing route for fully equiaxed microstructures of  $\alpha+\beta$  alloys recrystallized at low temperatures [1].

A fast cooling rate in step I is a necessity to obtain fully equiaxed microstructures with small  $\alpha$  grain sizes via the second method described. During step IV secondary  $\alpha$  plates can be formed in the  $\beta$  phase even in fully equiaxed microstructures depending on the difference of temperature between step III and step IV or depending on the cooling details in step III for the first method.

Fully equiaxed microstructures can be changed to bi-modal microstructures by heating the material up to the temperature in  $\alpha+\beta$  phase field corresponding to the desired  $\alpha$  primary volume fraction and subsequently cooling with a sufficiently high rate to form  $\alpha$  lamellae within the  $\beta$  grains. It's also possible to change from a bi-modal structure to fully equiaxed structure. This is possible by heating the material in  $\alpha+\beta$  phase field at a temperature, high enough to dissolve  $\alpha$  lamellae and cools down slowly to allow the growth of  $\alpha$  primary. In a similar way the volume fraction of  $\alpha$  primary in bi-modal structures can be changed. Another important thing is that after each heat treatment the  $\alpha$  grain size and  $\beta$  grain size will be increased.

The so-called mill-annealed condition is a very common process where the recrystallization step is omitted (Fig.2.13). Consequently the deformation details in step II determine the resulting microstructure (especially the degree of recrystallization). The final annealing step is done at higher temperatures than the  $Ti_3Al$  solvus temperature and just for stress relieving [1].

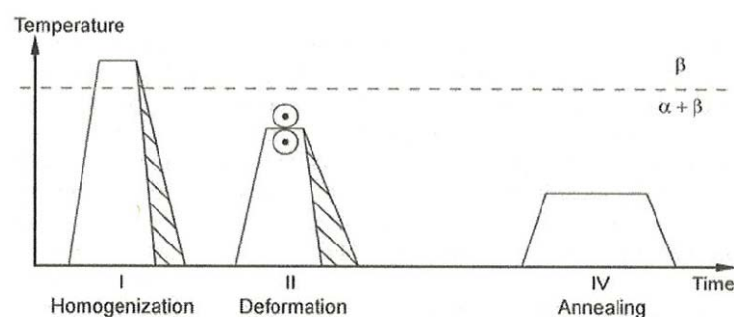


Fig.2.13. Processing route for fully mill-annealed microstructures of  $\alpha+\beta$  alloys [1].

### 2.1.5. $\beta$ alloys

In contrast to  $\alpha+\beta$  alloys,  $\beta$  alloys do not transform martensitically. Upon quenching to room temperature a metastable  $\beta$  phase is formed. The  $\alpha$  can precipitate very fine from the metastable  $\beta$  phase. The main feature of  $\beta$  alloys is that they can be hardened to much higher yield stress levels than  $\alpha+\beta$  alloys. In addition, these alloys can be processed at lower temperatures than  $\alpha+\beta$  alloys and some heavily stabilized  $\beta$  alloys are cold conformable. The corrosion resistance of  $\beta$  alloys is equal or better than that of  $\alpha+\beta$  alloys, especially in environments with the presence of hydrogen because the  $\beta$  phase has a higher hydrogen tolerance than the  $\alpha$  phase.

The so-called “high strength”  $\beta$  alloys or “near  $\beta$ ” alloys are located with their chemical composition close to the  $\beta/\alpha+\beta$  phase boundary (see Fig.2.3) and contain a high volume fraction of  $\alpha$ . In addition, there are the “heavily stabilized”  $\beta$  alloys which are located more to the right in the pseudo-binary phase diagram (Fig.2.3) with lower content of  $\alpha$  fraction volume and lower strength compared with “high strength” alloys [1].

The Ti-6246, Ti-17, Beta-CEZ and Ti-10-2-3 alloys shown in Table 2.3 correspond to the first group of alloys, whereas the alloys Beta 21S, Ti-15-3 and Beta-C belong to the second group of alloys.

Name	Alloy composition	$T_{\beta}$ (°C)
Ti-6246	Ti-6Al-2Sn-4Zr-6Mo	940
Ti-17	Ti-5Al-2Sn-2Zr-4Mo-4Cr	890
Beta-CEZ	Ti-5Al-2Sn-2Cr-4Mo-4Zr-1Fe	890
Ti-10-2-3	Ti-10V-2Fe-3Al	800
Beta 21S	Ti-15Mo-2.7Nb-3Al-0.2Si	810
Ti-15-3	Ti-15V-3Cr-3Al-3Sn	760
Beta-C	Ti-3Al-8V-6Cr-4Mo-4Zr	730

Table 2.3. Important  $\beta$  alloys with chemical composition and  $\beta$  transus temperature [1] [5].

The  $\beta$  annealed microstructure (Fig.2.14b) illustrates the key feature of  $\beta$  alloys namely the continuous  $\alpha$  layers at the  $\beta$  grain boundaries [1].

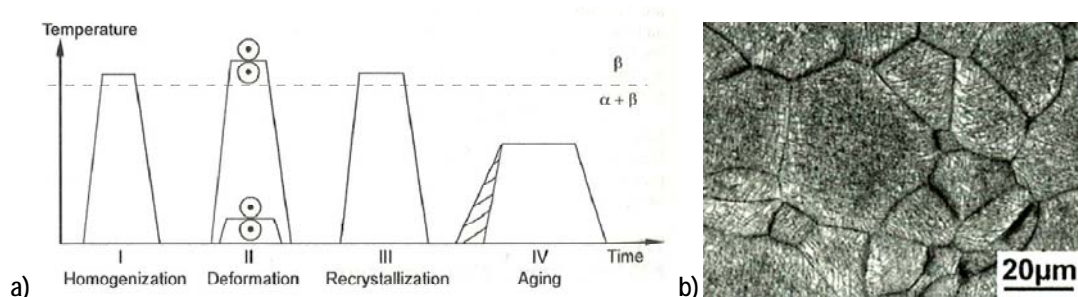


Fig.2.14. a) Processing route [1] and b)  $\beta$  annealed microstructures of heavily stabilized  $\beta$  Ti alloys [1].

Sometimes it is difficult to obtain a homogeneous distribution of  $\alpha$  platelets by the normal one-stage ageing of heavily stabilized  $\beta$  alloys. That’s why sometimes a pre-ageing is necessary to

form a distribution of fine  $\alpha$  platelets and a subsequent ageing where the platelets will grow and coarser (Fig.2.15).

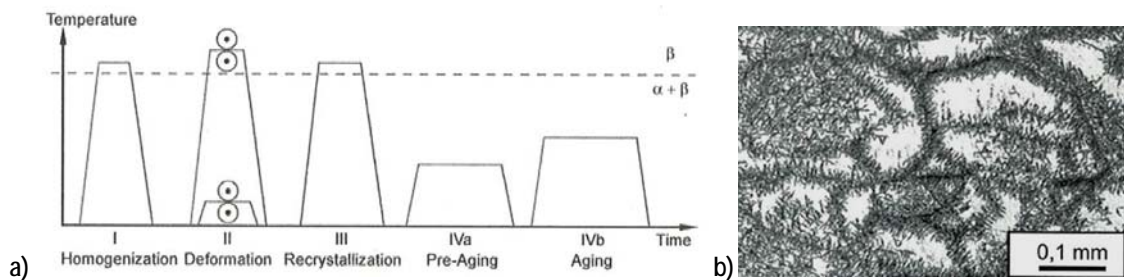


Fig.2.15. a) Processing route for  $\beta$  annealed microstructures with pre-ageing step [1] b) Effect of pre-ageing step IVa [7].

A final heat treatment in the  $\alpha+\beta$  field is usually done for high strength  $\beta$  alloys in two steps (Fig.2.16): annealing (step IVa) to precipitate a desired volume fraction of coarse  $\alpha$  plates, and ageing to form the  $\alpha$  fine platelets [1].

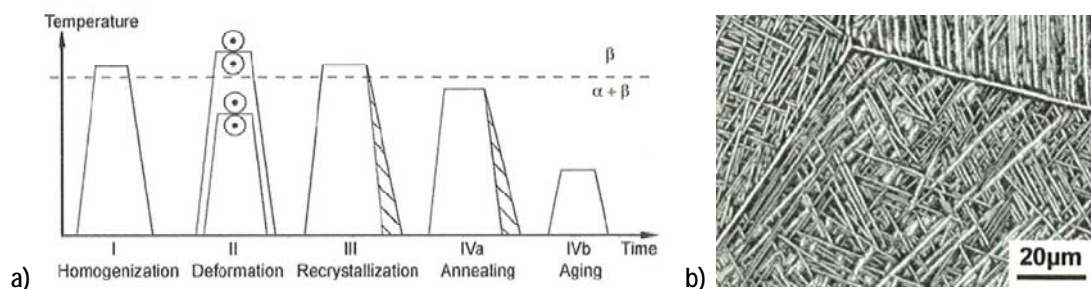


Fig.2.16 a) Processing route [1] and b)  $\beta$  annealed microstructures of high strength  $\beta$  Ti alloys [1].

In the processing route for  $\beta$  processed microstructures (Fig.2.17) the recrystallization step III is omitted to create non recrystallized microstructure with deformed  $\beta$  grains. Then the  $\alpha$  layers formed on  $\beta$  grain boundaries will take a the local shape of the deformed  $\beta$  boundaries [1].

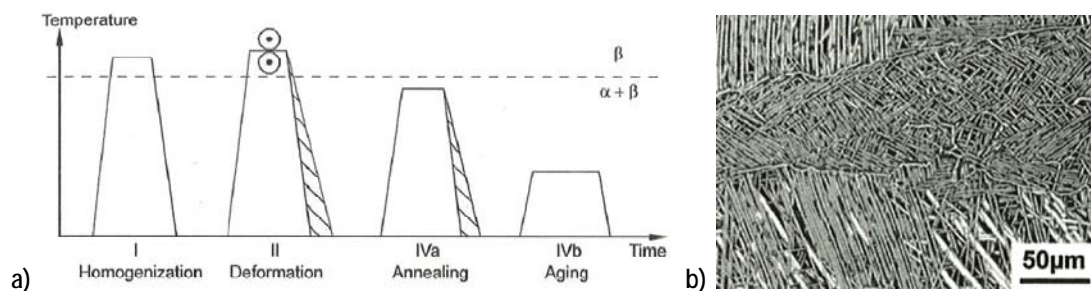


Fig.2.17 a) Processing route [1] and b)  $\beta$  processed microstructure of  $\beta$  Ti alloys [1].

The benefit of bi-modal microstructures in  $\beta$  alloys is to compensate the continuous  $\alpha$  layers at  $\beta$  grain boundaries by creating a small enough  $\beta$  grain size. The processing route for these alloys is shown in Fig.2.18. The recrystallization annealing temperature (step III) determines the volume fraction of primary  $\alpha$  and also has an influence on the size of the recrystallized and

equiaxed  $\beta$  grains. Afterwards the intermediate annealing (step IVa) is done to precipitate coarse  $\alpha$  plates and the final ageing (step IVb) to form the small  $\alpha$  platelets [1].

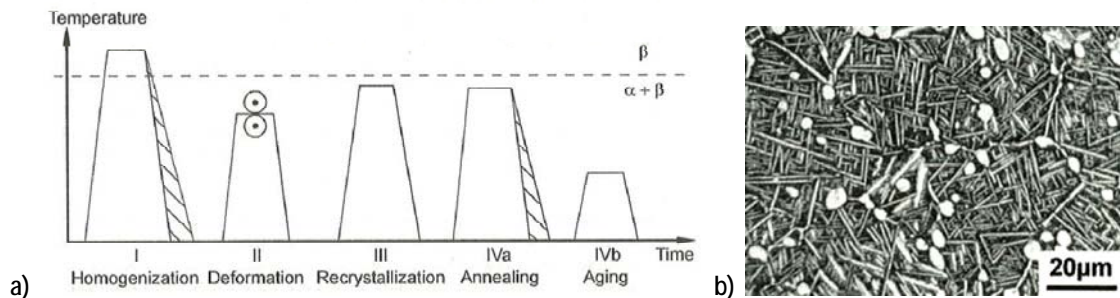


Fig.2.18. a) Processing route [1] and b)  $\beta$  bi-modal microstructure of  $\beta$  Ti alloys [1].

### 2.1.6. Mechanical properties

For  $\alpha + \beta$  alloys as well as for the  $\beta$  alloys, the mechanical properties which are relevant for a particular application are optimized through the microstructural control. The knowledge of the microstructure-properties relationship and the evolution of the microstructure as a result of processing, are requisites to optimize the material properties. Table 2.4 and Table 2.6, show the experimentally observed influences of microstructural parameters on the particular mechanical property of  $\alpha + \beta$  alloys and  $\beta$  alloys. The influences are indicated by “+” (improvement), “-” (degradation), or “0” (no significant influence) [8].

$\alpha + \beta$ Titanium alloys	$\sigma_{0,2}$	$\epsilon_F$	HCF	Microcracks $\Delta K$	Macrocracks			Creep Strength 0,2%
					$\Delta K$ R=0,7	$K_{Ic}$	$\Delta K$ R=0,1	
Fully lamellar microstructure	+	-	+	+	0	0	0	+
Age-hardened microstructure	+	-	+	-	-	-	+	+
Bi-modal microstructure	+	+	-	+	-	-	-	-
Grain boundary $\alpha$ -layers	0	-	-	-	0	-	0	0
Small $\alpha$ -colonies $\alpha$ -lamellae	+	+	+	+	-	-	-	-
Texture in Deformation direction	+	0	Vac +	0	0	0	0	Vac
			Air -	-	-	0	-	Air

$\sigma_{0,2}$ : Yield stress  
 $\epsilon_F$ : Final strain  
 HCF: High cycle fatigue  
 $\Delta K$ : Stress intensity factor  
 $K_{Ic}$ : Critical fracture toughness

Table 2.4. Influence of microstructural parameters on mechanical properties of  $\alpha + \beta$  Ti-alloys [8].

In  $\alpha + \beta$  alloys the dominant difference between the bi-modal and fully lamellar microstructure is the greatly reduced grain size. This reduction has a pronounced effect on the effective slip length, which is essentially equivalent to the colony size. In fully lamellar structures with large  $\beta$  grain size, the colony size is also large ( $\sim 100 \mu\text{m}$ ) and in bi-modal the colony size cannot exceed the  $\beta$  grain size ( $\sim 20-50 \mu\text{m}$ ). As a rule, a reduction in pile-up length improves both yield stress (+) and ductility (+). This effect is shown in for Ti-6Al-4V in Table 2.5 [8].

	$\sigma_{0,2}$ (MPa)	Tens. Elong (%)
Ti-6Al-4V Bi-modal	950	22
Ti-6Al-4V Fully lamellar	880	7

Table 2.5. Comparison of yield stress and ductility for bi-modal and lamellar structures in Ti-6Al-4V  $\alpha+\beta$  alloy [8].

$\beta$ Titanium alloys	$\sigma_{0,2}$	$\epsilon_F$	HCF	Microcracks $\Delta K$	Macrocracks			Creep Strength 0,2%
					$\Delta K$ R=0,7	$K_{Ic}$	$\Delta K$ R=0,1	
Over ageing microstructure	-	+	-	+	+	+	+	-
Grain boundary $\alpha$ -layers	0	-	-	-	0	-	0	0
Bi-modal microstructure	0	+	+	+	-	-	-	0

$\sigma_{0,2}$ : Yield stress  
 $\epsilon_F$ : Final strain  
 HCF: High cycle fatigue  
 $\Delta K$ : Stress intensity factor  
 $K_{Ic}$ : Critical fracture toughness

Table 2.6. Influence of microstructural parameters on mechanical properties of  $\beta$  Ti-alloys [8].

Due to the nature of precipitation reaction in  $\beta$  alloys,  $\alpha$  plates are precipitated in the twelve possible orientations, thus slip transfer over large distances (commonly observed in  $\alpha+\beta$  alloys) is not possible in  $\beta$  alloys. Increasing the ageing temperature or time the  $\alpha$  plates coarsen (over ageing) and the yield stress decreases (-) and the ductility increases (+).

The major difference in the bi-modal and lamellar microstructures for  $\beta$  alloys is the much finer  $\beta$  grain size for the bi-modal structure. There is no influence of the grain size on the yield stress (0), since the slip length is controlled by the spacing of the  $\alpha$  plates rather than the grain size [8].

### 2.1.7. Applications

Titanium and its alloys have proven to be technically superior and cost-effective materials of construction for a wide variety of aerospace, industrial, marine and commercial applications. In North America, approximately 70% of the titanium consumed is utilized for aerospace applications. Due to the expansion of existing applications and the development of new uses, the greatest growth occurs in the industrial, marine and commercial sectors.

Titanium is immune to corrosive attack by salt water or marine atmospheres. It also exhibits exceptional resistance to a wide range of acids, alkalis, natural waters and industrial chemicals. Titanium alloys offers as well a superior resistance to erosion, cavitation or impingement attack. In service conditions, the heat transfer properties of titanium approximate those of admiralty brass and cupronickel due to its advantages: the higher strength permits to use thinner walled equipment, the relative absence of corrosion generally results in a bright and smooth surface which improves the lamellar flow, and titanium's excellent erosion-corrosion resistance permits significantly higher operating velocities [9].

### **2.1.7.1. Aerospace applications**

Aerospace industry is the largest market for titanium products primarily due to the exceptional strength to weight ratio, elevated temperature performance and corrosion resistance. Titanium applications are most significant in jet engine and airframe components that are subject to temperatures up to 600°C and for other critical structural parts. Usage is widespread in most commercial and military aircrafts. Titanium is also used in spacecraft where the many benefits of titanium are effectively utilized [9].

### **2.1.7.2. Industrial applications**

Highly efficient gas turbine engines are possible only through the use of titanium-based alloys in components like fan blades, compressor blades, discs, hubs and numerous non-rotor parts.

A major industrial application for titanium remains in heat transfer applications in which the cooling medium is seawater, brackish water or polluted water.

Because of high toughness, high strength and exceptional erosion/corrosion resistance, titanium is currently being used for submarine ball valves, fire pumps, heat exchangers, castings, hull material for deep sea submersibles, water jet propulsion systems, shipboard cooling and piping systems.

Titanium vessels, heat-exchangers, tanks, agitators, coolers, and piping systems are utilized in the processing of aggressive compounds, like nitric acid, organic acids, chlorine dioxide, inhibited reducing acids and hydrogen sulphide [9].

### **2.1.7.3. Biomedical applications**

Titanium is a standard material for medical applications such as hip joints, bone screws, knee joints, bone plates, dental implants, surgical devices, pacemaker cases and centrifuges due to its total resistance to attack by body fluids, high strength and low modulus. The body readily accepts titanium since it is more biocompatible than stainless steel or cobalt chrome. Titanium also has higher fatigue strength than many other metals. The unique qualities of titanium prove to be MRI (Magnetic Resonance Imaging) and CT (Computed Tomography) compatible [9].

## **2.2. Methodology**

### **2.2.1. Metallography**

#### **2.2.1.1. Light optical microscopy (LOM)**

The optical microscope uses visible light and a system of lenses to magnify images of small samples. Optical microscopes are the oldest design of microscope and the basic optical microscopes can be very simple, although there are many complex designs which aim to improve resolution and sample contrast. Optical microscopes have an extended usage because they use visible light and can be directly observed by eye. The resolution is limited by the wave length of light ( $>0.3\mu\text{m}$ ).

The image from an optical microscope can be captured by normal light-sensitive cameras to generate a micrograph. Originally images were captured by photographic film but modern developments in CMOS and later charge-coupled device (CCD) cameras allow the capture of digital images. Purely digital microscopes are now available which just use a CCD camera to examine a sample, and the image is shown directly on a computer screen without the need for eye-pieces.

A compound microscope is a microscope which uses multiple lenses to collect light from the sample and then a separate set of lenses to focus the light into the eye or camera. Compound microscopes are heavier, larger and more expensive than simple microscopes due to the increased number of lenses used in construction. The main advantages of multiple lenses are improved numerical aperture, reduced chromatic aberration and exchangeable objective lenses to adjust the magnification. A compound microscope also makes more advanced illumination setups, such as phase contrast [10].

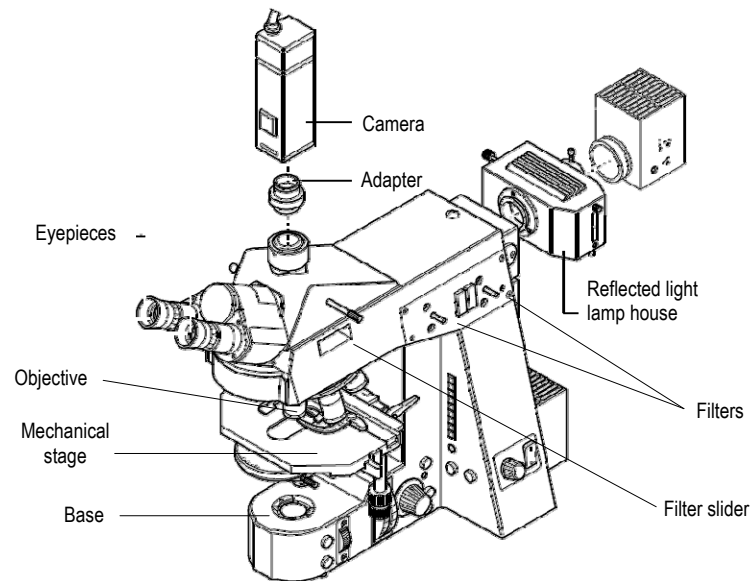


Fig.2.19. Components of a compound modern microscope with digital camera mainly used in metallography [11].

Reflected light microscopy is often referred to as incident light, epi-illumination, or metallurgical microscopy, and is the method of choice for fluorescence and for imaging specimens that remain opaque. Because light is unable to pass through these specimens, it must be directed onto the surface and returned to the microscope objective by either specular or diffused reflection. Light that is returned upward can be captured by the objective in accordance with the objective's numerical aperture and then passes through the partially silvered mirror. The vertical illuminator should also make provision for the insertion of filters for contrast and photomicrography, polarizers, analyzers, and compensator plates for polarized light and differential interference contrast illumination [10]. Fig.2.19 shows a common LOM microscope used in metallography analysis.

Specific techniques of light have been found for the evaluation of the grain size for two phase titanium alloys. A complete quantitative description of microstructure for  $\alpha+\beta$  titanium alloys should include data about three elements: grains, colonies and lamellae. Due to considerable differences in the size and lack of features unambiguously distinguishing these microstructural elements from one another, it is not possible to apply one observation technique to determine the stereological parameters of grains, colonies and lamellae of the phases  $\alpha$  and  $\beta$  simultaneously. For the evaluation of the sizes of grains and colonies, images obtained by means of special techniques of light microscopy (LOM) can be used, whereas the quantitative characterization of the  $\alpha$  phase lamellae should be carried out on images obtained by means of scanning electron microscopy (SEM).

By optical microscopy usually the contrast between the  $\alpha$  phase lamella colonies is too small to be use for image analysis. The methods of observation in polarized light can be applied when

the examined material is characterized by optical anisotropy. Observations in dark field gave better results than in bright field and the best results are obtained during the observation in polarized light. By changing the setting angle of the polarizer against the analyzer during the observation in polarized light, it is possible to obtain images on which the same microstructural element has a different gray level. However, for image analysis it's required to record at least several images of the microstructure from the same place in the specimen. The difficulties connected with the necessity of recording many images can be eliminated thanks to the application a lambda filter during the observation in polarized light. Such an image can be subjected to colour separation according to the selected model of colours (e.g. RGB, CMYK, HSB and HLS). The investigations of the titanium alloy microstructures showed that the best results are achieved using the CMYK model (C = cyan, M=magenta, Y= yellow, K= black) [12]. An example of this process is observed in Fig.2.20.

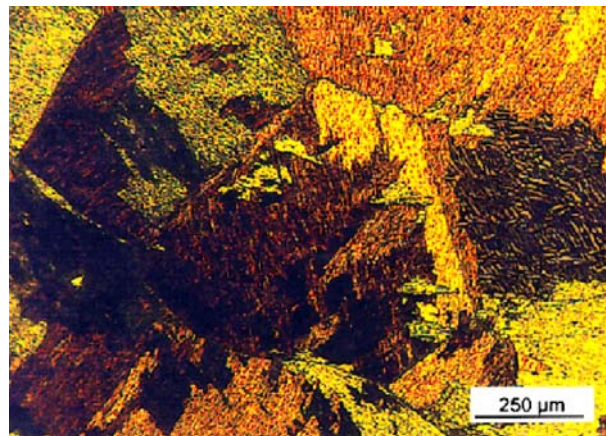


Fig.2.20. Microstructure of a Ti-6Al-2Mo-2Cr-Fe alloy annealed in  $\beta$  field obtained in polarized light with lambda filter [12].

### 2.2.1.2. Scanning electronic microscopy (SEM)

The scanning electron microscope (SEM) uses a focused beam of high-energy electrons to generate a variety of signals at the surface of solid specimens. The signals that derive from electron-sample interactions reveal information about the sample including external morphology (topography), chemical composition, and crystalline structure and orientation of materials (EBSD). In most applications, data are collected over a selected area of the surface of the sample, and a two-dimensional image is generated that displays spatial variations in these properties. Areas ranging from approximately 1 cm to 5 microns in width can be imaged in a scanning mode using conventional SEM techniques (magnification ranging from 20X to approximately 100,000X, on massive samples spatial resolution of 0.1 $\mu$ m can be achieved). The SEM is also capable of performing analyses of selected point locations on the sample; this approach is especially useful to determine chemical compositions (wave length or energy

dispersive EDX), crystalline structure, and crystal orientations (using EBSD) qualitatively or semi-quantitatively [10].

Accelerated electrons in SEM carry significant amounts of kinetic energy, and this energy is dissipated as a variety of signals produced by electron-sample interactions when the incident electrons are decelerated in the solid sample. These signals include secondary electrons and backscattered electrons (BSE) that produce SEM images, diffracted backscattered electrons (EBSD that are used to determine crystal structures and their orientations), photons (characteristic X-rays that are used for elemental analysis and continuum X-rays), visible light (cathodoluminescence-CL), and heat. Secondary electrons and backscattered electrons are commonly used for imaging samples: secondary electrons are most valuable for showing morphology and topography samples and backscattered electrons are most valuable for illustrating contrasts in composition in multiphase samples (i.e. for rapid phase discrimination). X-ray generation is produced by inelastic collisions of the incident electrons with electrons in discrete orbitals (shells) of atoms in the sample. As the excited electrons return to lower energy states, they yield X-rays that are of a fixed wavelength (that is related to the difference in energy levels of electrons in different shells for a given element). Thus, characteristic X-rays are produced for each element in a material that is "excited" by the electron beam allowing for EDX. SEM analysis is considered to be "non-destructive"; that is, x-rays generated by electron interactions do not lead to volume loss of the sample, so it is possible to analyze the same materials repeatedly [10].

Essential components of all SEMs include the following (Fig.2.21):

- Electron Source ("Gun")
- Electron Lenses
- Sample Stage
- Detectors for all signals of interest
- Display / Data output devices
- Infrastructure Requirements:
  - Power Supply
  - Vacuum System
  - Cooling system
  - Vibration-free floor
  - Room free of ambient magnetic and electric fields

SEMs always have at least one detector (usually a secondary electron detector), and most have additional detectors. The specific capabilities of a particular instrument are critically dependent on which detectors it accommodates [13].

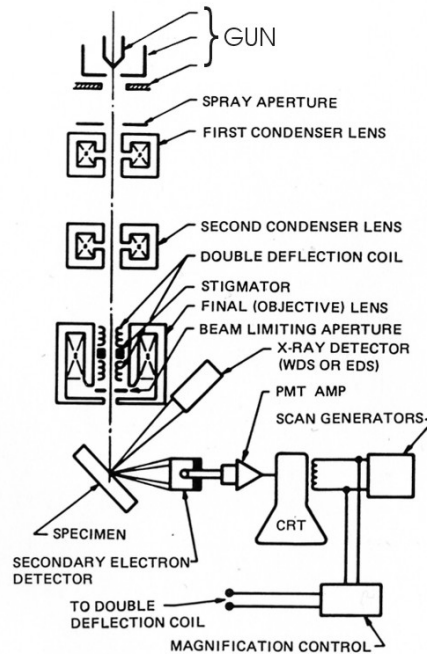


Fig.2.21. Diagram of the components in a SEM [13].

Field Emission Gun Scanning Electron Microscope (FEG-SEM) provides high spatial resolution and contrast (1nm at 15kV) and can operate at low operating voltages (5kV) because the field-emission cathode in the electron gun. The field emission gun is used to produce an electron beam that is smaller in diameter, more coherent and with up to three orders of magnitude greater current density or brightness than can be achieved with conventional thermionic emitters such as tungsten or lanthanum hexaboride ( $\text{LaB}_6$ )-tipped filaments. The result is a significantly improved signal-to-noise ratio and spatial resolution, and greatly increased emitter life and reliability compared with thermionic devices [14]. The high brightness allows the spatial resolution of x-ray analysis by Energy Dispersive Spectroscopy (EDS) to be optimised [15].

#### 2.2.1.2.1. BSE mode

Interaction of an accelerated electron beam with a sample target produces a variety of elastic and inelastic collisions between electrons and atoms within the sample. Elastic scattering changes the trajectory of the incoming beam electrons when they interact with a target sample without significant change in their kinetic energy. In this case, we can think of elastic scattering in terms of a "billiard-ball" model of small particles (electrons) colliding with large particles (atoms). Larger atoms (with a greater atomic number,  $Z$ ) have a higher probability of producing

an elastic collision because of their greater cross-section. Consequently, the number of backscattered electrons (BSE) reaching a BSE detector is proportional to the mean atomic number of the sample. Thus, a "brighter" BSE intensity correlates with greater average  $Z$  in the sample, and "dark" areas have lower average  $Z$ . BSE images are very helpful for obtaining high-resolution compositional maps of a sample and for quickly distinguishing different phases [10].

The resolution of  $\sim 1\mu\text{m}$  afforded using the SEM microscope in BSE mode especially compared with other available techniques (e.g. optical micrographs) is of paramount importance to provide the highest fidelity to quantify microstructural data in titanium alloys. The BSE micrographs of  $\alpha+\beta$  titanium alloys show the two distinct phases  $\alpha$  and  $\beta$  by their relative contrasts as a result of their respective average atomic mass. The  $\alpha$  phase stabilized by elements with a low atomic number (e.g., Al and O) appears darker relative to the  $\beta$  phase, stabilized by the heavier elements (e.g., V and Fe) [16].

#### 2.2.1.2.2. EBSD technique

Accelerated electrons in the primary beam of the SEM can be diffracted by atomic layers in crystalline materials. These electrons are diffracted along cones which can be detected when they impinge on a phosphor screen and generate visible lines, called Kikuchi bands, or "EBSP's" (electron backscatter patterns). These patterns are effectively projections of the geometry of the lattice planes in the crystal, and they give direct information about the crystalline structure and crystallographic orientation of the grain from which they originate. When the patterns are used in conjunction with a data base that includes crystallographic structure information of the material phases, these data can be used to identify phases based on crystal structure and also to perform analyses on polycrystalline systems [13].

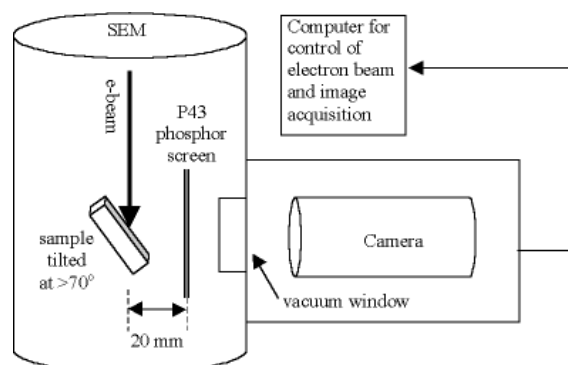


Fig.2.22. Scheme of the EBSD measurement array [13].

The polished sample is placed in the SEM and inclined approximately  $70^\circ$  relative to normal incidence of the electron beam (Fig.2.22). The detector is actually a camera equipped with a

phosphor screen integrated with a digital frame grabber. The pattern of Kikuchi lines on the phosphor screen is electronically digitized and processed to recognize the individual Kikuchi lines.

EBSD is currently the fastest and most reliable way to acquire data for crystalline structure and orientation in a solid crystalline phase. The data give true 3-dimensional orientations for individual crystals, which is superior to optical pole figures which give 2-dimensional orientations. These data can be used to reveal systematic textural relations between individual grains or phases and even to determine relative abundances of phases in a polyphase sample [13]. A surface free of surface deformation is a prerequisite for EBSD.

### 2.2.1.3. Image analysis

The properties in Ti alloys are dependent upon the microstructural features. However, there is no model which accurately predicts the mechanical properties of a microstructure given by a set of microstructural variables. Indeed the best tools available establish whether a microstructural feature has a positive (+), negative (-) or neutral (0) influence on the mechanical properties of Ti alloys. The absence of a physically based model is largely predicted by the complicated interdependences that exist among the microstructural features. A solution to the complex problem of isolating and quantifying the magnitude of the functional dependences of a property on the microstructure or processing route involves the use of expert systems. The fidelity of a solution provided by any expert-based approach is dictated by the quality and amount of the data used to train it. Thus for the development of neural networks based on databases relating microstructures and mechanical properties, it is essential to develop rigorous procedures for providing an accurate, quantified description of a multitude of microstructural features present in the digital micrograph [16].

In  $\alpha+\beta$  Ti alloys such as Ti-6Al-4V, the microstructural features that should be considered to identify for quantification are [16]:

- **Mean equiaxed  $\alpha$  size**

Image process from SEM backscattered image (Fig.2.23):

- 1- Separate individual particles from clusters (manual step) based in an “equiaxe” criterion.
- 2- Mean intercept method (plug-in) using a program for image analysis (e.g. *Forvea*) to determine the size of the equiaxed  $\alpha$ .

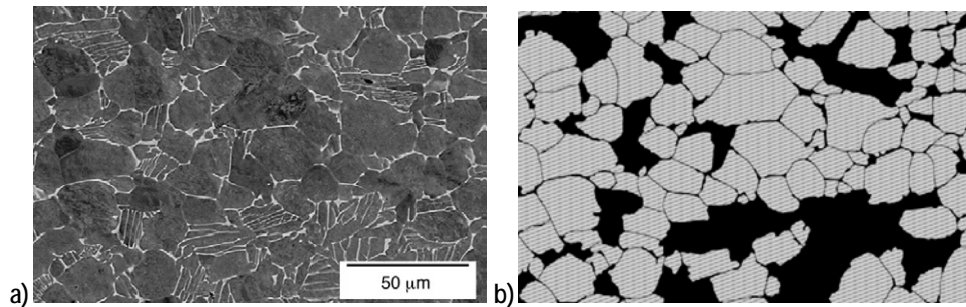


Fig.2.23. a) Original image [9] b) segmented equiaxed  $\alpha$  phase (grey) [13].

- **Volume fraction of equiaxed  $\alpha$  and total  $\alpha$**

Image process from SEM backscattered image (Fig.2.24):

- 1- After the pre-processing of the high resolution images is possible to use those images to perform an area fraction measurement to determine the volume fraction of the various phases.

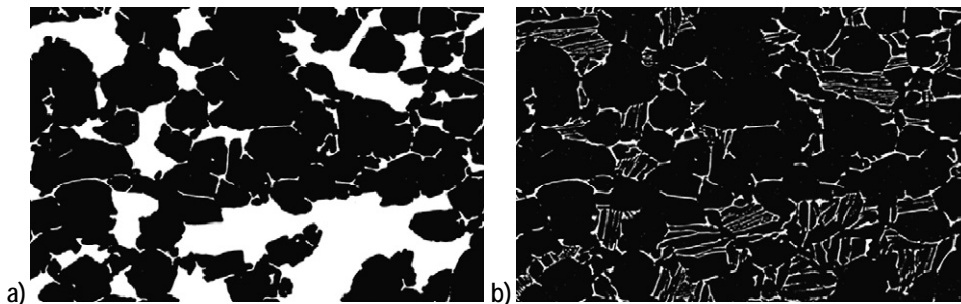


Fig.2.24. a) Volume fraction of equiaxed  $\alpha$  [9] and b) total volume fraction of  $\alpha$  (black) [13].

- **Thickness of Widmanstätten  $\alpha$ -laths in transformed  $\beta$**

Image process from SEM backscattered image (Fig.2.25):

- 1- The same interception method used to measure the size of equiaxed  $\alpha$  particles is used to measure the mean inverse intercept length of the  $\alpha$ -laths [13].



Fig.2.25. a) Isolation [9] and b) thickness measurement of Widmanstätten  $\alpha$ -laths [13].

- **$\beta$  Grain size**

Image process from optical image (2.26):

- 1- Low magnification images are used to ensure that an adequate number of grains is included in the analysis.
- 2- A mean intercept method carried out with ellipse plug-in from *Forvea* software, is used to measure the size of  $\beta$  grains. The method is difficult to implement in cases where the prior  $\beta$  grain boundaries are not covered by grain boundary  $\alpha$  [17].

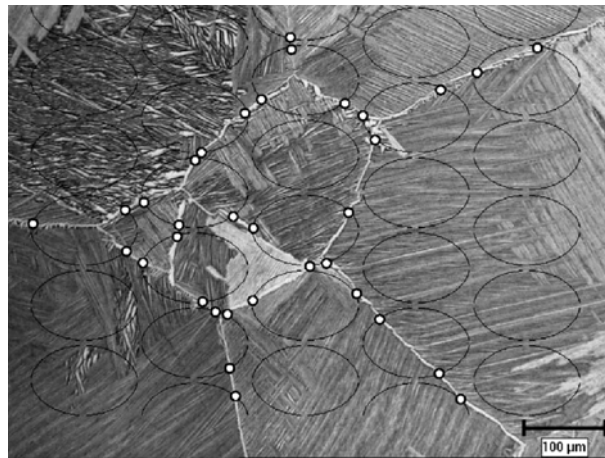


Fig.2.26. Prior  $\beta$  grain size measurement using a grid of cycloids [17].

These results of the 2D measurements depend on the statistics and quality of the measurements.

For this reason the following figures of merit should be considered [16]:

- Sample to sample variation
- Standard deviation for  $X$  micrographs
- Coefficient of variation in population
- Coefficient of variation

### 2.2.2. Differential scanning calorimetry (DSC)

Differential Scanning Calorimetry (DSC) means the measurement of the change of the difference in the heat flow rate to the sample with respect to a reference sample while they are subjected to a controlled temperature program. DSC measures the change of heat flow rate difference which normally is released or absorbed due to an alteration of the sample temperature. In case of thermal reactions/transitions in the samples during the test that controls the stepwise change from one temperature to another, the temperature of the samples undergoes an alteration and causes a DSC signal.

DSC is a technique suitable for investigating phase transformations and reactions which involve heat absorption and/or heat release. Such transitions usually correlate to endothermic or exothermic peaks in the DSC curve. The starting and ending temperatures of the transformation can be measured from the offset points of the peak. The latent heat of the transformation or reaction (or transformation enthalpy) can be determined by integrating the endothermic or exothermic peak area from the onset to offset temperatures (Fig.2.27) [18].

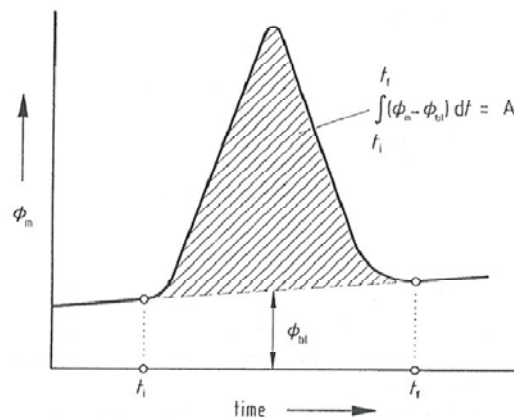


Fig.2.27. Integration from Onset to offset temperature of the peak considering a straight baseline [18].

Some DSC tests were carried out at a constant heating rate to understand the  $\alpha+\beta\rightarrow\beta$  transformation in Ti-6Al-4V. With an initial equiaxed  $\alpha$  phase mixed with transformed  $\beta$  phase (secondary  $\alpha$ ) microstructure, the results show that the  $\alpha+\beta\rightarrow\beta$  transformation includes two stages or endothermic peaks:  $\alpha$  in transformed  $\beta\rightarrow\beta$  and primary  $\alpha\rightarrow\beta$  [19].

The transformation upon heating starts from the transformed  $\beta$  phase. The retained  $\beta$  (secondary alpha) is metastable but contains less vanadium than equilibrium demands when formed during cooling. On re-heating above the temperature-range at which it formed it will become supersaturated in vanadium. The block  $\alpha$  phase is a stable phase with less  $\beta$ -stabilising vanadium and rich in  $\alpha$ -stabilising element aluminium. It can not transform if the temperature is not high enough. In most cases the  $\alpha+\beta\rightarrow\beta$  transformation in  $\alpha+\beta$  Ti alloys develops via the increase of  $\beta$  phase volume because the migration of  $\alpha/\beta$  interface [19].

### 2.2.3. Dilatometry

Dilatometry is a method by which the thermal expansion of a material may be measured. The volume alterations associated with the transformations at heating and cooling can be clearly seen as e.g. variations of the linear dimensions of specimens in dilatometric experiments. There are many types of dilatometers. Dilatometers may use a push-rod, capacitor, or optical system to sense expansion and may be configured in horizontal, vertical, or in-between configurations.

The push-rod dilatometer (Fig.2.28) can only be used for studies of length changes in solid materials. The sample rests between the tips of a fixed quartz rod and a similar frictionless sensing rod in the centre of a high-frequency induction furnace. Length changes are transmitted through the frictionless rod to an electronic transducer which in turn drives the recording system. The thermocouple is spot welded to the sample. Quenching gas enters to the chamber, passes through the hollow cylindrical sample and escapes through the openings. In a high-speed dilatometer, the specimen is positioned along the axis of a cylindrical heating coil, which is connected to a radio-frequency power generator. During operation, the magnetic field around the coil induces currents in the specimen, causing it to warm up. The induction coil itself is only mildly heated through resistive effects, but is in any case water cooled. Hence, the response of the system depends on the thermal characteristics of the specimen rather than those of the furnace. Fast quenching rates can therefore be achieved by directing high-pressure jets of gas through the centre of a hollow specimen; quench rates of up to 5000°C/s are reported to be obtained in favourable circumstances [20][21].

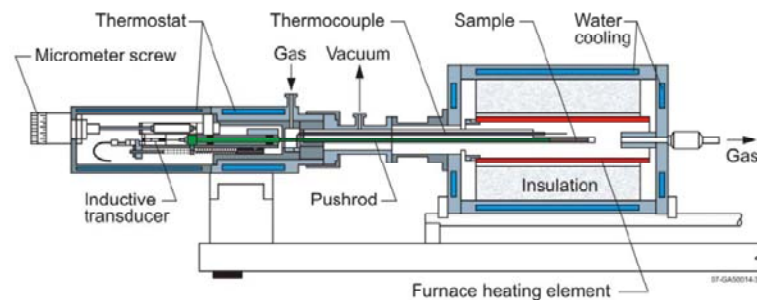


Fig.2.28. Scheme of a push-rod dilatometer in horizontal configuration [20].

Helium is used as the quenching gas in high cooling rate experiments because its thermal conductivity is about six times that of nitrogen. Large thermal gradients can be developed in the specimen during the quench, which may cause difficulties in the interpretation of the observed changes in specimen dimensions during cooling. The specimen can be enclosed in a vacuum, but it is more usual to use an inert atmosphere [21].

In titanium alloys the hexagonal type of  $\alpha$  phase crystal lattice is responsible for a considerable anisotropy of these dimensional variations. It has been calculated for pure Ti and experimentally confirmed that the changes of linear dimensions of the samples are not isotropic in character and each crystallographic orientation of the hexagonal  $\alpha$  phase shows distinctly different deformation both in terms of value and sign. The total linear effect is therefore a resultant of contributions of particular orientations in the final transformation product. Then, the results of the dilatometric tests may, depending on the conditions promoting growth in one or another direction, may lead to wrong conclusions. A much more reliable way to evaluate the volume

effect of transformations can be, therefore, the determination of changes of specific volumes of phases taking part in transformation with other techniques [22].

As the temperature increases the lattice parameters of  $\alpha$  phase grow in a linear manner and the change of the transformation kinetics have no impact upon their behaviour. The character of lattice parameters changes of  $\alpha$  is controlled mainly by the variations of thermal expansion coefficient. In the case of Ti-6Al-4V it should be also taken into account that the concentration of vanadium in the  $\alpha$  phase is low and the aluminium concentration remains practically constant in the whole range of transformation temperatures. On the other hand, the  $\beta$  phase lattice parameter shows more significant alterations due to the increase of the  $\beta$  phase content in the microstructure. The  $\beta$  lattice parameter grows mainly as a result of reducing of vanadium ( $\beta$ -stabilizer) content in this phase. It has been found that the maximal volume effect is associated with the transformation caused by heating at moderate rate of some 1 K/s, and its magnitude is fairly low (below 1%) [22]. The description of this effect should be clear:  $\alpha$  into  $\beta$  means volume shrinkage and the variation of vanadium content in the beta phase results in an expansion of the  $\beta$  phase (by increasing the content of vanadium in the beta phase, the lattice parameter decreases [23]).

#### 2.2.4. Hardness

The measurement of hardness is a simple but useful technique for characterizing mechanical properties and investigating phases in quenched-and-aged alloys. In the vickers method a weighted square pyramid, usually of diamond, is allowed to rest for a specific length of time on a polished surface of the specimen. Since the area of the impression is proportional to the load ( $L$ , kg), a load-independent hardness number can be formed from the quotient  $L/d^2$ . According to the Vickers prescription  $H_V=1,8544L/d^2$ . If its desired to investigate the individual grains of a fine polycrystalline sample, miniaturized versions (e.g. microhardness) of the tests are needed [24].

Macrohardness studies revealed the degrees of  $\alpha'$  decomposition depending on temperature and heating time. Fig.2.29 shows that at each temperature the curve of hardness vs. heating time has a sigmoidal type indicating that the precipitation of  $\alpha$  and  $\beta$  phases from  $\alpha'$  occurs by a nucleation and growth process controlled by diffusion. At low annealing temperatures ( $<600^\circ\text{C}$ ) the decomposition of  $\alpha'$  is incomplete as is shown by the low value of hardness. At temperatures above  $M_f$  ( $T\sim 800^\circ\text{C}$ ), the decomposition of  $\alpha'$  reaches completion, and the fact is observed in the high saturation value exhibited by the hardness (410HV). Thus, highest hardness values occur at total precipitation [2].

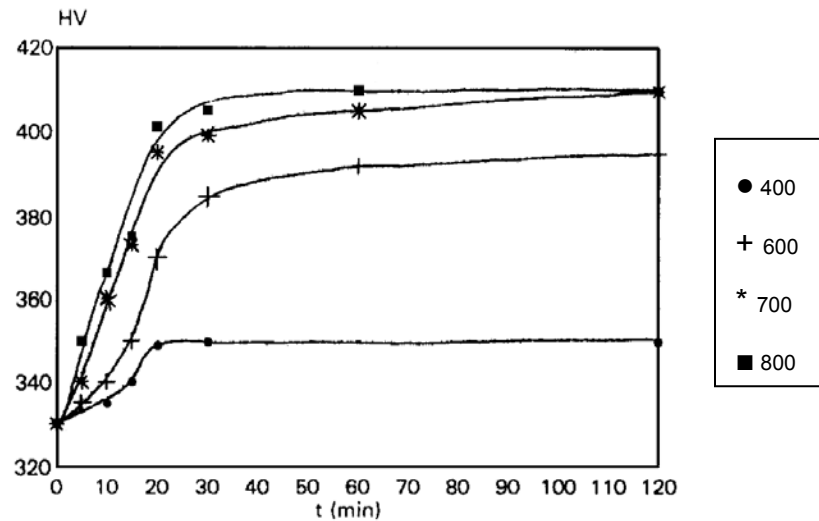


Fig.2.29. Plot of hardness evolution with annealing time for different temperatures [2].

Microhardness tests in Ti-6Al-4V revealed that the Vickers hardness decreases with increasing grain size and the thickness of laminar  $\alpha+\beta$  phase (Fig.2.29) [25].

The increasing value in microhardness occurs due to the precipitation of hcp  $\alpha$  phase during the decomposition. The  $\alpha$  phase is known to be harder than the hcp  $\alpha'$  and orthorhombic  $\alpha''$  martensite [26].

Lower values of the macrohardness have been observed in Ti-6Al-4V compared to its microhardness. This effect can be assigned to the physical presence of a population of processing-related artifacts and the hard  $\beta$  phase. However, compared to the commercially pure Ti the macrohardness is marginally higher than the microhardness resulting from the presence of a larger volume fraction of soft  $\alpha$  phase [27].

### 3. Experimental

---

#### 3.1. Material

A pre-forged Ti-6Al-4V alloy was used in this work with a chemical composition depicted in Table 3.1. The beta transus temperature is around 1000°C. The material was pre-forged in different steps in  $\alpha+\beta$  and  $\beta$  field followed by an annealing at 730°C during 1 hour and then air cooled.

Al	V	Fe	O <sub>2</sub>	C	N <sub>2</sub>	H <sub>2</sub>	Y
6,47	3,94	0,18	0,178	0,023	0,003	0,002	<0,001

Table 3.1. Chemical composition (%) of the Ti-6Al-4V samples.

Different heat treatment experiments have been carried out with deformed double cone samples (Fig.3.1). These samples are used to obtain a wide range of strains after deformation and to determine the microstructure evolution during deformation [28]. Samples were machined in order to be deformed with load axis perpendicular to the cogging direction as is illustrated in Fig.3.2 and deformed at different temperatures and strain rates. Table 3.2 shows the different deformation conditions in  $\alpha+\beta$  field of the studied samples.



Fig.3.1. Double cone sample before (left) and after deformation (right).

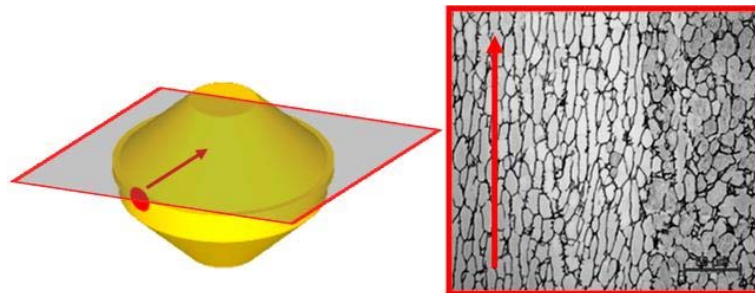


Fig.3.2. Prior  $\alpha$  grain orientation of the as-received microstructure in the double cone samples.

Deformation temperature (°C)	Strain rate (s <sup>-1</sup> )
930	0,1
	5
970	0,1
	5

Table 3.2. Temperature and overall strain rate conditions of the starting double cone samples.

Finite elements method simulations were carried out in previous works by Deform 2D software in order to determine the local parameters within the deformed samples and thus to correlate with the observed microstructure [28]. Fig 3.3 shows the local strain within the deformed double cone sample and the distribution along the major radius. Strain values between 0.2 and 1.1 were computed.

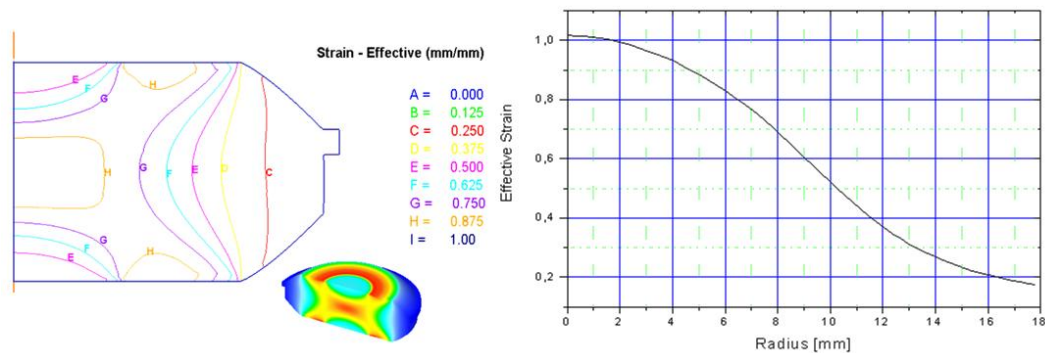


Fig.3.3. Effective strain distribution along the major radius of the deformed double cone samples.

### 3.2. Heat treatments

Heat treatments were carried out in order to observe the microstructure evolution depending on the deformation parameters. The eighth piece of each sample was used to carry out the heat treatment (HT1) in the *Linn High Therm HT1600* oven (3kw, 220V, 25A,  $T_{\max}=1550^{\circ}\text{C}$ ) in  $\alpha+\beta$  field at the temperatures of 930, 950 and  $970^{\circ}\text{C}$  during 30min and then cooled in oil on air (Fig.3.4). After metallographic analysis, an ageing at  $720^{\circ}\text{C}$  during 2 hours performed to 6 hours, followed by air cooling was carried out (Fig.3.4). All the experiments were in an Argon atmosphere to avoid the oxidation of the surface. Experiments with slow cooling at 20 K/min took place in the dilatometer *Bähr Thermoanalyse DIL 805* (Fig.3.5) in an inert atmosphere.

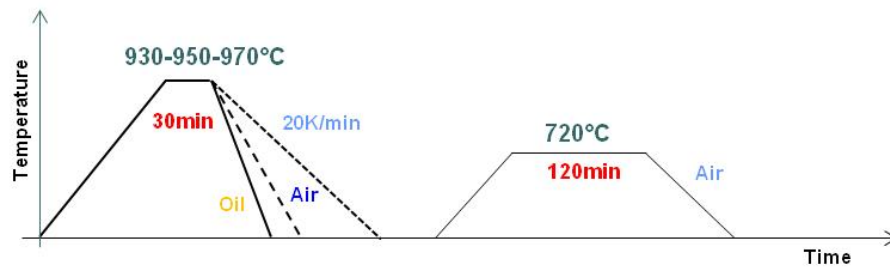


Fig.3.4. Heat treatments (HT1) and ageing carried out in the oven and dilatometer.

A cycle (HT2) with a combination of isothermal heat treatment in  $\alpha+\beta$  field with controlled cooling rates was carried out by means of *Bähr Thermoanalyse DIL 805* dilatometer.

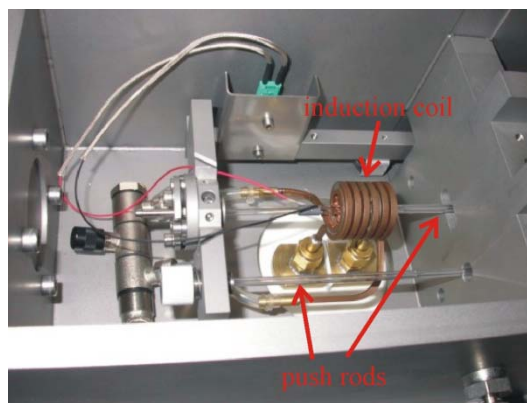


Fig.3.5. Photo of the *Bähr Thermoanalyse DIL 805* device.

Fig.3.6 shows the thermal cycle used, with heating rates of 300 K/min and 20 K/min to 925°C and 970°C holding in different tests during 4 hours. Afterwards the cooling was achieved by using three different stages of  $\sim 0.9$ , 6 and 300 K/min (Air) cooling rates with the intention to obtain a fully recrystallized material.

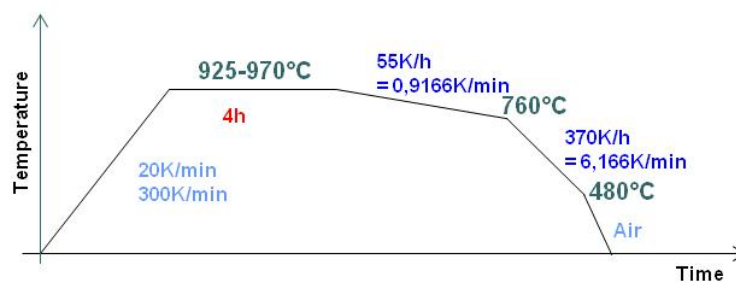


Fig.3.6. HT2 cycle carried out in the dilatometer.

These tests took place in a low pressure Argon atmosphere. In this case, the samples for these tests were cut from the quarters of the double cone samples of 4x4x10mm, with the maximum length parallel to the compression axis. From the dilatometry program, basically the data with length change, time and temperature were obtained for each experiment. Each test was carried out with a platinum sample as well in order to calibrate the measurements with Ti-6Al-4V

samples. Due to the non-homogeneous heating of the sample by the induction furnace, some tests with two thermocouples attached to the sample were carried out to control the gradient of temperature (Fig.3.7). Afterwards a gradient of approximately 50°C was revealed.

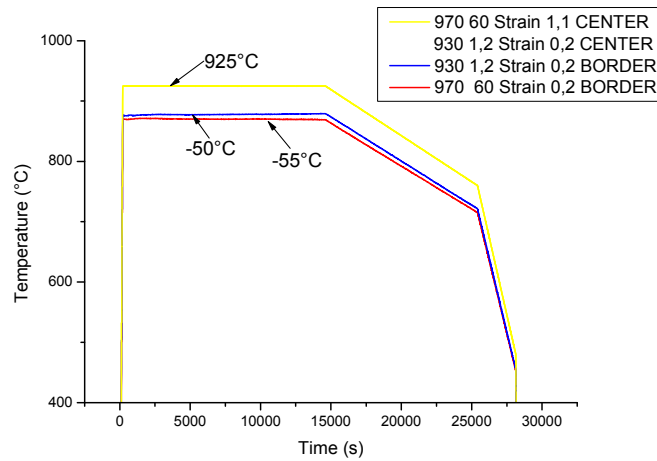


Fig.3.7. Tests carried out with two thermocouples to measure the gradient of temperature between the centre and the border of the sample.

The temperature ranges allowed in the *DIL 805* dilatometer with quartz rods is between 20°C-1100°C and 1500°C can be reached in the case of application of alumina rods. The maximum heating rate for the equipment is 4000K/s due to the inductive oven. The atmosphere can be controlled (vacuum or flow rate of gas). The maximum cooling rate reported is 2500K/s. More general information about the dilatometry methodology is explained in the 2.2.3 section.

### 3.3. Metallography

The double cone samples were cut by means of *Struers Accutom-5* machine using *Struers CBN 456 CA* disks for extremely hard non-ferrous metals (500-1400 HV). The pieces were then embedded in the *Struers Predopress* machine with *polyfast* resin which is used for examination in SEM due to its good electrical conductivity. Afterwards the polishing program for titanium alloys shown in Table 3.3 was carried out in the *Struers Tegraforce-5* machine for the embedded samples.

Step	Grinding/Polishing Cloth	Suspension	Lubricant	Time (min)
1	Si-C paper #320	-	Water	2
2	Si-C paper #500	-	Water	8
3	MD-Largo*	Diamond paste 9 $\mu$ m	Blau*	5
4	MD-Dur*	Diamond paste 3 $\mu$ m	Blau*	3
5	MD-Mol*	Diamond paste 1 $\mu$ m	Rot*	15
6	MD-Chem*	OP-S*	-	30

\*Commercial codes of Struers:  
MD-Largo: Composite disk that replaces several grinding steps of Si-C paper by one single step that prepares the specimen to be polished.  
MD-Dur: Cloth for fine grinding/polishing of ferrous/non-ferrous metals, coatings and plastics. Satin woven natural silk.  
MD-Mol: Cloth for fine polishing of ferrous/non-ferrous metals and plastics. Woven 100% wool.  
MD-Chem: Cloth for final polishing of all materials. Porous neoprene.  
OP-S: Colloidal silica suspension with a pH of 9.8 and a grain size of about 0.04  $\mu$ m. It is especially suited for polishing of very ductile metals.  
Blau: Cooling and lubricating liquid for fine grinding and diamond polishing.  
Rot: Lubricating liquid for final diamond polishing of softer materials. Water and oil based.

Table 3.3. Applied polishing method.

After polishing the samples were prepared for high resolution observation, either SEM or EBSD measurements. A *Philips XL30* SEM and a *FEI Quanta 200* FEG-SEM microscopes in BSE mode were used to observe the specimens with an accelerating voltage of 15kV and a spot of 5. EBSD measurements were carried out in the FEG-SEM equipment with the sample tilted 70°, applying an accelerating voltage of 20kV, a spot 6 at a working distance of 10 mm, with an increment step of 0.15-0.3  $\mu$ m.

Some samples were observed using a *Zeiss Axioplan* LOM microscope after etching with a Kroll reagent (150ml water, 3ml HF and 6ml HNO<sub>3</sub>) solution.

The image analysis for the quantification of microstructural features was carried out using the *Axiovision 4.7* program. SEM images were used at 500x magnification with a resolution of 1424 x 968 pixels. First, a maximization of the contrast in the SEM image between the alpha and the beta phase and a smoothing were needed to apply an intensity threshold mode to “paint” the stuck  $\alpha$  primary grains to be measured. After that, an improvement of the  $\alpha$  phase shape was completed by means of erase, drawing and cut tools. A worksheet about features of stuck  $\alpha$  grains like area, diameter, feret ratio or form circle is obtained. The secondary  $\alpha$  plates were also analysed in two different samples. Three different images from each strain condition were used to determine reliable results for each analyzed sample. Afterwards the obtained data from worksheets were plotted following the fitting of the log normal equation.

### 3.4. Differential scanning calorimetry

Analysis of continuous heating was carried out by DSC to determine the effect of final microstructure obtained after each heat treatment on the phase transformation. Thus, to identify the dissolution or precipitation of the different phases present in the material during the heating is the main goal. A *Netzch DSC 404C Pegasus* device (Fig.3.8) was used with a work temperature range from 120°C to 1650°C and vacuum / gas atmosphere up to 50K/min of heating/cooling rate.



Fig.3.8. Netzch DSC 404C Pegasus device.

The DSC tests were carried out using two reference samples: Alumina ( $\text{Al}_2\text{O}_3$ ) and CP Ti grade II. The CP Ti grade II sample had to be prepared in function of the mass of the standard  $\text{Al}_2\text{O}_3$  reference sample ( $m_R$ ), following the equation 3.1. Basically, equation 3.1 considers that in case of no reaction in the samples during the test there is no heat flow difference ( ) between the reference and the studied samples. Then the mass of the studied ( $m_S$ ) sample can be obtained in function of heat capacity values of reference ( $C_R$ ) and studied sample ( $C_S$ ), and the mass of reference sample ( $m_S$ ).

$$\Delta\phi_{SR} = \phi_S - \phi_R = 0$$

$$C_S \frac{dT_S}{dt} = C_R \frac{dT_R}{dt}$$

$$C_S \cdot m_S = C_R \cdot m_R \rightarrow m_S$$

Equation 3.1. Flow difference relationship to know the mass of the studied sample.

The calculation established that the dimensions of CP Ti grade II samples had to be disks of  $\phi=5,5\text{mm}$  and  $h=1,5\text{mm}$ . The DSC Ti-6Al-4V samples were cut from strain 1 zone of the eighth pieces or dilatometer samples into disks of  $\phi=5,5\text{mm}$  and  $h=1,1\text{mm}$  either for  $\text{Al}_2\text{O}_3$  as a reference sample or for CP Ti grade II as a reference sample. The reference and studied samples

are placed in  $\text{Al}_2\text{O}_3$  cylindrical crucibles and the heating cycle applied (Fig.3.9) was carried out in an Argon atmosphere. In addition, several experiments with empty pan as reference with  $\text{Al}_2\text{O}_3$  and CP Ti grade II samples, and CP Ti grade II as reference and as a sample, were carried out to evaluate the effect of external factors like oxidation in the tests. The results were processed and analyzed by the *Proteus Analysis* program, obtaining the heat flux vs temperature curve for each experiment. In the measurements of energy values at peak the criterion of flat baseline in zero was used.

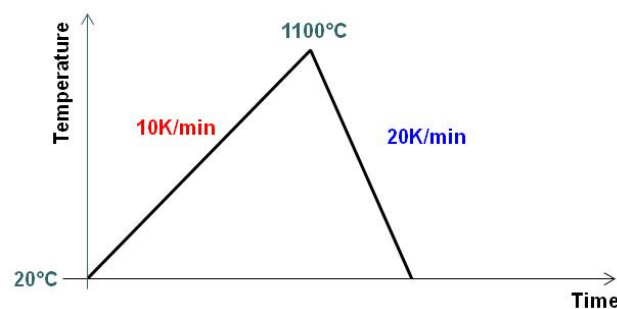


Fig.3.9. Continuous heating in the DSC device up to 1100°C.

The DSC tests were carried out with Ti grade II and  $\text{Al}_2\text{O}_3$  as reference samples with the intention to get more reliable results in the tests with  $\text{Al}_2\text{O}_3$ , because there is no reaction of the sample during the continuous heating, and to have better information of the peaks with the Ti grade II samples due to its close heat capacity to the Ti-6Al-4V samples. In general, the tendencies of the Ti grade II curves were quite different than the ones using  $\text{Al}_2\text{O}_3$  as reference (Fig.3.10b) due to its reactivity, and just few of them showed a similar tendency of peaks (Fig.3.10a).

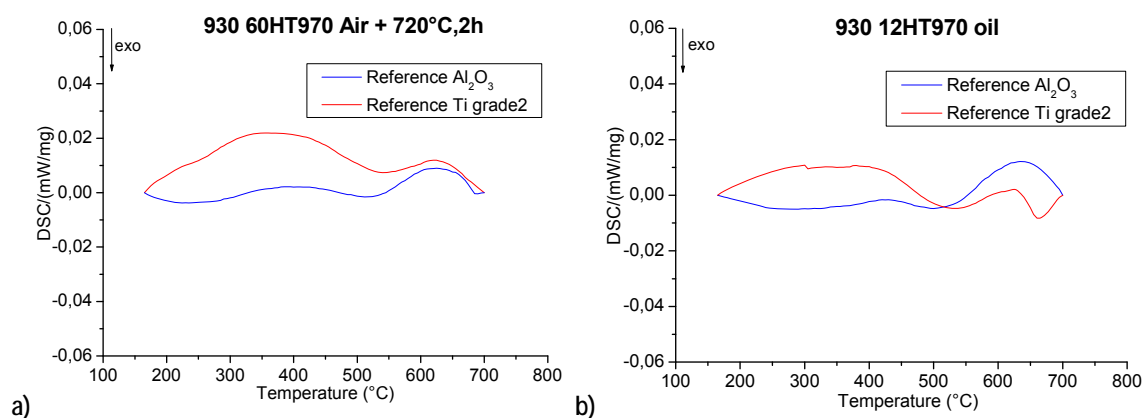


Fig.3.10. a) Similar and b) different tendencies of Ti grade II curves compared to  $\text{Al}_2\text{O}_3$  curves.

Fig.3.11a presents the tests carried out with both reference samples, against an empty pan as reference. The curve with Ti grade II should be almost flat until the precipitation peak of  $\alpha$  in the temperature of 882°C approximately, and that's not what the curve shows. The test with

both Ti grade II, test sample and reference sample (Fig.3.11b), should result in a totally flat curve. These measurements show that during the tests some oxidation or reaction with the  $\text{Al}_2\text{O}_3$  pan of the Ti grade II results in a non reliable heat flow curve, for this reason just the data obtained with  $\text{Al}_2\text{O}_3$  samples can be considered in the results.

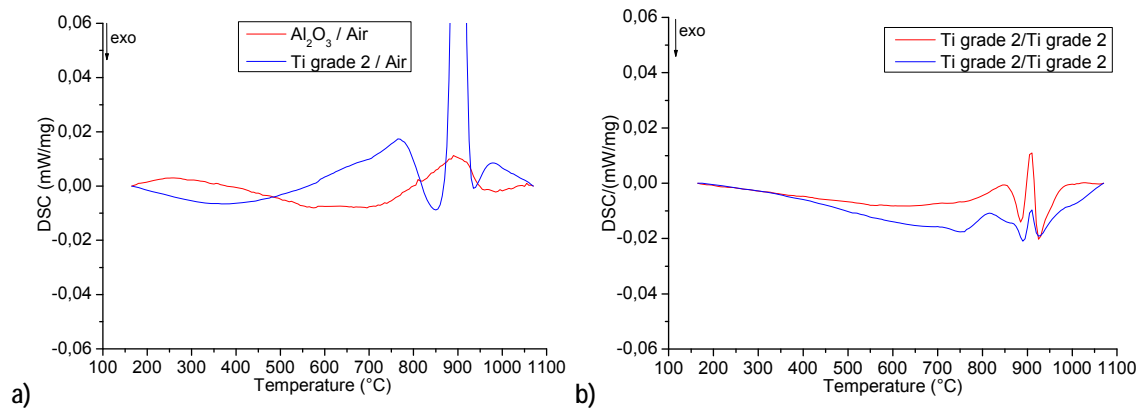


Fig.3.11. DSC measurements carried out to check the behaviour of reference samples in the continuous heating cycle applied in the Ti-6Al-4V samples. a) Tests with  $\text{Al}_2\text{O}_3$  and Ti grade II with an empty crucible as a reference (Air) b) Two tests with Ti grade II as a sample and as reference.

### 3.5. Hardness

Some samples were polished and submitted to macrohardness and microhardness tests after the heat treatments. Several macrohardness measurements were carried out to samples submitted to only HT1, ageing and HT2 cycles. On the contrary, the microhardness tests were just applied to aged samples. An *Emco Test MIC* machine was used for the macrohardness tests. At least six Vickers indentations were carried out respectively over the strain ranges 0.2 and 1.1 zones of the heat treated samples with 1Kg of force during 10s of dwell time. The diagonals of each indentation were measured with the *Emco test* software to get the HV value.

As well as in macrohardness tests, six microhardness Vickers indentations were carried out respectively in  $\alpha$  primary phase and in transformed  $\alpha'$  martensite phase of aged samples for the strain ranges of 0.2 and 1.1. The *MHT-4* microhardness tester (control unit) and a Vickers indenter (sensor with a diamond tip) combined directly with a *Zeiss Axioscop LOM* microscope with a digital camera were used to make the microindentations in the different phases of the heat treated samples. The indenter is controlled by the tester and is simply inserted into the nose-piece of the microscope instead of an objective (Fig.3.12). The camera displayed the image of the microstructure in a screen with enough resolution to locate the phases and make the indentation, but not enough to measure the diagonals. For this reason once the microindentations were carried out, were measured afterwards in the *Zeiss Axioplan LOM* microscope with its analysing program. The used parameters were: Force of 0,1N, 10s of dwell time, slope of 0,5N/s and 100x magnification to measure the indentations.



Fig.3.12. Vickers indenter used for the microhardness measurements.

## 4. Results

---

### 4.1. Metallography

#### 4.1.1. Microstructure of the starting samples

The as-received Ti-6Al-4V alloy presents a bimodal  $\alpha+\beta$  equiaxed microstructure due to the processing explained in section 3.1. Fig.4.1a shows the microstructure in the transverse section of the billet with a homogenous distribution of primary  $\alpha$ . On the other hand, Fig.4.1b shows the microstructure of the material in the longitudinal direction with a non homogeneous shape distribution of primary  $\alpha$ , with some grains elongated in the cogging direction of the billet.

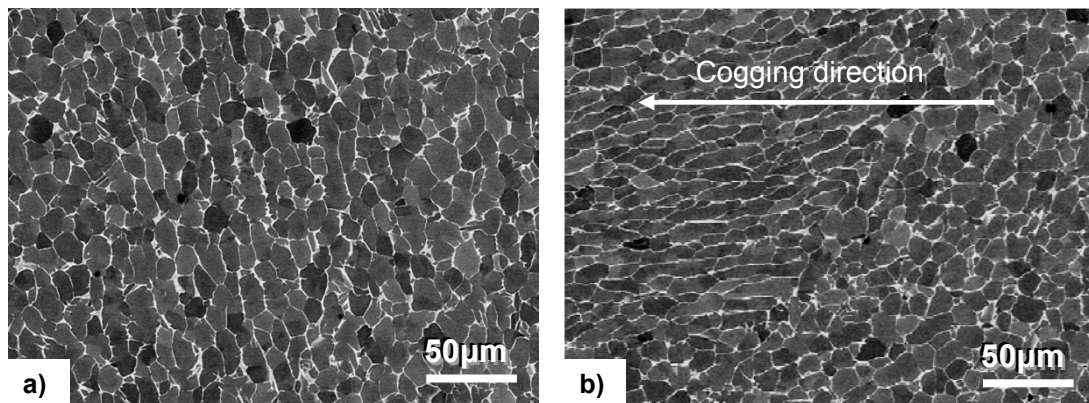


Fig.4.1. FEG-SEM images of as-received Ti-6Al-4V with small secondary  $\alpha$  particles between (equiaxed)  $\alpha$  primary grains a) transverse direction and b) longitudinal (prior grain orientation) direction in the billet..

After the deformation processes commented in section 3.1, the double cones have a clear bimodal morphology. After each deformation condition, the samples were water quenched, resulting in an  $\alpha+\beta$  structure of deformed  $\alpha$  grains surrounded by a precipitated  $\alpha'$  martensite in the  $\beta$  grains. An influence of the temperature and the local deformation can be observed in Fig 4.2 to 4.5. In Fig.4.2 and 4.3 the effect of deformation on the shape of  $\alpha$  primary grains is observed with an elongation of the  $\alpha$  grains when increasing the strain perpendicular to the deformation direction. The strain rate effects also the morphology of the alpha grains. At higher temperature of deformation,  $\alpha$  primary grains in Fig.4.4 and Fig.4.5 show a minimum effect of the strain on the shape. However, between Fig.4.4 and 4.5 there is no apparent effect of the deformation rate in  $\alpha$  primary morphology.

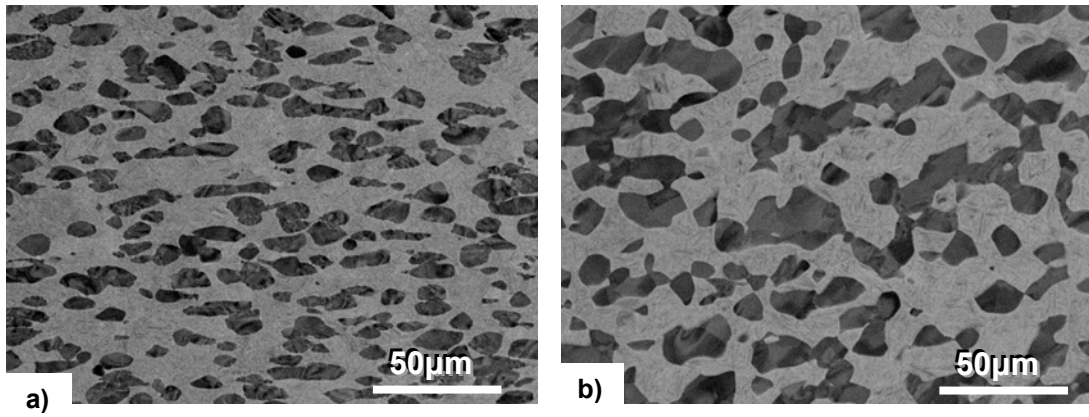


Fig.4.2. SEM images of Ti-6Al-4V double cones deformed at 930°C and 0.1s<sup>-1</sup> for a) 1.1 strain and b) 0.2 strain. Compression axis is vertical.

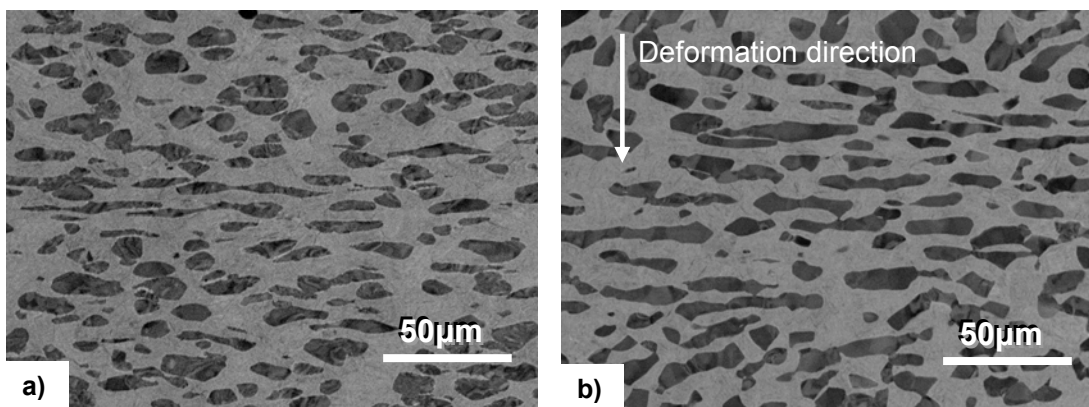


Fig.4.3. SEM images of Ti-6Al-4V double cones deformed at 930°C and 5s<sup>-1</sup> for a) 1.1 strain and b) 0.2 strain.

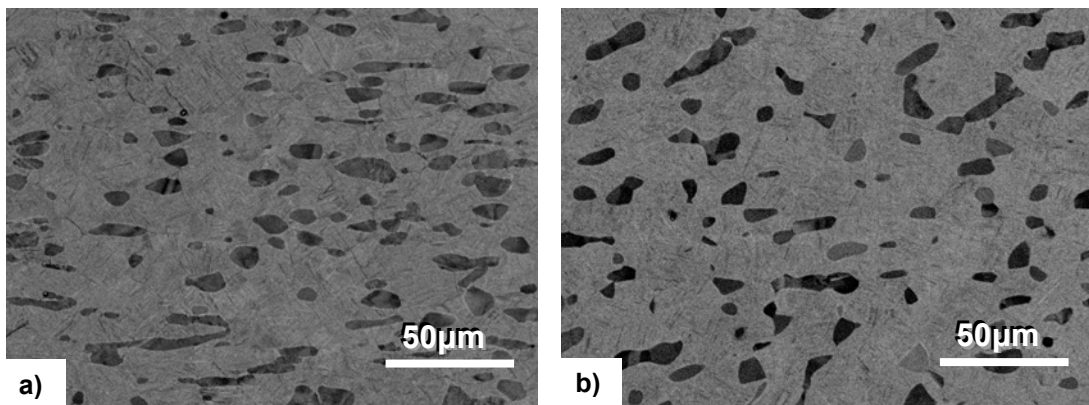


Fig.4.4. SEM images of Ti-6Al-4V double cones deformed at 970°C and 0.1s<sup>-1</sup> for a) 1.1 strain and b) 0.2 strain. Compression axis is vertical.

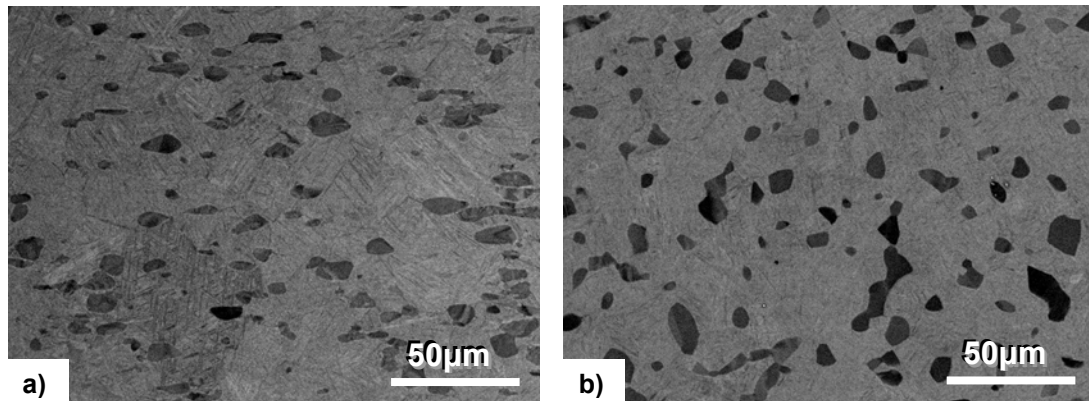


Fig.4.5. SEM images of Ti-6Al-4V double cones deformed at 970°C and 5s<sup>-1</sup> for a) 1.1 strain and b) 0.2 strain. Compression axis is vertical.

#### 4.1.2. Microstructure after heat treatments

##### 4.1.2.1. HT1

The Fig.4.6, Fig.4.7 and Fig.4.8 show the microstructures obtained from deformed samples at 930°C followed by HT1 (930 or 970°C followed by water, oil quenching and slowly cooling). The amount of  $\alpha$  was decreases with increasing the temperature. The microstructures of oil cooled samples (Fig.4.6) consist of  $\alpha$  primary grains surrounded by  $\alpha'$  martensite in the  $\beta$  grains as in the deformed samples (Fig.4.3). On the other side, the samples cooled in air Figures 4.7 and 4.8 present  $\alpha$  primary grains surrounded by  $\alpha$  secondary laths embedded in a  $\beta$  matrix. A layer of  $\alpha$  constituent along  $\beta$  grain boundaries can be seen in these samples (Fig.4.7).

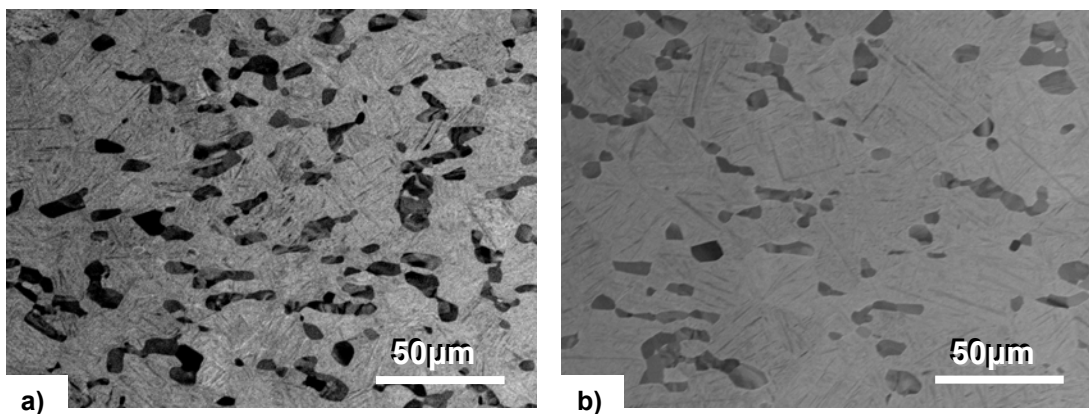


Fig.4.6. SEM images of Ti-6Al-4V double cone samples deformed at 930°C, 5s<sup>-1</sup>, 1.1 strain, and heat treated a) 950°C, 30min, Oil cooled b) 970°C, 30min, Oil cooled. Compression axis is vertical.

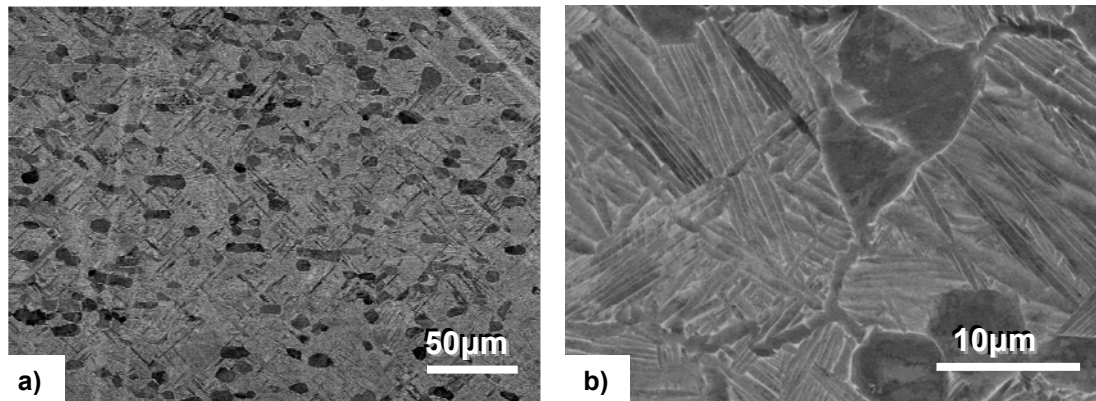


Fig.4.7. FEG-SEM images of the Ti-6Al-4V double cone sample deformed at 930°C, 5s<sup>-1</sup>, 1.1 strain, and heat treated at 970°C, 30min, Air cooled. a) general view b) detail showing primary globular  $\alpha$  and secondary  $\alpha$  growing also at the prior beta grain boundary. Compression axis is vertical.

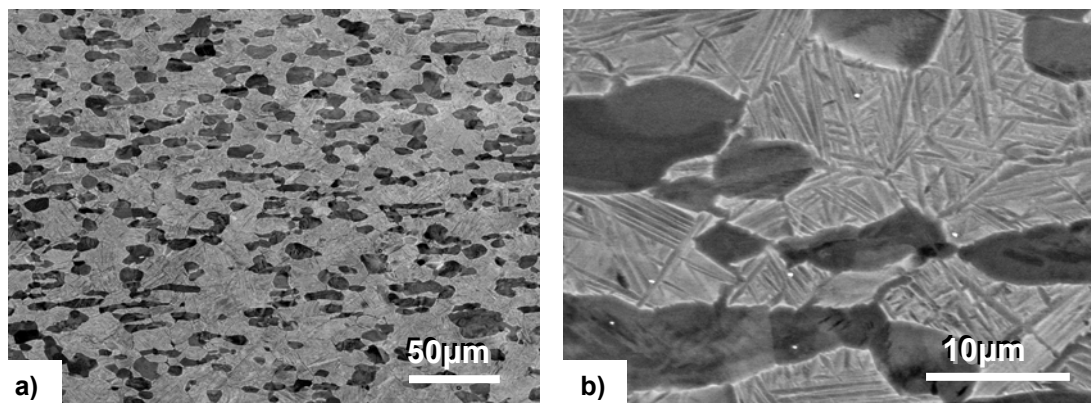


Fig.4.8. FEG-SEM images of the Ti-6Al-4V double cone sample deformed at 930°C, 5s<sup>-1</sup>, 1.1 strain, and heat treated at 930°C, 30min, Air cooled. a) general view b) detail of primary and secondary alpha. Compression axis is vertical.

Fig.4.9, Fig.4.10 and Fig.4.11 correspond to samples deformed at 970°C followed by HT1. In this case, when the deformation temperature and the temperature of the heat treatment are equal (Fig.4.9), the same kind of microstructures as in Fig.4.6b, Fig.4.7 are obtained for oil and air cooling. On the other hand when the temperature of the heat treatment is lower than that of the deformation temperature (Fig.4.10 and Fig.4.11),  $\alpha$  secondary large plates appear in the microstructure. For air cooling condition (Fig.4.10) the microstructure shows a homogeneous distribution of  $\alpha$  primary grains and  $\alpha$  secondary plates surrounded by  $\alpha$  secondary laths embedded in the  $\beta$  matrix. It was observed that  $\alpha$  primary grains are surrounded by  $\alpha'$  martensite. A less  $\alpha$  secondary plates are found in the oil cooling condition (Fig.4.11). In addition, is it possible to distinguish some  $\beta$  grains in the microstructure of Fig.4.11b.

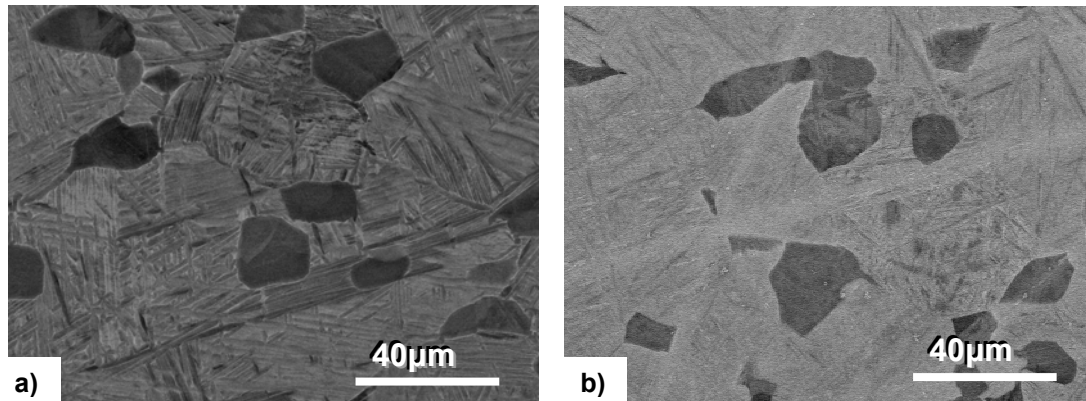


Fig.4.9. FEG-SEM images of Ti-6Al-4V double cone samples deformed at 970°C, 5s<sup>-1</sup>, 1.1 strain, and heat treated at a) 970°C, 30min, Air cooled b) Oil cooled. Compression axis is vertical.

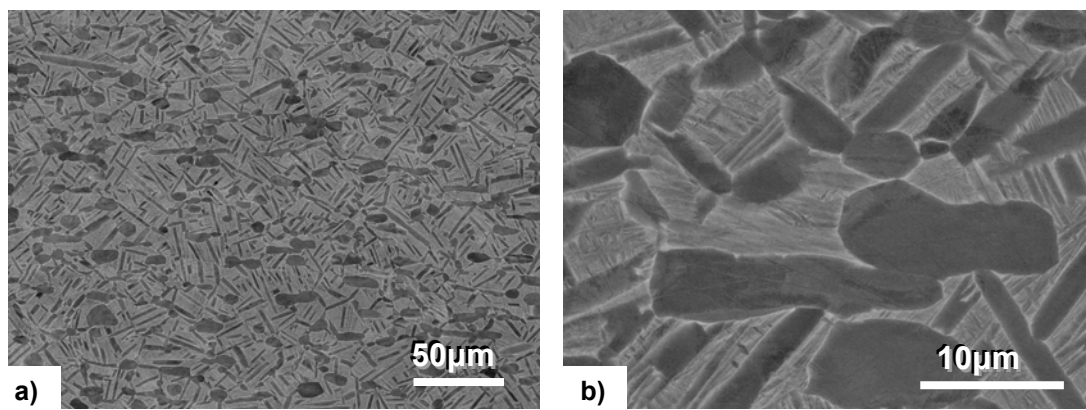


Fig.4.10. FEG-SEM images of the Ti-6Al-4V double cone sample deformed at 970°C, 5s<sup>-1</sup>, 1.1 strain, and heat treated at 930°C, 30min, Air cooled. a) general view b) detail. Compression axis is vertical.

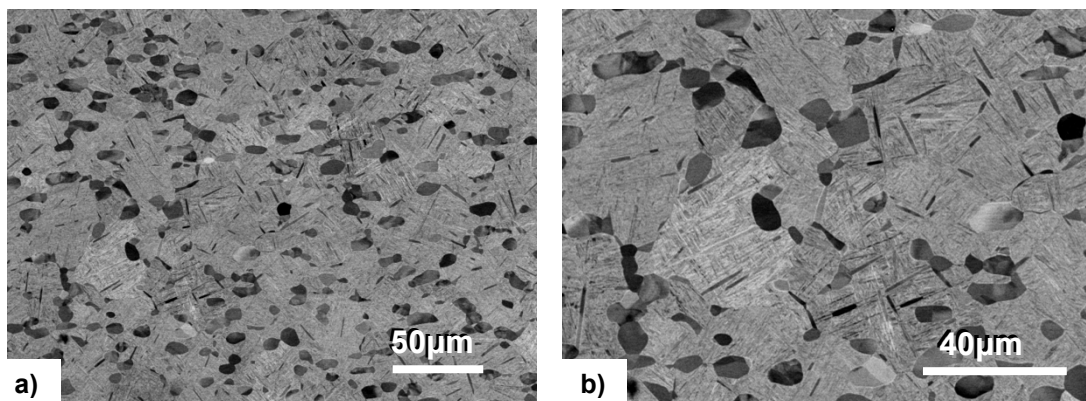


Fig.4.11. FEG-SEM images of the Ti-6Al-4V double cone sample deformed at 970°C, 5s<sup>-1</sup>, 1.1 strain, and heat treated at 950°C, 30min, Oil cooled. a) general view b) detail. Compression axis is vertical.

The comparison of the Fig.4.6b with the Fig.4.12a shows that there is no apparent difference in the primary  $\alpha$  morphology for the samples deformed by the same parameters in a different strain range. Despite the heat treatment some  $\alpha$  primary grains still show a deformed morphology (Fig.4.12a). The same effect happens for two samples with different strain rates (Fig.4.6b and Fig.4.12b). The higher the strain rate the (Fig.4.6b) larger and more oriented are the primary  $\alpha$  grains (Fig.4.12).

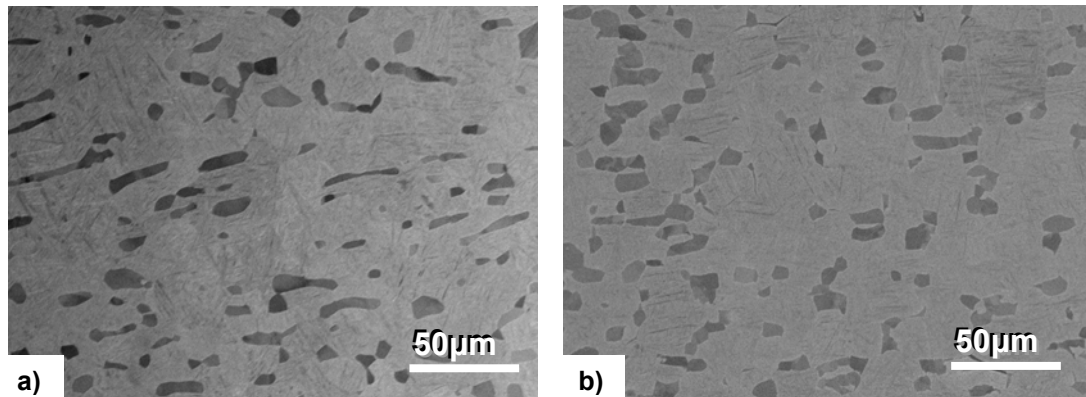


Fig.4.12. SEM images of Ti-6Al-4V double cone samples heat treated at 970°C, 30 min and oil quenched, deformed at a) 930°C, 5s<sup>-1</sup>, 0.2 strain b) 930°C, 0.1s<sup>-1</sup>, 1.1 strain. Compression axis is vertical.

#### 4.1.2.2. Ageing

The next pictures show the effect on the microstructure of the ageing heat treatments carried out after HT1. Fig.4.13, Fig.4.14 and Fig.4.15 show the effect of the ageing on samples oil cooled from HT1. It can be seen that the  $\alpha'$  martensite transformed into  $\alpha$  needles or laths of different sizes embedded in a matrix of  $\beta$  in different orientations. It was also observed that among the big needles grown at the  $\alpha$  primary grains or  $\beta$  grain boundaries, there are different colonies of smaller needles which grown perpendicular from these big needles. In the samples of figures 4.13 and 4.14 the ageing heat treatment was applied during two hours and in each case the way in which the needles grew is the same independent of the temperature, strain rate or strain range history, just depending on the cooling rate (air or oil). The needles observed in Fig.4.15 are bigger than those observed in Fig.4.13 and Fig.4.14 as a consequence of the longer ageing heat treatment of six hours.

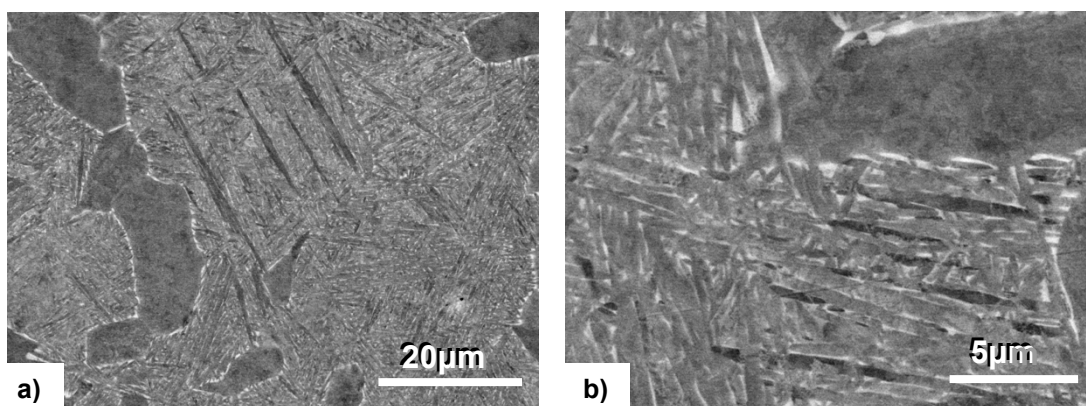


Fig.4.13. FEG-SEM images of the Ti-6Al-4V double cone sample deformed at 930°C, 0.1s<sup>-1</sup>, 1.1 strain, heat treated at 970°C, 30min, Oil cooled, plus ageing at 720°C, 2h a) general view b) detail. Compression axis is vertical.

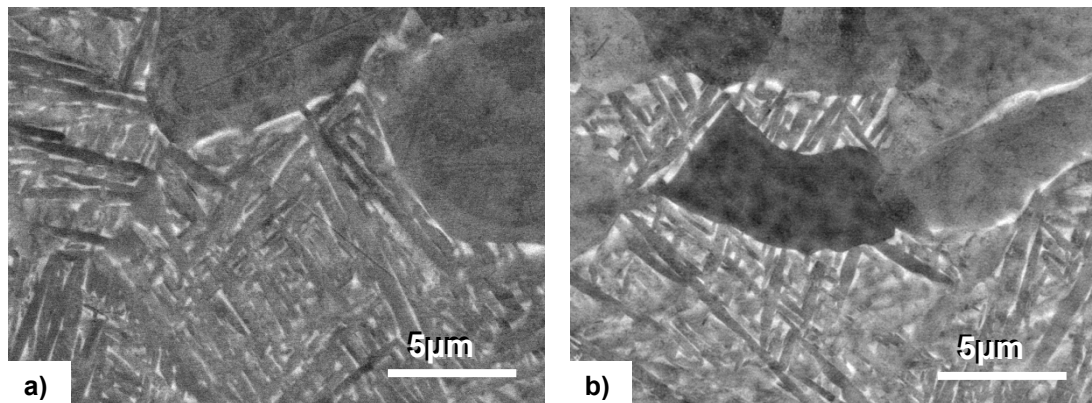


Fig.4.14. FEG-SEM images of Ti-6Al-4V double cone samples deformed at a) 930°C, 5s<sup>-1</sup>, 1.1 strain and heat treated at 970°C, 30min, Oil cooled, plus ageing at 720°C, 2h b) 970°C, 0.1s<sup>-1</sup>, 1.1 strain and heat treated at 950°C, 30min, Oil cooled, plus ageing at 720°C, 2h. Compression axis is vertical.

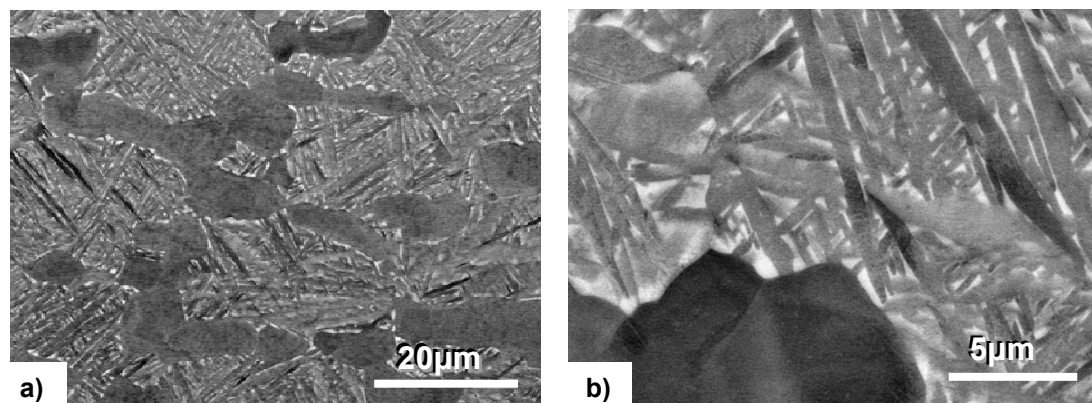


Fig.4.15. FEG-SEM images of the Ti-6Al-4V double cone sample deformed at 930°C, 5s<sup>-1</sup>, 1.1 strain, heat treated at 970°C, 30min, Oil cooled, plus ageing at 720°C, 6h a) general view b) detail. Compression axis is vertical.

The ageing heat treatments carried out with air cooled samples from HT1 (Fig.4.16) show a different morphology compared to the aged samples that came from a  $\alpha'$  martensite structure (oil cooled). In Fig.4.16a can also be seen that in these samples the  $\beta$  grain boundaries are clearly revealed by a wide  $\alpha$  layer.

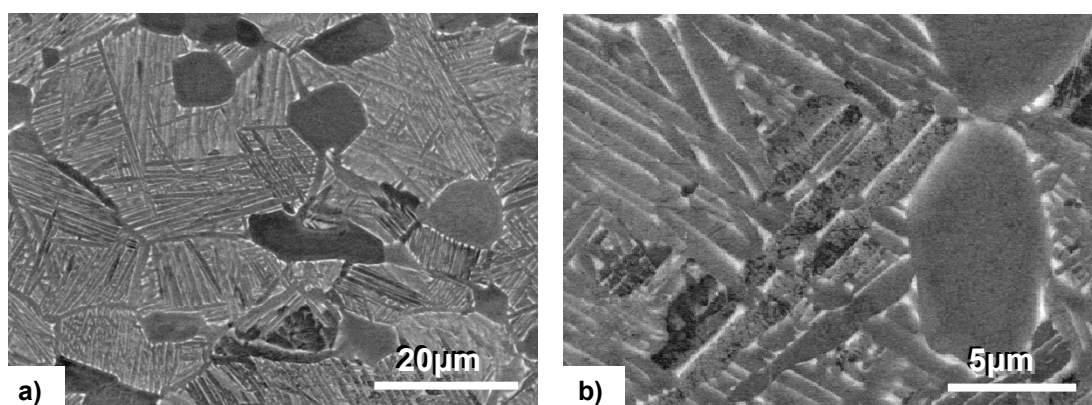


Fig.4.16. FEG-SEM images of the Ti-6Al-4V double cone sample deformed at 930°C, 5s<sup>-1</sup>, 1.1 strain, heat treated at 970°C, 30min, Air cooled, plus ageing at 720°C, 2h a) general view b) detail. Compression axis is vertical.

The microstructure in Fig.4.17 corresponds to the slowest cooling condition of 20K/min from HT1 followed by ageing. The obtained microstructure is completely different compared with the

others seen in anterior images. Fig.4.17b shows large alpha lamellae, primary alpha and some tiny alpha laths in between.

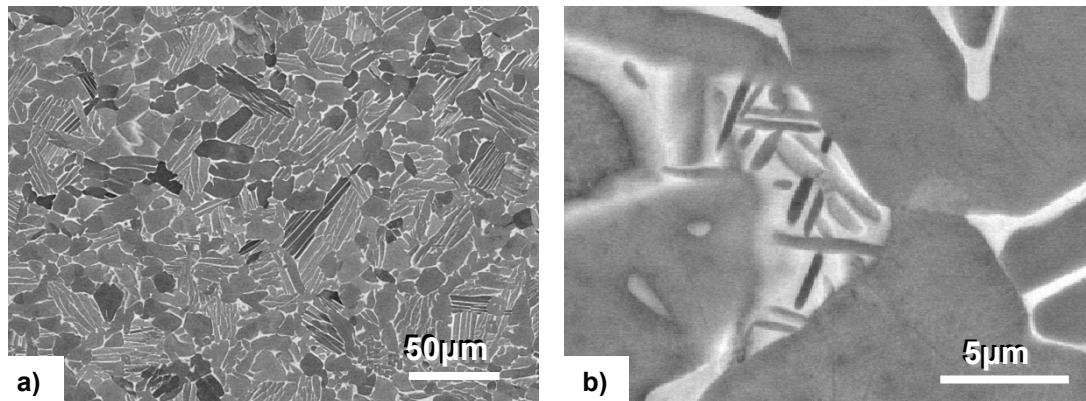


Fig.4.17. FEG-SEM images of the Ti-6Al-4V double cone sample deformed at 930°C, 5s<sup>-1</sup>, 1.1 strain, heat treated at 970°C, 30min, 20K/min cooled, plus ageing at 720°C, 2h, Air cooled a) general view b) detail. Compression axis is vertical.

#### 4.1.2.3. HT2

The Fig.4.18, Fig.4.19, Fig.4.20, Fig.4.21 and Fig.4.22 show the microstructures after the HT2. Fig.4.18 shows a globularized  $\alpha$  microstructure of samples deformed at 930°C followed by recrystallization treatment. Fig.4.18b reveals that there are tiny  $\alpha$  needles among  $\alpha$  primary grains for higher heat treatment temperatures higher than deformation temperature (Fig.4.19a). A globularized  $\alpha$  structure is also observed, but in this case the grains are larger than those observed in Fig.4.18. The recrystallization cycles applied to samples deformed at 970°C are shown in Fig.4.19b and Fig.4.20. Once again, the morphology of the  $\alpha$  grains depends on the heat treatment temperature. For the recrystallization cycle until 925°C (Fig.4.20a), big  $\alpha$  plates have grown homogeneously among the  $\alpha$  primary grains. In the sample treated at 900°C (Fig.4.20b) smaller secondary  $\alpha$  plates appears distributed in colonies. Finally, when the deformation temperature of 970°C coincides with the heat treatment temperature (Fig.4.19b), the secondary  $\alpha$  plates are even bigger than the  $\alpha$  primary elements and the microstructure is coarser than the others heat treated at 925°C (Fig.4.20) after deformation at the same temperature.

The effect of the anterior deformation to the recrystallization cycle can be appreciated in Fig.4.21. As was commented before, the temperature in the border of the sample for dilatometry (Fig.4.21b) is lower than in the centre (Fig.4.21a). For this reason and because of the lower strain condition (Fig.4.21b) a thinner prior  $\beta$  shape appears.

During the heat treatments in the dilatometer, a formation of oxide (Fig.4.22) affected the surface of the samples forming  $\alpha$  casing approximately in the first 80 $\mu$ m. It was due to the contamination of the chamber with oxygen and the use of a poor protective Ar atmosphere.

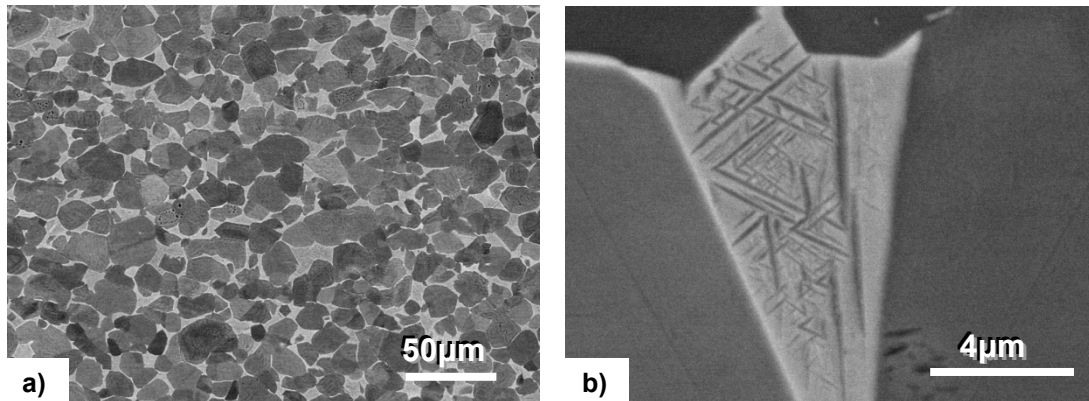


Fig.4.18. FEG-SEM images of the Ti-6Al-4V double cone sample deformed at 930°C, 5s<sup>-1</sup>, 1.1 strain, heat treated up to 925°C in HT2 a) globularized alpha grains b) small alpha needles embedded in the beta field. Compression axis is vertical.

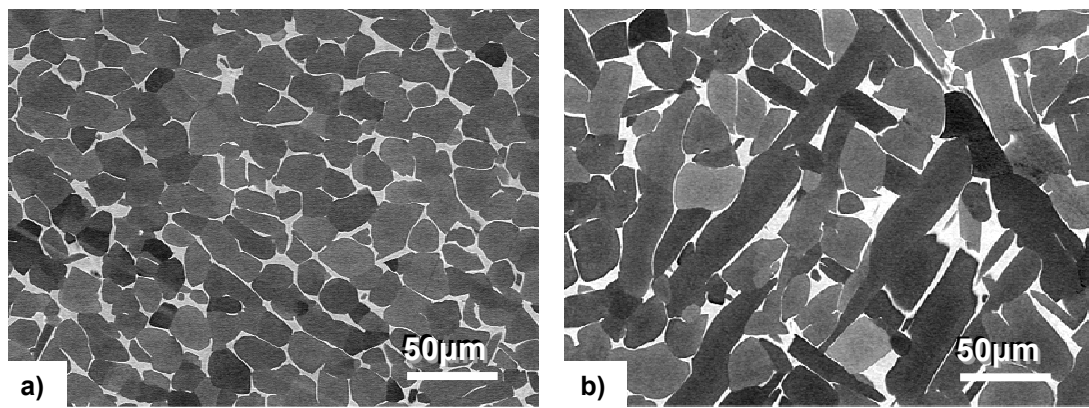


Fig.4.19. FEG-SEM images of Ti-6Al-4V double cone samples heat treated at 970°C in HT2 after deformation a) 930°C, 5s<sup>-1</sup>, 0.8 strain b) 970°C, 1s<sup>-1</sup>, 0.8 strain.

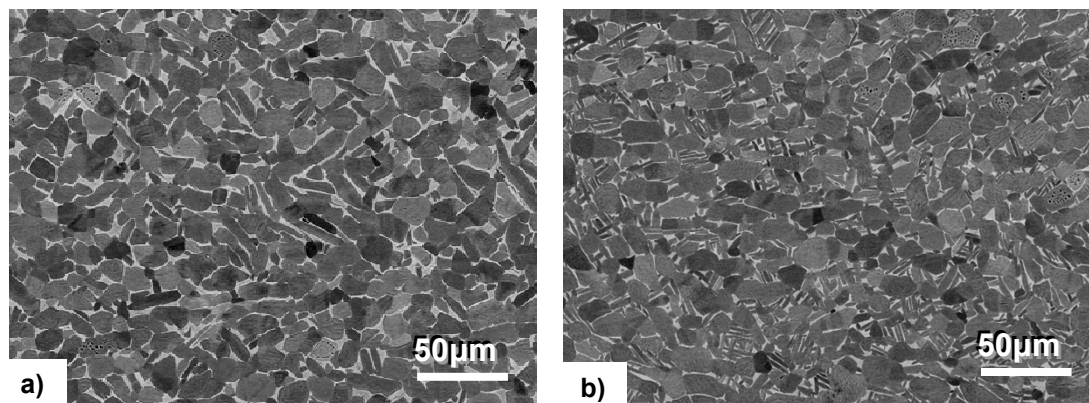


Fig.4.20. FEG-SEM images of Ti-6Al-4V double cone samples deformed at 970°C, 5s<sup>-1</sup>, a) 1.1 strain heat treated at 925°C in HT2 b) 0.6 strain and heat treated at 900°C in HT2. Compression axis is vertical.

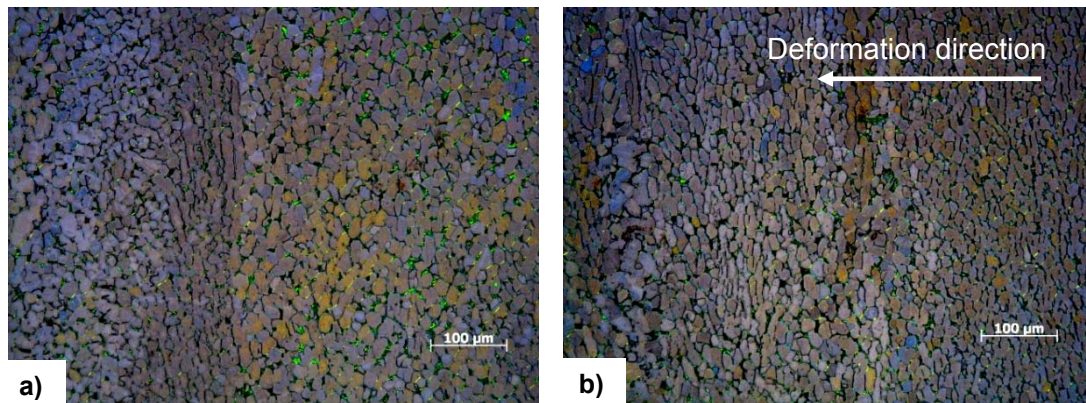


Fig.4.21. LOM images using polarized light of Ti-6Al-4V double cone samples deformed at 930°C, 5s<sup>-1</sup>, a) 1.1 strain in the centre b) 0.5 strain at the border and heat treated at 925°C in HT2. Compression axis is horizontal.

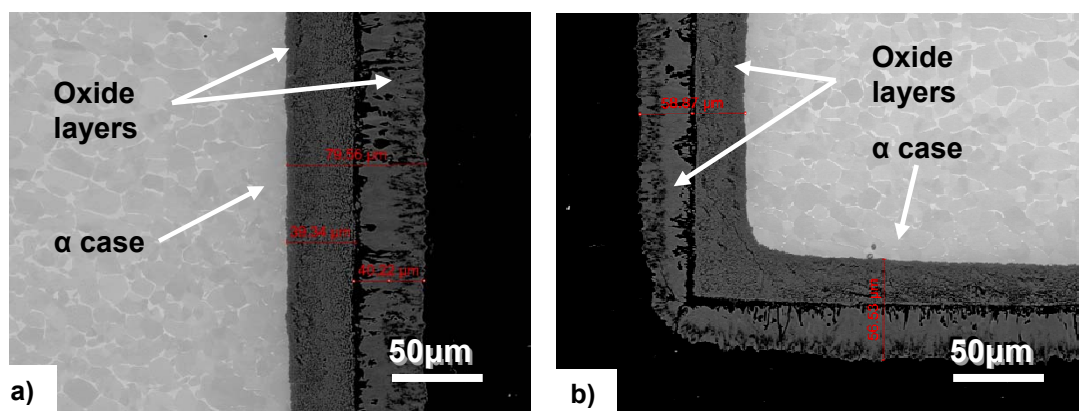


Fig.4.22. Oxide layers in dilatometry samples after the tests.

The EBSD measurements were carried out after HT1 (Fig.4.23) and after HT2. Fig.4.24, Fig.4.25 and Fig.4.26 show the orientation maps where the different crystallographic orientations of the alpha and beta phases are distinguished. Fig.4.23 shows the  $\alpha$  grains of the deformed sample at 970°C and subsequent heat treated at 930°C and finally air cooled. It is possible to distinguish the  $\alpha$  primary grains from the secondary plates and the  $\alpha$  secondary small laths. Orientation maps in Fig.4.24a and Fig.4.25a show a completely recrystallized microstructure with globularized  $\alpha$  in differentiated orientation. In Fig.4.24b and Fig.4.25b the crystallographic orientation of the  $\beta$  phase is also shown. Deformation at 970°C and HT2 at 925°C results in similar features than before, as can be seen in Fig.4.26 with big secondary  $\alpha$  plates and larger  $\beta$  grains denoted by the crystallographic orientation.

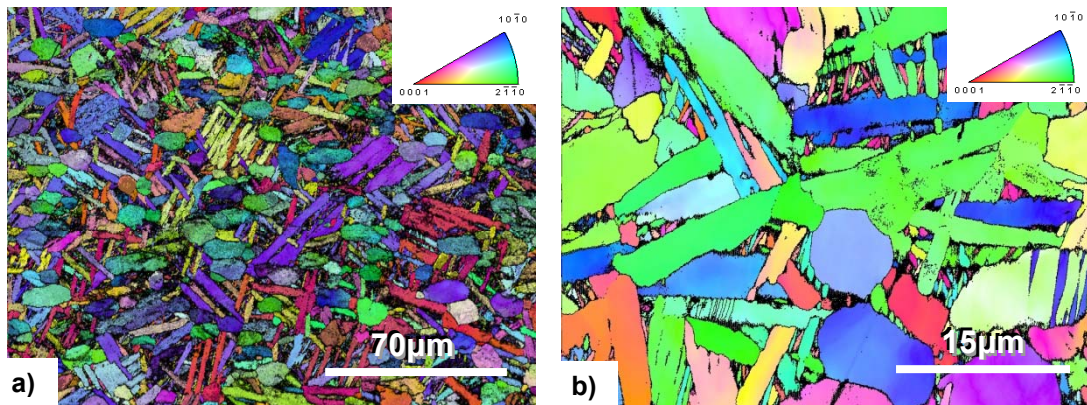


Fig.4.23. EBSD orientation map of Ti-6Al-4V double cone samples deformed at 970°C, 5s<sup>-1</sup>, 1.1 strain and heat treated at 930°C, 30min, Air cooled. a) Low b) Big magnification.

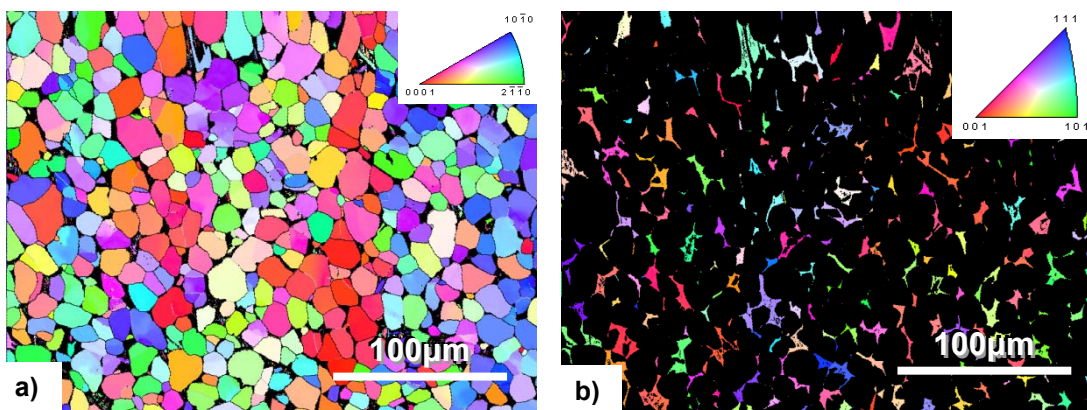


Fig.4.24. EBSD orientation map of Ti-6Al-4V double cone samples deformed at 930°C, 5s<sup>-1</sup>, 1.1 strain and heat treated up to 925°C in HT2. a) α phase b) β phase.

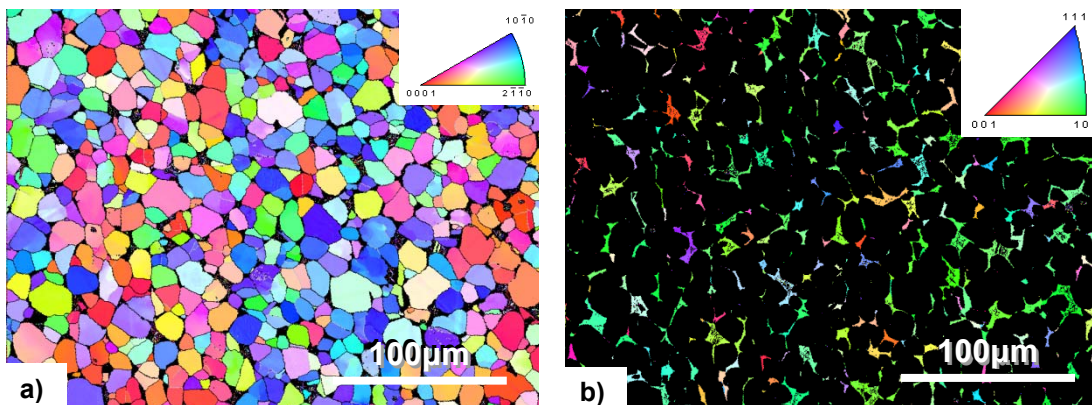


Fig.4.25. EBSD orientation map of Ti-6Al-4V double cone samples deformed at 930°C, 0.1s<sup>-1</sup>, 1.1 strain and heat treated up to 925°C in HT2. a) α phase b) β phase.

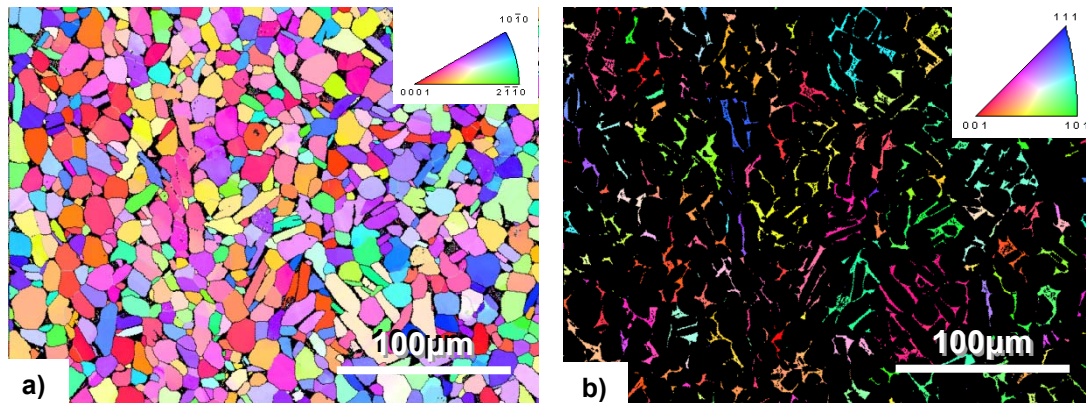


Fig.4.26. EBSD orientation map of deformed Ti-6Al-4V double cone samples at 970°C, 5s<sup>-1</sup>, 1.1 strain and heat treated up to 925°C in HT2. a)  $\alpha$  phase b)  $\beta$  phase grains shown by the same colour.

## 4.2. Quantification

The results shown in this section are obtained from the micrographs of HT1 explained in section 3.2. Fig.4.27 and Fig.4.28 show the size distributions of  $\alpha$  primary grains after deformation at 930°C to different strains at different strain rates. The curves of the samples deformed at 930°C (Fig.4.27) show that there are no differences between both strain rates, therefore curves for strain 0.2 and 0.8 follow the same tendency while the curves for strain 1.1 present a narrower size distribution. The distributions in samples deformed at 970°C (Fig.4.28) show a higher portion of small grains than the ones in samples deformed at 930°C (Fig.4.27). There are no considerable differences between different strain conditions in Fig.4.28. Fig.4.29 presents the total amount of primary  $\alpha$  content for the deformed samples. Samples deformed at 930°C have a higher  $\alpha$  content than the ones deformed at 970°C and there is no considerable effect of the strain rate and strain in any case.

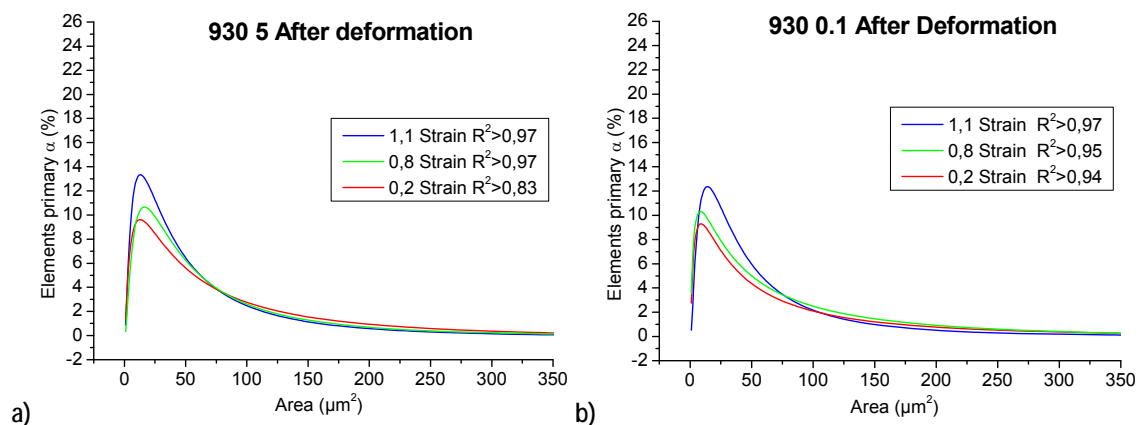


Fig.4.27.  $\alpha$  primary grain size distribution at different strains in the samples a) deformed at 930°C, 5s<sup>-1</sup> b) deformed at 930°C, 0.1s<sup>-1</sup>.

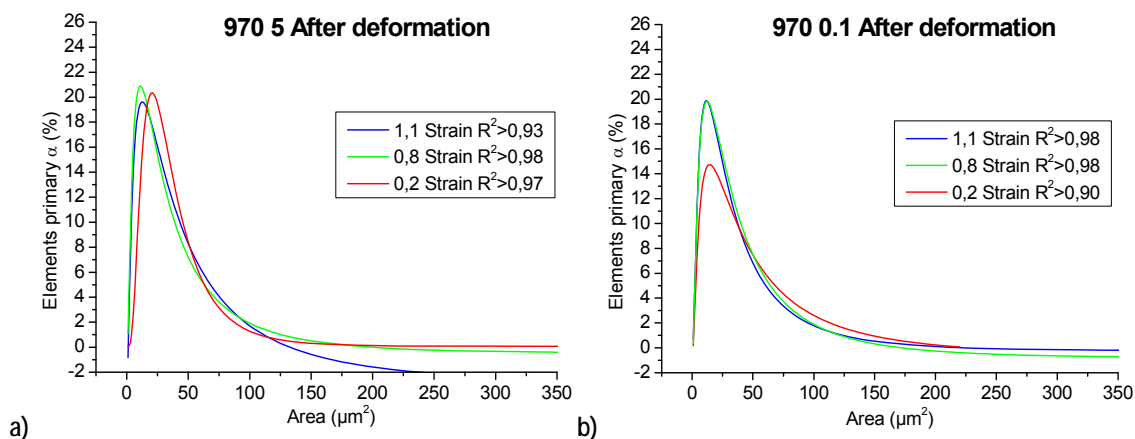


Fig.4.28.  $\alpha$  primary grain size distribution at different strains in the samples a) deformed at 970°C, 5s<sup>-1</sup> b) deformed at 970°C, 0.1s<sup>-1</sup>.

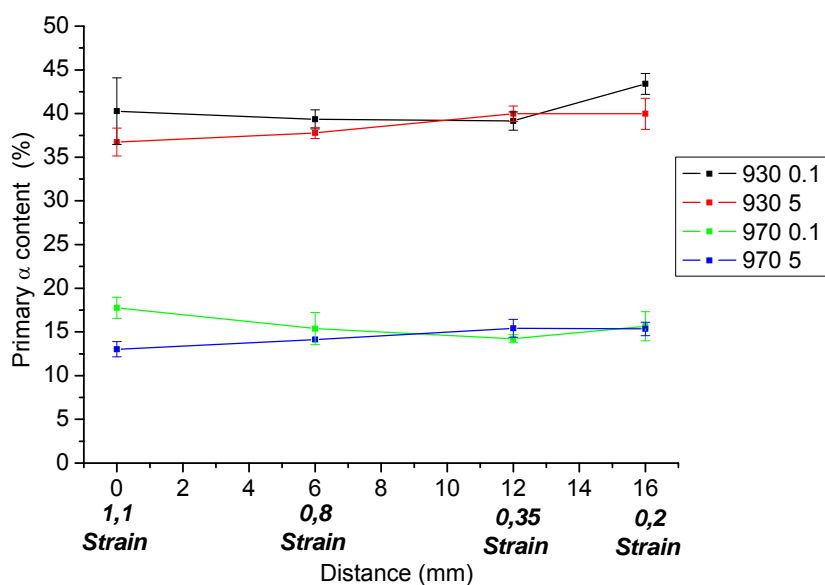


Fig.4.29.  $\alpha$  primary content for different strains in samples deformed at 930 and 970°C at 0.1s<sup>-1</sup> and 5s<sup>-1</sup> strain rate.

The same information is seen in the Fig.4.30, Fig.4.31 and Fig.4.32 for the samples heat treated in HT1. The size distribution of the samples deformed at 930°C remains the same independently from the applied heat treatment. The graphs of Fig.4.30b and Fig.4.31 have identical  $\alpha$  size distributions showing no influence of the strain rates, heat treatment temperature and cooling. Only curves of the sample in Fig.4.30a have a narrower distribution compared with the ones commented before, but there is influence of the strain as well.

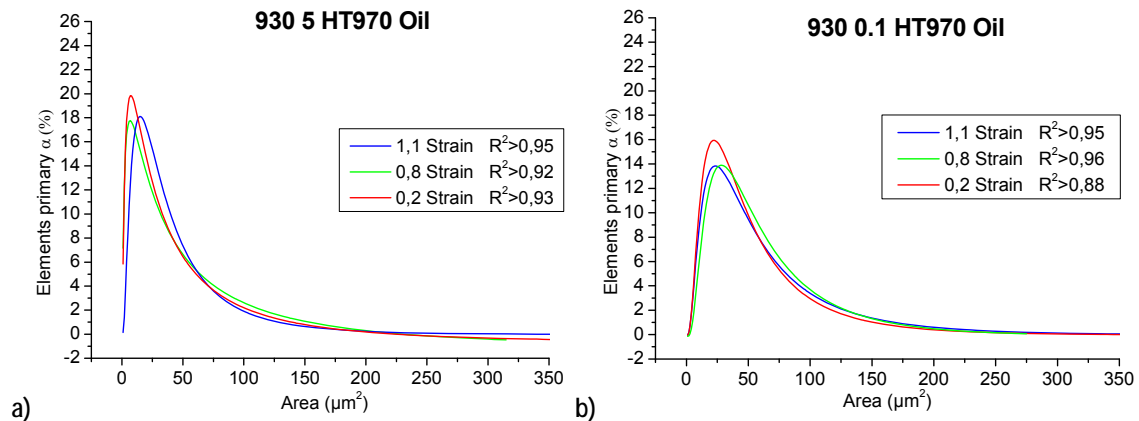


Fig.4.30.  $\alpha$  primary grains size distribution for different strains in the samples a) deformed at 930°C, 5s<sup>-1</sup> and heat treated at 970°C, 30min, oil cooled b) deformed at 930°C, 0.1s<sup>-1</sup> and heat treated at 970°C, 30min, oil cooled.

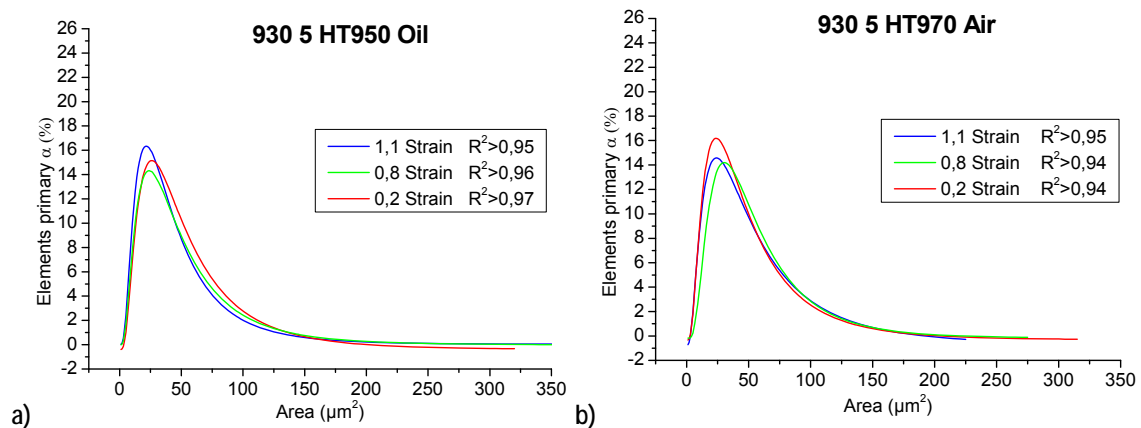


Fig.4.31.  $\alpha$  primary grains size distribution for different strain ranges in the samples a) deformed at 930°C, 5s<sup>-1</sup> and heat treated at 950°C, 30min, oil cooled b) deformed at 930°C, 5s<sup>-1</sup> and heat treated at 970°C, 30min, Air cooled.

Two more samples deformed at 970°C with different strain rates were also quantified (Fig.4.32). In general, there are no considerable differences between the alpha grain size distribution in the samples after HT1.

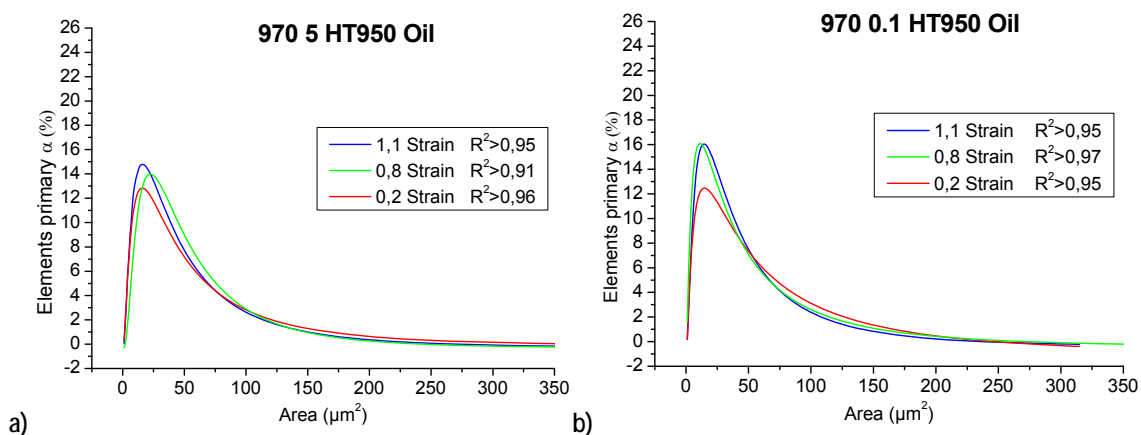


Fig.4.32.  $\alpha$  primary grain size distribution for different strain rates in the samples deformed at 970°C and heat treated at 950°C, 30min, oil cooled a) 5s<sup>-1</sup> b) 0.1s<sup>-1</sup>.

The total amount of primary  $\alpha$  content is shown in Fig.4.33 after deformation at different strain rates and temperatures and after different heat treatments. The samples with less quantity of  $\alpha$  primary are in general the ones deformed at 930°C and heat treated at 970°C in oil cooling condition. Thus, can be said that in the heat treated samples there is no big effect of the strain on the  $\alpha$  primary content.

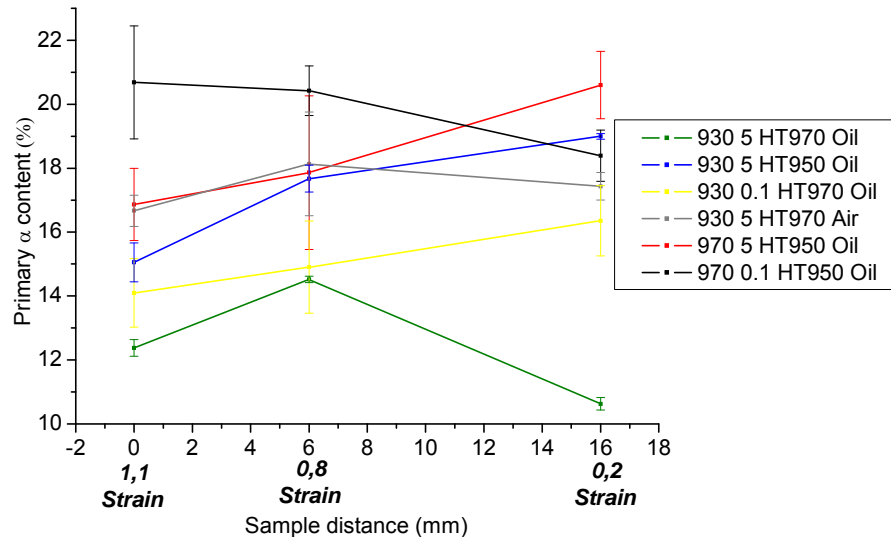


Fig.4.33.  $\alpha$  primary content in samples deformed to different strains and heat treated in different conditions.

Fig.4.34 shows the mean alpha grain size value for the same samples commented in Fig.4.33. This value is the average of the  $\alpha$  primary areas measured in the micrographs. The values shown are just for guidance. The standard deviation is related to the size distribution, and is not shown here. The sample with smaller  $\alpha$  grains is the one with less  $\alpha$  content as well. However, there is no tendency to make a relationship between the mean value and the heat treatments with the strain. Half of the samples show big differences of the mean values in the different strain rates either decreasing or increasing it.

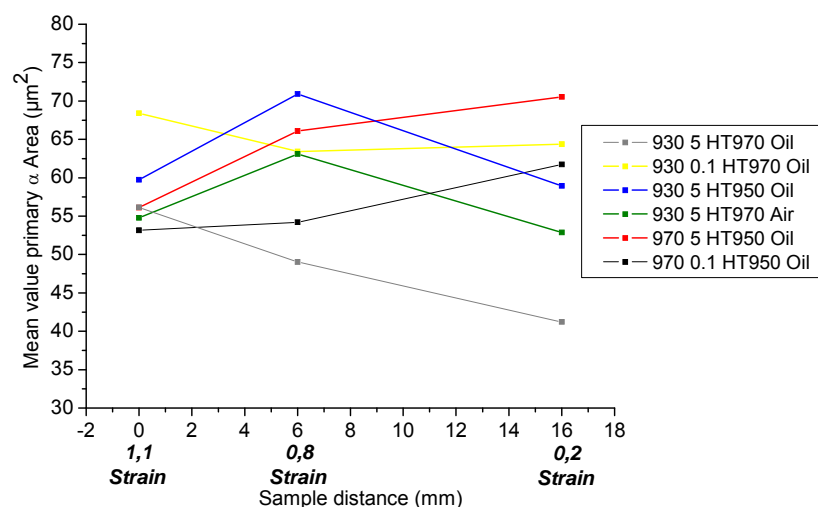


Fig.4.34.  $\alpha$  primary mean grain size for different strains in samples deformed and heat treated in different conditions.

Secondary  $\alpha$  plates were also quantified in two samples deformed at 970°C (Fig.4.35). The measurements of the content of  $\alpha$  plates (sticks) are shown in Fig.4.36 for the two analysed samples for different strains. The sample deformed at a higher strain rate presents a higher content of plates for at large strains, whereas at 0.2 of strain, the value reaches that of the other sample. On the contrary, the sample deformed at slow strain rate has a constant content of  $\alpha$  secondary plates for all the strain.

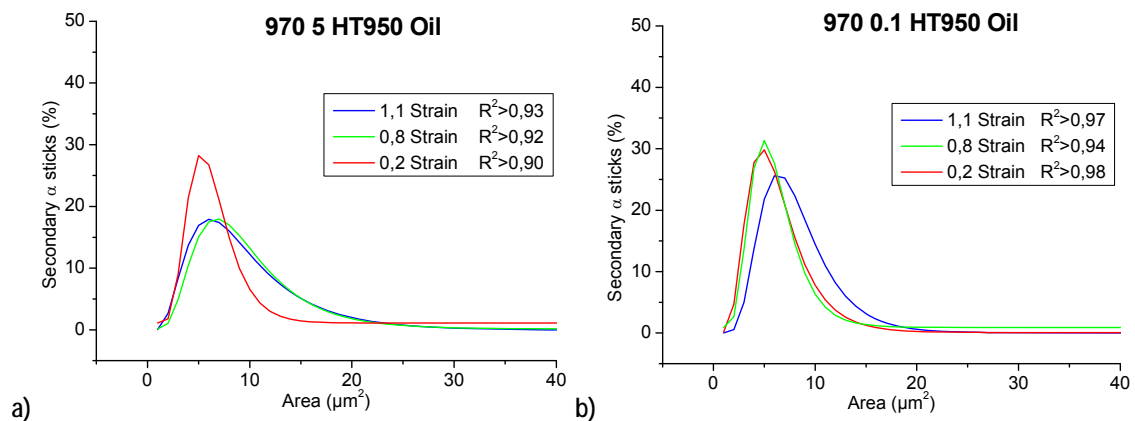


Fig.4.35.  $\alpha$  secondary plates size distribution for different strains in the samples deformed at 970°C and heat treated at 950°C, 30min, oil cooled a) 5  $\text{s}^{-1}$  b) 0.1  $\text{s}^{-1}$ .

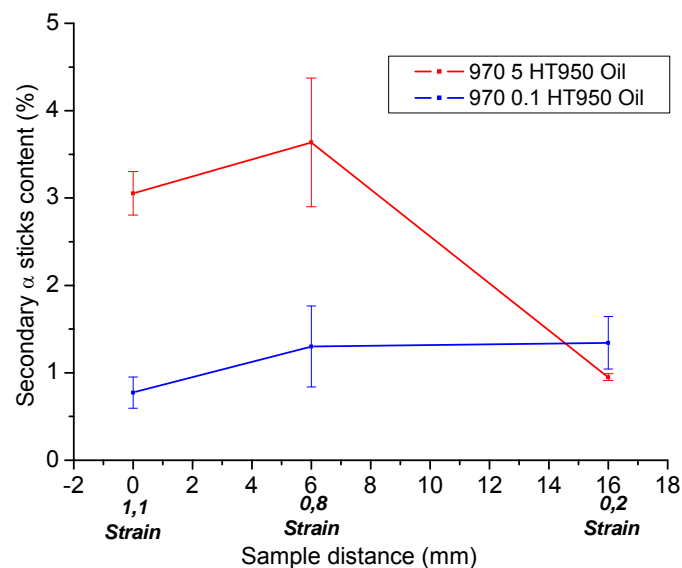


Fig.4.36. Content of  $\alpha$  secondary sticks for different strains in two samples deformed at 970°C with different strain rates.

### 4.3. DSC

Fig.4.37, Fig.4.38, Fig.4.39 and Fig.4.40 show the DSC tests with the  $\text{Al}_2\text{O}_3$  sample as reference. All of the curves present a different distribution of peaks until 800-900°C, and then all of them show the peak of distribution of primary  $\alpha$  around 1000°C. All of the curves except the ones shown in Fig.4.39b and Fig.4.40a have three endothermic peaks corresponding to the dissolution of secondary  $\alpha$  phases, like laths, plates, needles, etc. In both Fig.4.39b and Fig.4.40a a fourth peak appears. In Fig.4.39b that peak is placed at a considerably low temperature where no phase could be dissolved, so it is attributed to an artefact. On the other hand, the fourth peak in Fig.4.40a could be attributed to dissolution of a secondary phase. Should be said that the intensity and height of the peaks in each curve is really different.

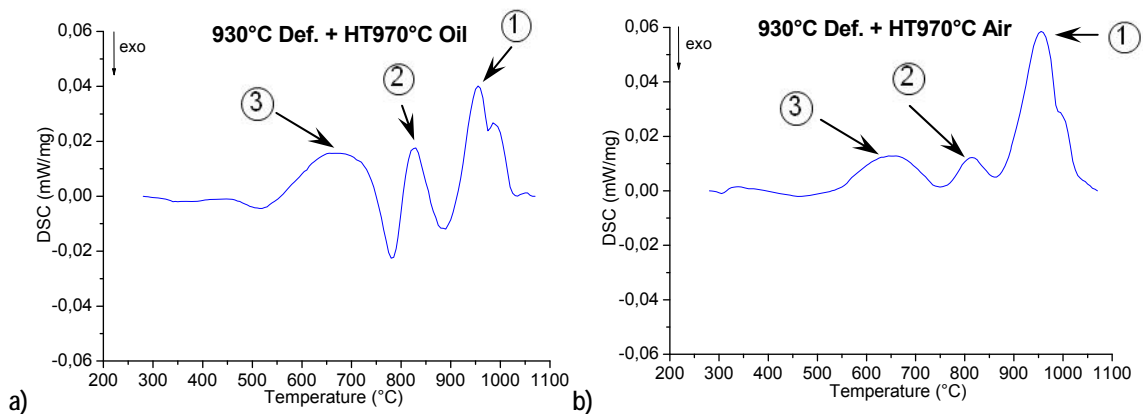


Fig.4.37. DSC heat flow curves for 20 K/min heating stage using  $\text{Al}_2\text{O}_3$  as a reference sample for Ti64 deformed at 930°C, 1s<sup>-1</sup> and heat treated at 970°C, 30min, a) oil cooled b) Air cooled.

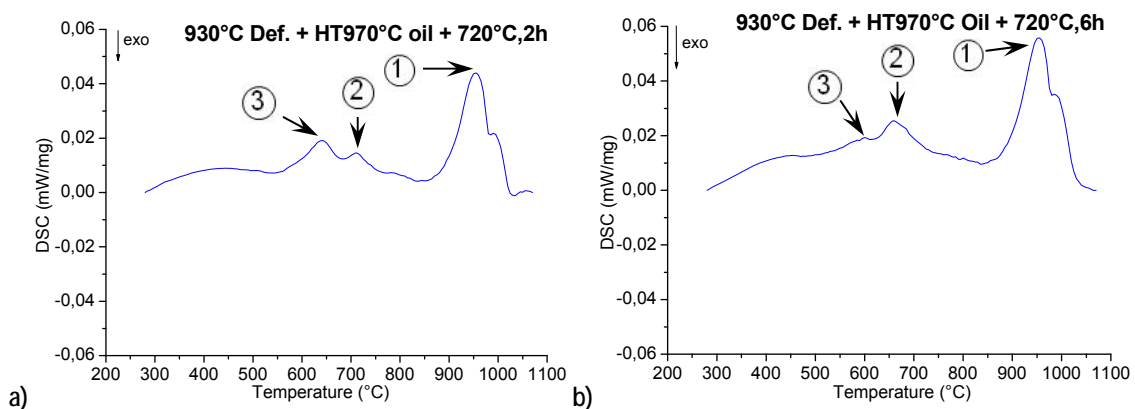


Fig.4.38. DSC heat flow curves for 20 K/min heating stage using  $\text{Al}_2\text{O}_3$  as a reference sample for Ti64 deformed at 930°C and heat treated at 970°C, 30min, oil cooled, plus ageing at 720°C, 2h a) strain rate 1s<sup>-1</sup> and aged for 2h b) 5s<sup>-1</sup> and ageing for 6h.

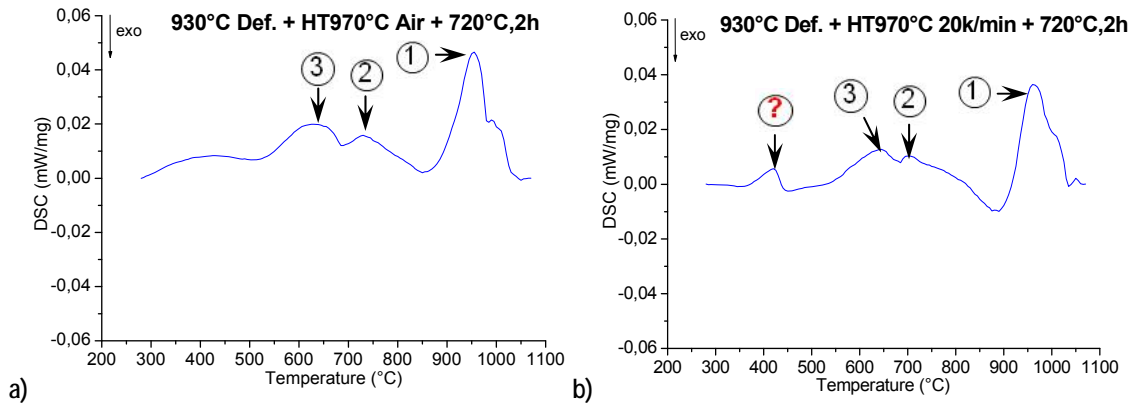


Fig.4.39. DSC heat flow curves in the continuous heating stage using  $\text{Al}_2\text{O}_3$  as a reference sample for Ti64 deformed at  $930^\circ\text{C}$ ,  $5\text{s}^{-1}$  and heat treated at  $720^\circ\text{C}$ , 30min plus ageing at  $720^\circ\text{C}$ , 2h a) air cooled b) 20K/min.

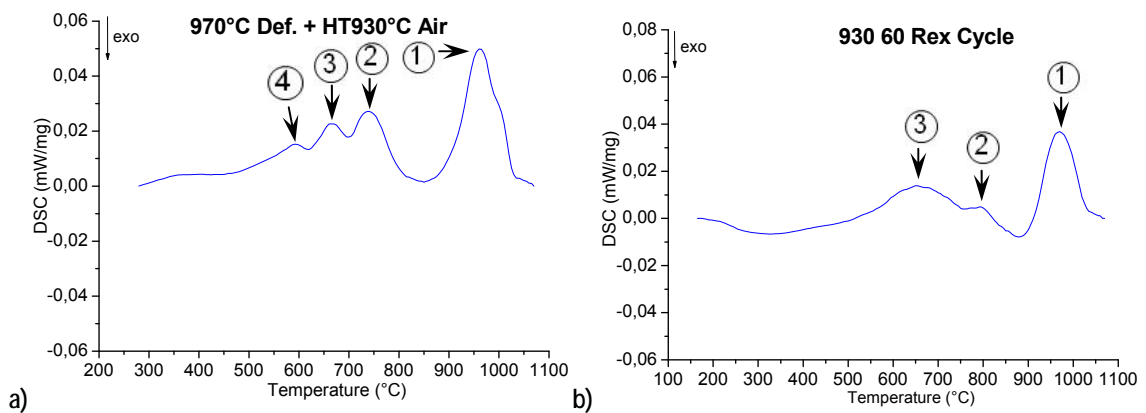


Fig.4.40. DSC heat flow curves in the continuous heating stage using  $\text{Al}_2\text{O}_3$  as a reference sample for Ti64 a) deformed at  $970^\circ\text{C}$ ,  $5\text{s}^{-1}$  and heat treated at  $930^\circ\text{C}$ , 30min, Air cooled b) deformed at  $930^\circ\text{C}$ ,  $5\text{s}^{-1}$  and heat treated until  $925^\circ\text{C}$  in the recrystallization cycle.

The Fig.4.41 and 4.42 plot the DSC graphs obtained with  $\text{Al}_2\text{O}_3$  reference samples for the peaks 1, 2 and 3. Fig.4.41 shows the temperature range of every peak of each sample. The temperatures of peak 1 are quite similar for all the samples. On the contrary, the temperatures of peak 2 have different values for all the samples. The higher temperatures are in the sample without ageing (1, 2) heat treated at higher temperature than the deformation temperature, and the lowest is in the sample aged during six hours. Temperature peak 3 values are similar for all the samples except in the six hours aged one, which has lower value. On the other side, the values of the energy of every peak are shown in Fig.4.51. In this case for peak 1, the highest energy value is for the one aged during six hours. Subsequently the same sample with the heat treatment at  $930^\circ\text{C}$  has the highest values for peak 2, and aged sample number 6 has the highest value for peak 3. It is important to say, that in all the samples the value in peak 1 is higher than for peak 2 or peak 3, but in some samples the value of peak 3 is higher than the value for peak 2.

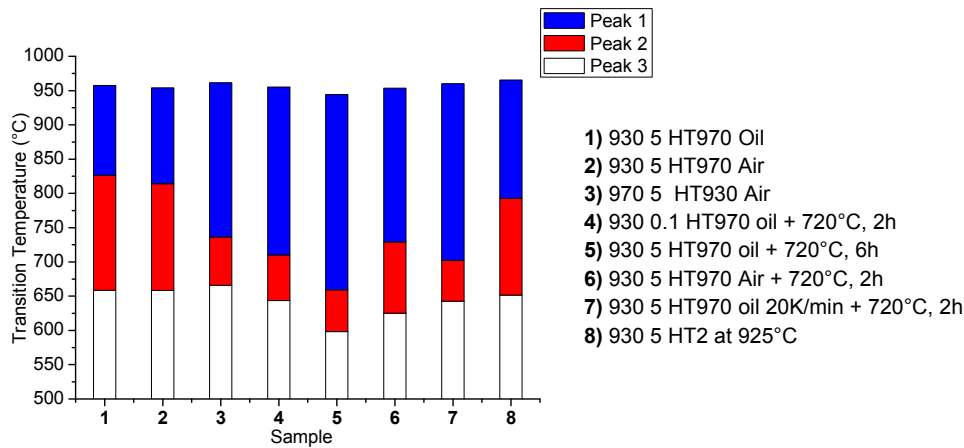


Fig.4.41. Values of temperature in the first three peaks for the studied samples.

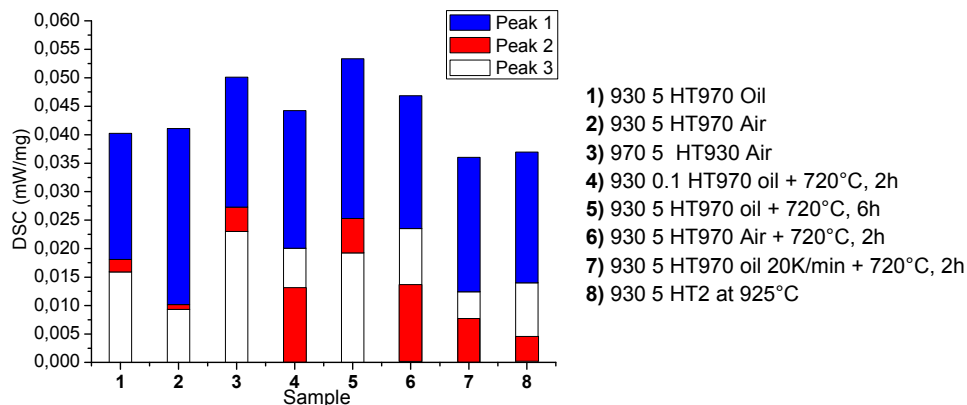


Fig.4.42. Values of energy in the firsts three peak of the studied samples.

#### 4.4. Dilatometry

HT2 tests were carried out in the dilatometer and the obtained measurements of these samples are shown in Fig.4.43. The results present the graph of length change vs. time for the studied specimens in these heat treatments during the first stage of the heat treatments where there is no substantial oxidation that can affect them. Every sample shows that the length increase during the heating until 925°C, denoting a sharp peak and then decrease until around 1000s during the part of the isothermal stage at 925°C and increases again. The peak can be related to the early stage of stabilization of the phases.

Fig.4.44 compares the isothermal percentage difference between the peak value and the minimum value for each deformed sample condition and as received condition. The higher length changes were obtained for the as-received sample and the deformed sample at 930°C, 5s<sup>-1</sup> and 0.2 of strain. The lowest for the sample deformed at 970°C, 0.1s<sup>-1</sup> to 1.1 strain. Comparing the samples deformed at 930°C and at 970°C for the same parameters of deformation, the

samples deformed at the lower temperature show higher length differences. An influence of the strain was also observed, with higher values at lower grades of deformation.

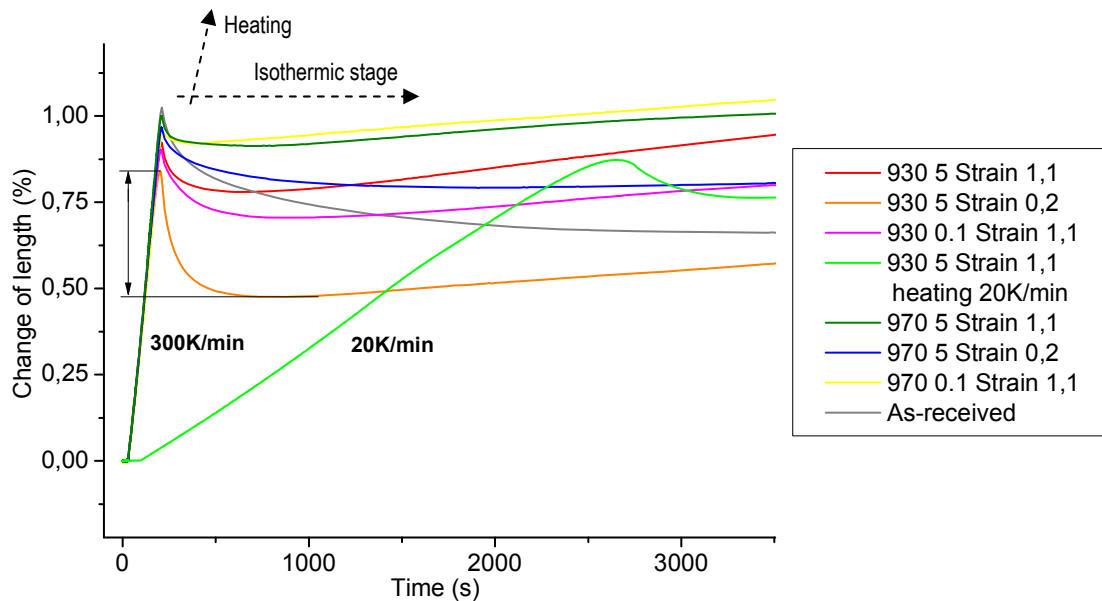


Fig.4.43. Change of length (%) of the deformed samples, indicating the gap between the peak and lower value of change of length during the isothermal stage for one of the measurements.

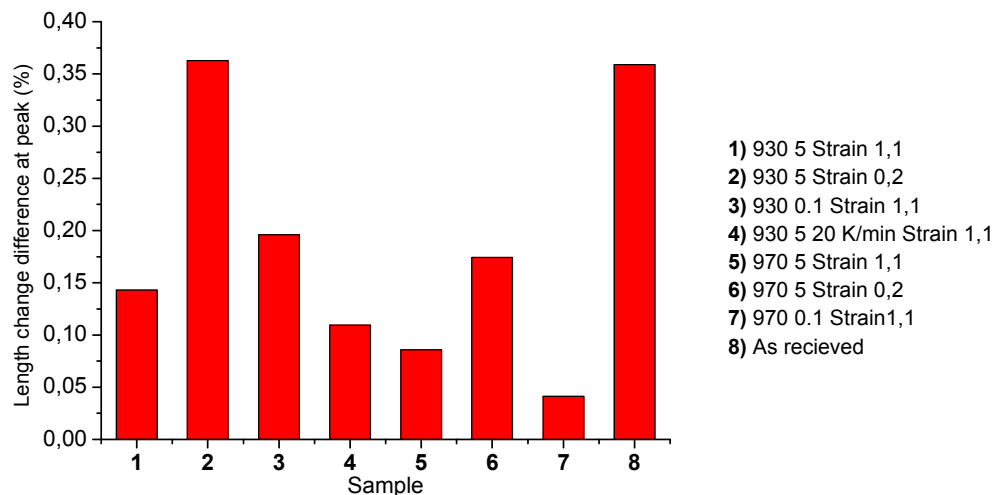


Fig.4.44. Isothermal change of length difference (%) of the deformed samples at peak.

## 4.5. Hardness

Fig.4.45 shows the values of Vickers macrohardness tests in the compressed samples for strain 1.1 and strain 0.2. In general, all the samples show a higher value of hardness in the strain 1.1 condition than for strain 0.2, except for one condition (sample 7). In general, there is a small difference of hardness between strain 1.1 and strain 0.2, but in sample3 there is a noticeable difference that could be related to the microstructure. The samples that have the highest value of hardness (samples 1 and 3) are the ones just heat treated in  $\alpha+\beta$ . The one cooled down at

20K/min from the heat treated in  $\alpha+\beta$  plus ageing (sample 10) presents the lowest value. The sample from HT2 (sample 11) show a low value of hardness, while the aged samples are in a similar range of values, with the highest hardness for the sample aged during 6 hours.

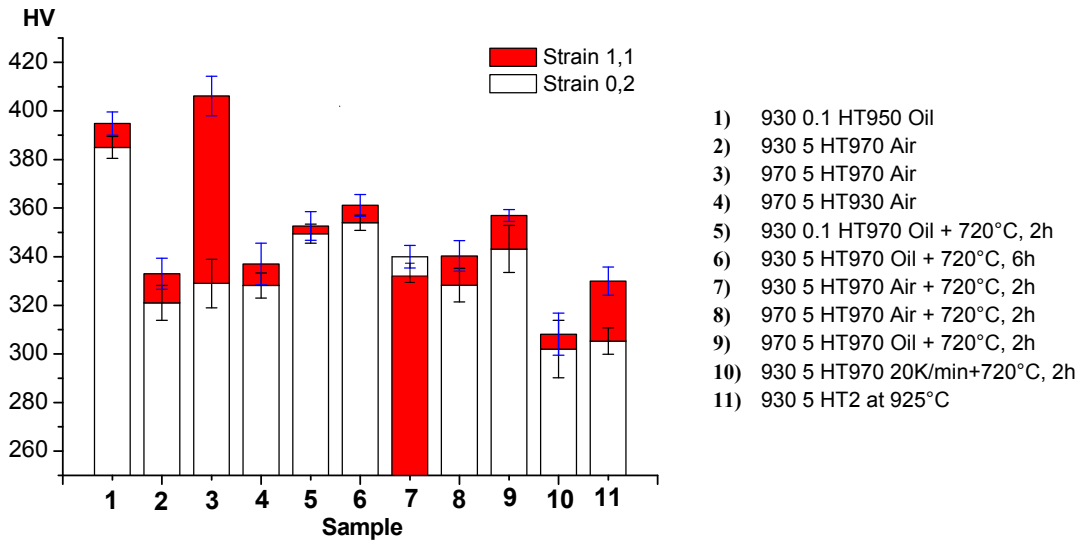


Fig.4.45. Values of Vickers macrohardness for heat treated samples at strains of 1.1 and 0.2.

Microhardness measurements (Fig.4.46) in the different phases show also a higher value in strain 1.1, and the same behaviour as the macro measurements for the same conditions but with higher values. In addition, in Fig.4.46 can be seen that in each sample the hardness value of the primary  $\alpha$  is slightly higher than the martensite phase.

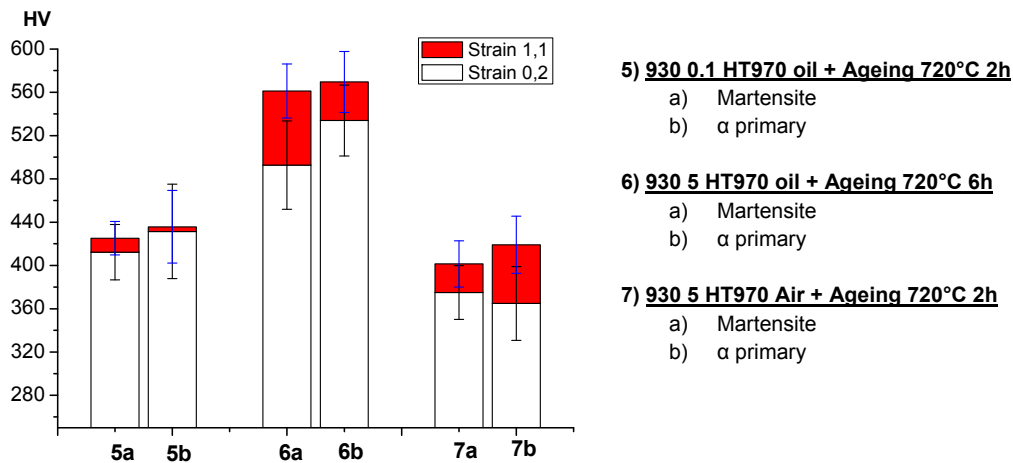


Fig.4.46. Values of Vickers microhardness for heat treated samples at strains 1.1 and 0.2 numbered according to Fig.4.45.

## 5. Interpretation and discussion

---

### 5.1. Phase transformations at high temperature treatments

The HT1 applied to samples deformed samples at 930°C, revealed dissolution of primary  $\alpha$  when the temperature of the heat treatment is higher than the deformation temperature. The diagram of  $\alpha$  primary content (Fig.4.33) in section 4.2 shows in general lower values for the heat treated and oil cooled samples at 970°C compared to the ones treated at 950°C for the same deformation condition. In addition, figures 4.30, 4.31 and 4.32 showed that there is no difference in the size distribution of  $\alpha$  primary for different strain values; therefore the effect of the heat treatment is stronger than the preceding deformation. Comparing the size distributions after the heat treatments (figures 4.27 and 4.28) with the ones obtained after deformation (figures 4.30, 4.31 and 4.32), the first ones show smaller grains than the deformed ones. In addition  $\alpha$  primary content in deformed samples (Fig.4.29) show higher values than the heat treated ones (Fig.4.33). These effects are the result of  $\alpha$  dissolution and separation of the interconnected  $\alpha$  grains during the heat treatment. Particularly, the sample deformed at 5s<sup>-1</sup> and heat treated at 970°C followed by oil cooling, shows a narrow alpha size distribution

The primary  $\alpha$  grain size distributions after HT1 at lower temperature than the deformation (Fig.4.32), show a slight change comparing to the other distributions of higher heat treatment temperature than deformation temperature (figures 4.31 and 4.32). After deformation at 970°C and water quenching,  $\alpha$  primary and martensite is formed. During the heat treatment at 930°C this martensite transforms into secondary  $\alpha$  plates by diffusion transformation with nucleation and growing of new alpha plates (Fig.4.10). An influence of the strain rate and strain on the size and content of the secondary  $\alpha$  sticks during deformation was detected (figures 4.35 and 4.36). At low strain rate (0.1s<sup>-1</sup>) the size as well as the content of alpha sticks do not change considerably, while at high strain rates an increment in content and size of these sticks is observed for strains higher than 0.2. Thus could be related to the nucleation points generated during the deformation by crystallographic defects activated by the mechanism of restoration. Work of Weixin on Ti-6Al-4V [3] has shown that the higher the temperature during deformation, the more the dislocation density decreases in the material, and the higher the strain rate and the strain, the more crystallographic defects increase. In addition, when there is a high dislocation density, secondary  $\alpha$  plates nucleate in the defects, otherwise they make nucleate in  $\beta$  grain boundaries. Following this criterion, in the sample with higher strain rate and strain

condition the quantity and content of  $\alpha$  secondary plates should be higher. It is just partially true with the obtained results.

## 5.2. Ageing treatment

The microstructure of the aged samples was found to depend strongly on the previous cooling rate. In oil cooled samples, the  $\alpha'$  martensite transforms into  $\alpha$  needles and  $\beta$  phase controlled by the diffusion of vanadium. The  $\alpha'$  martensite is supersaturated in  $\beta$  stabilizers (vanadium in this case) and during the annealing in  $\alpha+\beta$  field, it decomposes into  $\alpha+\beta$  by precipitating incoherent  $\beta$  particles at dislocations or  $\beta$  layers at plate boundaries. In this case, no effect of the strain on the microstructure of alpha needles was observed. There is an effect on the  $\alpha$  precipitates morphology by the ageing time. The sample aged during longer time (6 hours) has shown bigger  $\alpha$  laths (Fig.15) compared to the 2 hours ageing (figures 4.13 and 4.14). Ageing tests carried out after air cooling (Fig.4.16) produced a growth in  $\alpha$  laths, and when the cooling was slower (20K/min), secondary alpha grains grew, showing afterwards apparently no effect of the ageing (Fig.4.17). The resulting microstructures of ageing tests depending on the ones obtained in the previous cooling rates are shown in Fig.5.1. As it was pointed out from macrohardness results (Fig.4.45), Fig.5.1 also shows that aged structures form  $\alpha'$  martensite have a higher values of hardness than the ones from air and slower cooling rates.

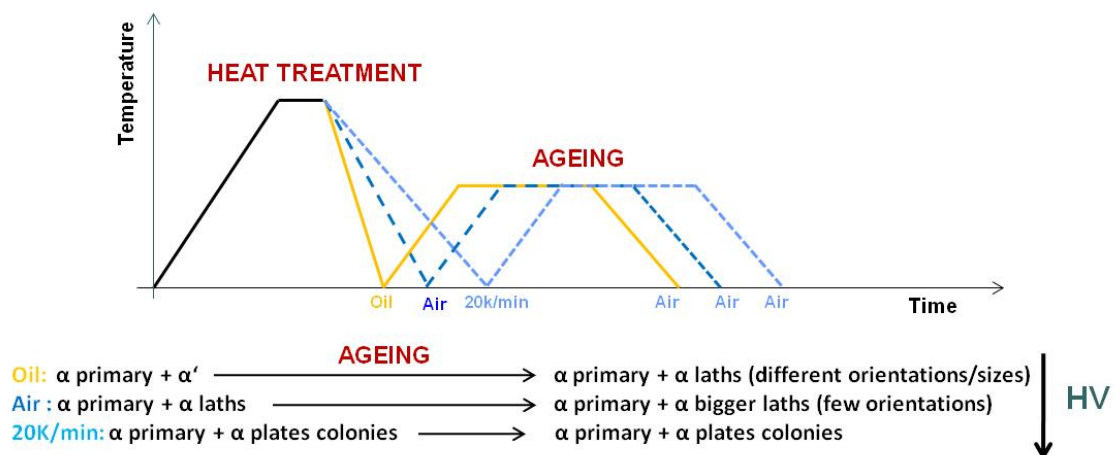


Fig.5.1. Scheme of microstructural effect of the ageing depending on the cooling rate from HT1 with the hardness tendency.

The DSC test carried out with the oil cooled sample from HT1 checks the commented decomposition behaviour of the  $\alpha'$  martensite (Fig.5.2). The hcp  $\alpha'$  martensite is supersaturated in  $\beta$  stabilizers and during the annealing transforms into  $\beta$  and  $\alpha$  lean in vanadium into  $\alpha$  secondary. This reaction can be seen in the indicated exothermic peak, and the anterior peak could be attributed to dissolution of small resting quantities of  $\alpha$  secondary. After the  $\alpha' \rightarrow \alpha_{\text{sec.}} + \beta$  precipitation the next endothermic peak corresponds to its dissolution.

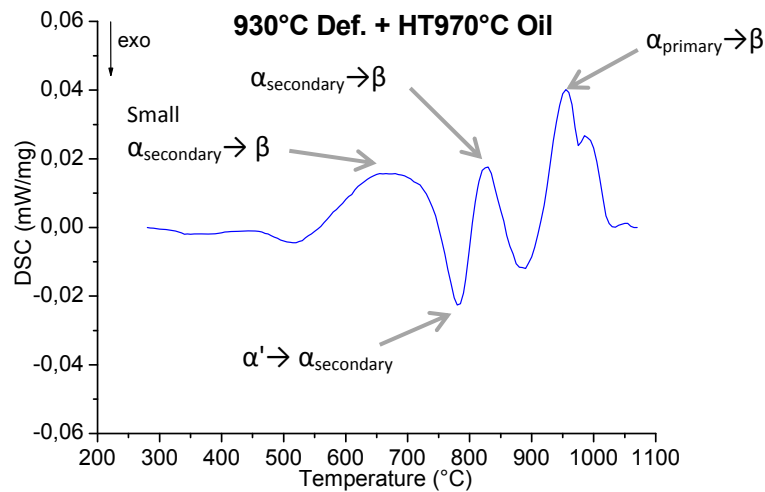


Fig.5.2. Phase transformations of the sample deformed at 930°C and treated up to 970°C in HT1 followed by oil cooling.

The same commented flow curve in Fig.5.2, is compared with another curve from the same HT1 but air cooling condition (Fig.5.3). In contrast, the air cooled sample has no martensite, therefore has no exothermic peak and just endothermic reactions of secondary  $\alpha$  dissolutions.

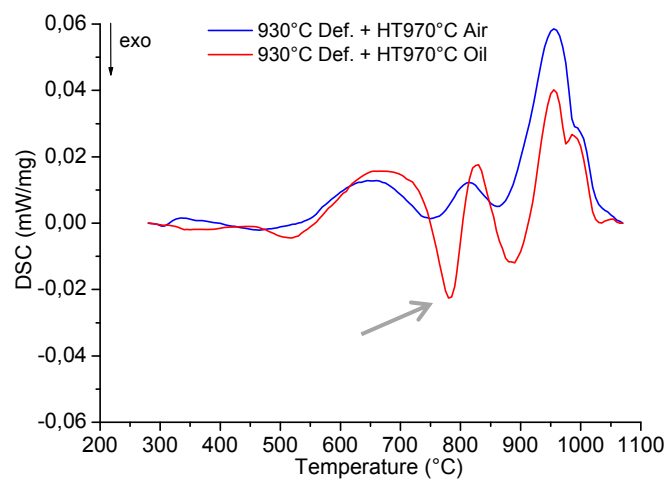


Fig.5.3. Comparison of DSC heat flow curves of two samples from the same HT1 cooled down in air and oil conditions.

In aged samples the  $\alpha' \rightarrow \alpha + \beta$  decomposition was developed in an isothermal process at 720°C thus these samples show in Fig.5.4 that endothermic peaks correspond to the dissolution of  $\alpha$  secondary placed around this temperature. On the contrary, the oil cooled sample without ageing shows the endothermic peak of  $\alpha$  secondary dissolution at higher temperatures because the formation of this phase depends on the slow continuous heating rate.

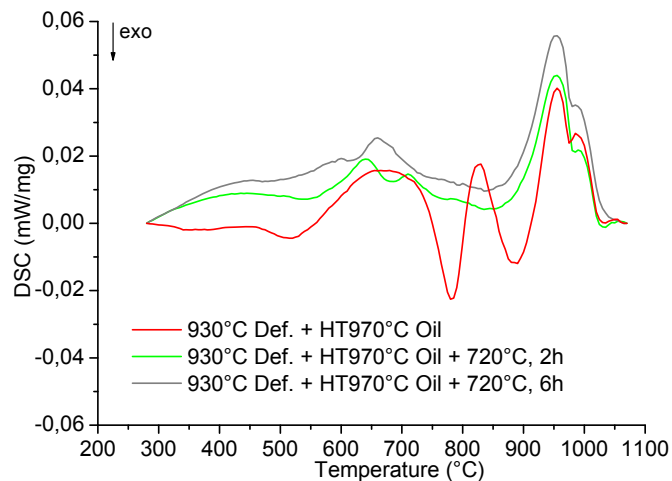


Fig.5.4. Comparison of DSC heat flow curves of different samples with the same HT1 in without ageing, ageing during 2 hours and 6 hours.

### 5.3. Recrystallization treatment

The sample deformed at 930°C and heat treated at 925°C shows the best recrystallized, globular, equiaxed and homogeneous microstructure, independently of the strain and strain rate. In this case, the appearance of very fine secondary  $\alpha$  plates among the alpha grains (Fig.4.18) could be related to the small temperatures gradients (5°C) between deformation temperature and isothermal heat treatment temperature. With same conditions of deformation but with isothermal heat treatment at 970°C, the microstructure shows also globular equiaxed alpha grains but coarser. When the temperature of deformation was 970°C, the heat treatments with isothermal stage at the same temperature or lower have formed a microstructure with the presence of secondary  $\alpha$  plates. Works of Semiatin's group related to kinetics of globularization over 900-955°C presented that globularization mechanisms during annealing are governed firstly by recession plus division of lamellae and coarsening of  $\alpha$  segments by termination migration afterwards [29]. Basically the recrystallization cycle can be related to these mechanisms, where the first isothermal stage could be governed by division of the lamellae and then growing of  $\alpha$  elements by migration of particles. During the slow cooling (~1K/min) the diffusivity of aluminium and vanadium play an important role up to the end of the first cooling stage (760°C) where there is almost no diffusion of both elements [30]. For this reason, the first two stages of those heat treatments determine the microstructure of the material.

Table 5.1 summarizes the obtained microstructures from HT2 depending on the deformation and heat treatment temperature variables. Following  $\alpha$  plates appear just after deformation at 970°C independently of the following heat treatment temperature. EBSD orientations maps of the  $\beta$  phase in these samples (figures 4.24b, 4.25b and 4.26b) showed smaller  $\beta$  subgrains for the deformation temperature of 930°C. The lower the deformation temperature, the smaller are

the  $\beta$  subgrains and consequently there are less sites to grow the  $\alpha$  plates between the equiaxed  $\alpha$  particles.

		Deformation temperature	
		930°C	970°C
Heat treatment temperature	930°C	Fully recrystallized microstructure with fine equiaxed $\alpha$ particles	Equiaxed microstructure with fine $\alpha$ plates
	970°C	Fully recrystallized microstructure with coarse equiaxed $\alpha$ particles	Equiaxed microstructure with coarse $\alpha$ plates

Table 5.1. Resulting microstructure in HT2 depending on the deformation and heat treatment temperatures.

#### 5.4. Thermal analysis

Depending on the morphologies of  $\alpha$  secondary phases obtained in the samples from different heat treatments carried out in this work, DSC measurements showed a different distribution of peaks. In most of the cases the microstructure can be correlated with the obtained peaks. In all specimens at least three endothermic peaks can be compared, although each one has not the same general meaning and should be compared between the samples with the same microstructure or thermal history.

The results from dilatometry measurements can be compared with the ones presented in metallography and quantification that show the effect of the heat treatment to the primary  $\alpha$  morphology. Deformed samples at 930°C show higher length change than the ones deformed at 970°C and the first ones present a higher  $\alpha$  content as well. Both kind of samples show the highest length change in the lowest strain range condition, where the quantification data presented also a higher value of  $\alpha$  content. The content of primary  $\alpha$  in the as-received sample should be the highest of the tested samples, and presents with another sample deformed at 930°C the highest value of length change. Depending on the direction of increase of lattice parameters, the value of length change cannot be totally reliable, but the results show in general a higher length change for the samples with higher  $\alpha$  primary content.

## 6. Conclusions

---

Scanning electron microscopy was used in BSE mode to determine  $\alpha$  and  $\beta$  phases in the investigated Ti-6Al-4V alloy. Micrographs showed dissolution of  $\alpha$  primary in annealing treatments at higher temperature than the deformation one and structures of  $\alpha_{\text{primary}} + \alpha'$  or  $\alpha_{\text{primary}} + \alpha_{\text{secondary laths}}$  for oil or air cooling condition were obtained respectively. On the other side heat treatments at lower temperature than the deformation one showed the presence of  $\alpha_{\text{primary}} + \alpha_{\text{secondary plates}} + \alpha'$  or  $\alpha_{\text{primary}} + \alpha_{\text{secondary plates}} + \alpha_{\text{secondary laths}}$  for the oil or air cooling condition, respectively. Appearance of  $\alpha$  plates was also observed in recrystallization heat treatments with deformed samples at 970°C due to suggested bigger size of  $\beta$  subgrains seen in EBSD orientation maps. A fully recrystallized microstructure with fine equiaxed  $\alpha$  particles was observed for the temperature of 930°C applied in deformation and in heat treatment. Images from aged samples revealed that the resulting microstructure depends on the thermal history and specially on the cooling rate after annealing. Macrohardness tests showed that aged samples from oil cooling condition are harder than the ones from air or lower cooling rates.

The analysis of SEM images in annealed samples made possible to quantify the microstructural features of primary  $\alpha$  but not for the characterization of  $\beta$  substructures. Quantification analysis of  $\alpha$  primary grain size distributions and of primary  $\alpha$  content correlate with dilatometry tests, where samples with higher  $\alpha$  content present higher length change.

The DSC technique was suitable to identify the phases after heat treatments and describe the  $\alpha' \rightarrow \alpha + \beta$  transformation in aged samples during continuous heating. The results also show that dissolution temperature of secondary  $\alpha$  depends on its formation temperature.

## 7. References

---

1. Lütjering G., Williams C. J., *Titanium*, Springer, Berlin, Germany, (2003)
2. Mur Gil F.X, Rodríguez D., Planell J.A., *Influence of tempering temperature and time on the  $\alpha'$ -Ti-6Al-4V martensite*, Journal of Alloys and Compounds 234 (1996), pages 287-289
3. Weixin Y., M.Q. Li, Jiao. L., *Effect of deformation parameters on the precipitation mechanism of secondary  $\alpha$  phase under high temperature isothermal compression of Ti-6Al-4V alloy*, Materials science and engineering A 527 (2010), pages 4210-4217
4. Burgers W. G., Physica 1, 1934.
5. Boyer R., Welsh G., Collings E. W., *Materials properties Handbook: Titanium alloys*, ASM, Materials Park, USA (1994)
6. Zeng Z., Zhang Y., Jonsson S., *Deformation behaviour of commercially pure titanium during simple hot compression*, Materials and design 30 (2009), pages 3105-3111
7. Peters M., Leyens C., *Titan und Titanlegierungen*, Wiley-VCH, Weinheim, Germany (2002)
8. Albrecht. J., Lütjering G., *Microstructure and mechanical Properties of Titanium Alloys*, Titanium 99': Science and Technology, Volume I, pages 366-373
9. Titanium industries, web page: <http://www.titanium.com>
10. Molecular expressions, web page:  
<http://micro.magnet.fsu.edu/primer/pdfs/microscopy.pdf><http://micro.magnet.fsu.edu>
11. Texas University, web page:  
<http://www.bio.tamu.edu/bsif/pdfs/b-40-022-63dmicroscopyaxioplan.pdf>
12. Chraponsky J., Szkliniarz W., *Quantitative metallography of two-phase titanium alloys*, Materials Characterization 46 (2001), pages 149-154
13. Carleton College, web page:  
[http://serc.carleton.edu/research\\_education/geochemsheets/techniques.html](http://serc.carleton.edu/research_education/geochemsheets/techniques.html)
14. Sintef, web page:  
<http://www.sintef.no/Home/Materials-and-Chemistry/Synthesis-and-Properties/Surface-Engineering---Strategic-Institute-Program/Characterisation/FEG-SEM>
15. Photometrics, web page: <http://www.photometrics.net/fesem.html>

16. Collins C. P., Welk B., *Development methods for the quantification of microstructural features in  $\alpha+\beta$  -processed  $\alpha/\beta$  titanium alloys*, Materials Science and Engineering A 508 (2009), pages 174-182
17. Tiley J., Searles T., *Quantification of microstructural features in  $\alpha/\beta$  alloys*, Materials Science and Engineering A373 (2004), pages 191-198
18. Höhne H. W. G., Hemminger F. W., Flammersheim J. H., *Differential Scanning Calorimetry*, Springer, Berlin, Germany, (2003)
19. Sha W., Guo Z., *Phase evolution of Ti-6Al-4V during continuous heating*, Journal of alloys and compounds 290 (1999), pages L3-L7
20. Idhao National Laboratory, web page:  
<http://www.inl.gov/technicalpublications/Documents/3901042.pdf>
21. University of Cambridge, web page: <http://www.msm.cam.ac.uk>
22. Szliniarz W., Smolka G., *Analysis effects of phase transformation in titanium alloys*, Journal of Materials Processing Technology 53 (1995), pages 413-422
23. Pearson W.B., *A Handbook of lattice spacings and structure of metals and alloys*, Pergamon Press (1958), page 876
24. Collings E.W., *Physical Metallurgy of Titanium alloys*, ASM, USA (1989)
25. Sui Y., Li B., LIU A., *Microstructure and Hardness of Ti-6Al-4V alloy staging castings under centrifugal field*, Trans. Nonferrous Met. Soc. China 18 (2008), pages 291-296
26. Qazi J.I., Senkov O.V., *Kinetics of martensite decomposition in Ti-6Al-4V-xH alloys*, Materials Science and Engineering A359 (2003), pages 137-149
27. Poondla N., Srivatsan T.S., *A study of the microstructure and hardness of two titanium alloys: Commercial pure and Ti-6Al-4V*, Journal of Alloys and Compounds, JALCOM-20239 (2009), 6 pages
28. Warchomicka F., Poletti C., Stockinger M., Henke T., *Microstructure evolution during hot deformation of Ti-6Al-4V double cones specimens*, Int. J. Mater Form. 3-1 (2010), pages 215-218.
29. Stefansson N., Semiatin S.L., *Mechanisms of Globularization of Ti-6Al-4V during static heat treatment*, Metallurgical and materials transactions Volume 34A (March 2003), pages 691-698
30. Semiatin S.L., Brown T.M., Goff T.A., *Diffusion coefficients for modeling the heat treatment of Ti-6Al-4V*, Metallurgical and materials transactions Volume 35A (September 2004), pages 3015-3018